

## ABSTRACT

Title of Dissertation:           LOW LOSS INTEGRATED PHOTONIC  
  DEVICES AND THEIR APPLICATIONS IN  
  ASTROPHOTONICS AND QUANTUM  
  INFORMATION

Shengjie Xie, Doctor of Philosophy, 2021

Dissertation Directed by:       Professor Mario Dagenais  
  Department of Electrical and Computer  
  Engineering

The silicon nitride ( $\text{Si}_3\text{N}_4$ ) integration platform for photonics is becoming a low-loss and compact platform for various applications such as astrophotonics and quantum information. In this dissertation, the fabrication techniques for low loss integrated photonics devices is first discussed. Then, we present the design, fabrication, and characterization of an on-chip low-loss (1.39 dB on-chip loss) echelle grating spectrometer that can work in an ultra-broad band (potentially from visible to mid-infrared spectral range) with high resolution and low crosstalk ( $<-30\text{dB}$ ). We demonstrate an on-chip add-drop filter working on arbitrarily spaced five channels based on the complex waveguide Bragg gratings and the multimode interferometer (MMI). A more than 40 dB extinction ratio is achieved in all five channels and the

device is shown to be low loss ( $<1$  dB on chip loss) and broadband ( $>200$  nm 3-dB bandwidth). We also study a Fabry-Pérot Bragg grating cavity enhanced four wave mixing process on a  $\text{Si}_3\text{N}_4/\text{SiO}_2$  platform, from an analytical treatment to an experimental demonstration. A unique grating loss reduction and a dispersion compensation technique is also demonstrated. Multiple loss reduction approaches are demonstrated to further reduce the loss and improve the four-wave mixing efficiency, including depositing thicker  $\text{Si}_3\text{N}_4$  film, using different etch masks, and different etching gases. Using a ring resonator, the waveguide loss has been extracted and reduced from 0.33 dB/cm to 0.18 dB/cm. Moreover, we explore aluminum nitride (AlN) on sapphire as a new platform for integrated photonics devices. A special fabrication process for the AlN-on-sapphire chip is developed and the loss is measured to be 1.95 dB/cm based on a ring resonator approach. Lastly, we demonstrate a high extinction ratio Mach-Zehnder interferometer (MZI) with MMI for exoplanet discovery. The MMI-MZI features an extinction ratio of 58 dB without thermal tuning and 50 dB with thermal tuning. A TM noise reduction technique is also shown to help realize the maximum extinction ratio.

LOW LOSS INTEGRATED PHOTONIC DEVICES AND THEIR  
APPLICATIONS IN ASTROPHOTONICS AND QUANTUM INFORMATION

by

Shengjie Xie

Dissertation submitted to the Faculty of the Graduate School of the  
University of Maryland, College Park, in partial fulfillment  
of the requirements for the degree of  
Doctor of Philosophy  
2021

Advisory Committee:

Professor Mario Dagenais, Chair

Professor Edo Waks

Professor Martin Peckerar

Professor Thomas Murphy

Professor Sylvain Veilleux, Dean's Representative

© Copyright by  
Shengjie Xie  
2021

## Acknowledgment

By finishing the dissertation, the six-year doctoral career at the University of Maryland comes to an end. Looking back to the past six years, it was a challenging but fruitful and enjoyable experience. There are many people I would like to give my sincere thanks to. Without your support, my journey would not be so wonderful.

It is a genuine pleasure to express my deep sense of thanks and gratitude to my advisor, Professor Mario Dagenais, and our long-term collaborator, Professor Sylvain Veilleux. They provide me the opportunity to explore the world of photonics, inspire me to challenge problems that have never been solved before, and encourage me to think outside the box. Without their guidance and support, it is impossible to make all the achievements. I would also like to thank the committee members, Professor Edo Waks, Professor Martin Peckerar, and Professor Thomas Murphy, for their valuable suggestions on my dissertation.

It is my privilege to give my thanks to my colleagues, Dr. Yang Meng, Dr. Yang Zhang, Dr. Yiwen Hu, and Jiahao Zhan, who have worked closely with me and gave me invaluable suggestions based on their experiences and expertise. I also need to thank Dr. Tiecheng Zhu, Dr. Yangyi Yao, Wei-Lun Hsu, Joey Brock, Niloy Acharjee, and Xiheng Ai for the frequent discussions on the research problems.

The fabrication work is made possible by the tremendous support from the Maryland Nanocenter. I would like to thank John Abrahams, Tom Loughran, Mark Lecates, and Jonathan Hummel for supporting and suggest multiple fabrication techniques. I am grateful to Dr. Jiancun Rao and Dr. Sz-Chian Liou for their supports on the SEM operation. I also want to extend my gratitude to Yigal Lilach and Nicole

Charles at George Washington University for their help on fabrication tools during the COVID pandemic.

I am extremely thankful to my parents Hong Xie and Yanlin Long. I would not have gone so far and finished my Ph.D. degree without all their unconditional love, support, and sacrifices during my life.

Lastly, my special thanks go to my wife, Xi Li. I still remember six years ago, when she was my girlfriend, she decided to give up other opportunities to start our new journey at the University of Maryland. We share all the happiness and stress during my Ph.D. career. Her understanding and support were the motivation that kept me pursuing the Ph.D. degree. Thank you for accompanying me and going through the past six years together.

# Table of Contents

Table of Contents .....	iv
List of Figures .....	vi
List of Table .....	xv
Publication List .....	xvi
Chapter 1 : Introduction .....	1
Chapter 2 : Fabrication Techniques for Integrated Photonics Devices.....	3
2.1 Basic Fabrication Process of Integrated Photonics Devices.....	3
2.2 E-Beam Lithography.....	4
2.3 Inductive Coupled Plasma Reactive Ion Etching (ICP-RIE).....	6
2.4 Plasma Enhanced Chemical Vapor Deposition (PECVD) SiO <sub>2</sub> .....	7
Chapter 3 : Echelle Grating Spectrometer for Operation Near 1.55 $\mu\text{m}$ .....	8
3.1 Introduction to Echelle Grating .....	8
3.2 Design and Fabrication .....	11
3.3 Experimental Result.....	15
3.4 Conclusion .....	21
Chapter 4 : Add-Drop Filter with Complex Waveguide Bragg Gratings and Multimode Interferometers Operating on Arbitrarily Spaced Channels.....	22
4.1 Introduction to Add-Drop Filters.....	22
4.2 Device Design and Fabrication.....	25
4.3 Experimental Results .....	33
4.4 Conclusion .....	37

Chapter 5 : On-Chip Fabry-Pérot Bragg Grating Cavity Enhanced Four-Wave Mixing	38
5.1 Introduction to Four-Wave Mixing.....	38
5.2 Theory of FPBG-FWM.....	40
5.3 Bragg Grating Design and Losses Reduction .....	44
5.4 FWM Experimental Results and Analysis.....	48
5.5 Conclusion and Proposed Future Work .....	58
Chapter 6 : On-Chip High Q Ring Resonator.....	60
6.1 Introduction.....	60
6.2 Theory of Ring Resonator.....	61
6.3 Ring Resonator Based on 600nm Si <sub>3</sub> N <sub>4</sub> Film .....	66
6.4 Ring Resonator Based on AlN.....	74
6.5 Discussion and Conclusion.....	80
Chapter 7 : On-Chip High Extinction Ratio Mach-Zehnder Interferometer for Exoplanet Discovery .....	84
7.1 Introduction to Exoplanet Discovery and Nulling Interferometer .....	84
7.2 Recent Advances and Challenges in Nulling interferometer .....	87
7.3 MMI-MZI Design.....	90
7.4 Experimental Results .....	93
7.5 Discussion and Conclusion.....	98
Chapter 8 : Conclusions and Perspectives .....	101
Appendix A: Detailed Fabrication Recipes .....	105
Bibliography .....	107

## List of Figures

Figure 2-1 Fabrication flow of the Si <sub>3</sub> N <sub>4</sub> chip. Both a positive-tone resist process and a negative-tone resist process are shown. ....	4
Figure 2-2 SEM images of the etched waveguide with negative resist mask. (a) Waveguide without oxygen plasma clean after ICP-RIE etching. Crosslink are observed on top of the waveguide. (b) Waveguide with oxygen plasma clean after ICP-RIE etching. The crosslink are successfully removed. ....	6
Figure 3-1 (a) Schematic of echelle grating. (b) Schematic of integrated echelle grating. ....	9
Figure 3-2 Schematic layout of the echelle grating. The light incidents from the input waveguide, propagates through the FPR, is reflected by the grating, and is refocused on the output WGs. 3 Reference WGs are used to extract the propagation loss and coupling loss. ....	12
Figure 3-3 Fabrication process of the proposed echelle grating. ....	14
Figure 3-4 SEM image of the echelle grating. (a) Top view of the echelle grating showing the relative position of WGs and grating teeth. (b) Zoom in image of the grating teeth before deep etching. Grating teeth get precise definition with EBL. (c) The etched facets of the echelle grating covered with silver. 3.1 $\mu\text{m}$ deep etch was achieved by ICP etching with perfect verticality. (d) Zoom in image of the output WGs with smooth edge. ....	15
Figure 3-5 Schematic diagram of the measurement setup. ....	16

Figure 3-6 (a) Measured TE mode transmission pattern of the echelle grating. (b) Superimposed transmission pattern of the fabricated echelle grating's five channels. Very good overlap and a maximum transmission power non-uniformity of 1.2 dB are achieved in our echelle grating. .... 17

Figure 3-7 Schematic layout and SEM image of stitching error. (a-d) Schematic layouts of stitch-free e-beam patterning and e-beam patterning with stitching error. These errors can happen at both left-right boundaries and up-down boundaries (e) SEM image of stitching errors on grating grooves. .... 18

Figure 3-8 Influence of stitching errors on adjacent channel crosstalk. (a) Simulation results of  $100\mu m$  WF transmission pattern with stitching errors. (b) Experimental results of  $100\mu m$  WF transmission pattern with stitching errors. (c) Simulation results of  $200\mu m$  WF transmission pattern with stitching errors. (d) Experimental results of  $200\mu m$  WF transmission pattern with stitching errors [21]. .... 20

Figure 4-1 Schematics of an add-drop filter. .... 23

Figure 4-2 Schematic of ring resonator based add-drop filter. .... 24

Figure 4-3 Schematic layout of the WBG-MMI add-drop filter. Light injects from the input channel waveguide, is evenly split after the first 2x2 MMI. The transmitted light goes towards the through port after the second 2x2 MMI while the reflected light refocuses on the drop port. The WBGs between two MMIs can be of arbitrary types, i.e. simple Bragg grating, phase shift Bragg grating and complex waveguide Bragg grating, for different applications. 26

Figure 4-4 The comparison of the bandwidth performance of the two implemented MMIs, with the power normalized to the input power. The one satisfying the paired interference condition shows a 3-dB bandwidth of more than 200 nm, while the other one only 80 nm.....	28
Figure 4-5 Schematic of the LP/LA algorithm process [22].....	30
Figure 4-6 SEM images of the CWBG-MMI add-drop filter. (a) The MMI and its output waveguides. (b) Identical CWBGs in two arms. The designed CWBG is highly aperiodic. (c) Zoomed-in image of one of the CWBGs showing the precise definition of tiny structures with e-beam lithography. (d) 45° tilted view of the CWBG before final PECVD deposition. A smooth sidewall is achieved with the dry-etching process. ....	32
Figure 4-7 Transmission and reflection signals of the WBG-MMI add-drop filter. ..	34
Figure 4-8 (a) The experimental result of the transmission (blue line) and reflection (red line) spectrum. All five channels show an on-chip loss of < 1 dB, a blue-shift of 0.73 nm of center wavelengths, a spectral precision of better than $\pm 0.2\text{nm}$ , a rejection ratio of > 40 dB and a 3-dB bandwidth of 1.2 nm. (b) Comparison between the initial simulation result, the experimental result, and the fitted simulation result. The experimental result is red-shifted by 0.73 nm to compensate for the mismatch of the positions of center wavelengths due to the index variation.....	36
Figure 5-1 (a) Electric fields in a Fabry-Pérot resonator. (b) Mode profile in a Si <sub>3</sub> N <sub>4</sub> waveguide .....	41

Figure 5-2 Simulation of the relationship between FWM efficiency and grating coupling strength by fixing other parameters. (a) taking the coupling strength to be  $\kappa = 54 \text{ cm}^{-1}$ , maximum efficiency  $\eta = -49.9 \text{ dB}$  in simulation (b) coupling strength  $\kappa = 94 \text{ cm}^{-1}$ , maximum efficiency  $\eta = -45.6 \text{ dB}$  (c) coupling strength  $\kappa = 133 \text{ cm}^{-1}$ , maximum efficiency  $\eta = -43.1 \text{ dB}$  (d) coupling strength  $\kappa = 193 \text{ cm}^{-1}$ , maximum efficiency  $\eta = -39.6 \text{ dB}$ ..... 45

Figure 5-3 Experimental characterization of grating loss of different grating coupling strength. (a) coupling strength  $77 \text{ cm}^{-1}$ , measured grating loss  $1.95 \text{ dB/cm}$ . (b) coupling strength  $110 \text{ cm}^{-1}$ , measured grating loss  $3.1 \text{ dB/cm}$ . (c) coupling strength  $155 \text{ cm}^{-1}$ , measured grating loss  $6.6 \text{ dB/cm}$ . (d) coupling strength  $201 \text{ cm}^{-1}$ , measured grating loss  $12.0 \text{ dB/cm}$ . (e) Transmission pattern of a normal PSBG with a coupling strength of  $125 \text{ cm}^{-1}$  (f) Transmission pattern of PSBG with tapered grating with a coupling strength of  $125 \text{ cm}^{-1}$ . ..... 46

Figure 5-4 Simulation of the  $L' \ 2(IEp)2IEsIEc$  with a grating loss of  $0.36 \text{ dB/cm}$  and a cavity loss of  $0.33 \text{ dB/cm}$ . The  $L' \ 2(IEp)2IEsIEc$  reaches the peak,  $40.21$ , with  $625$  periods of Bragg grating in each mirror and  $390 \text{ um}$  cavity length..... 49

Figure 5-5 (a) Schematic of the experimental setup. The CW pump laser is a thermally tuned butterfly laser diode with a maximum output power of  $13 \text{ dBm}$  and the CW signal laser is an electrically tunable laser with a maximum output power of  $4 \text{ dBm}$ . (b) Schematic of the FPBG, tapered grating is added between regular grating and cavity to facilitate mode conversion between

cavity mode and grating Bloch mode. (c-f) SEM images of the FPBG. (c) Periodic Bragg grating. (d) Straight waveguide between two Bragg grating mirrors. (e) Linearly tapered grating connecting regular Bragg grating and cavity. (f) Tilted view of the linearly tapered Bragg grating. .... 50

Figure 5-6 Transmission pattern of TE Bragg grating without TM noise filter and transmission pattern of TE Bragg grating with TM noise filter. The TE and TM stopbands overlap so that the TM noise inside the TE stopband is suppressed by around 30 dB. .... 52

Figure 5-7 (a) Transmission of the FWM Bragg grating. The 3-dB linewidth of the resonant peak is measured to be 3.3pm, corresponding to a quality factor of 480k. (b) The calculated IE factor inside the stopband. (c) The measured FWM signals. A -37.7 dB conversion efficiency is experimentally observed. (d) Simulation of the FWM conversion efficiency. The theoretical conversion efficiency of the actual device is slightly less than that of the optimum design due to fabrication uncertainty..... 53

Figure 5-8 (a) Comparison of grating induced dispersion and waveguide induced dispersion. The grating dispersion is dominant compared to the waveguide dispersion (b) A zoom-in dispersion comparison shows that the grating dispersion is still dominant around the stopband center. (c) The experimental results of thermal-tuning based dispersion engineering. Resonant peaks drift inside the stopband while leaving the stopband position unchanged. The red line represents the -5.6 MHz FSR detuning position. (d) the FSR detuning changes with the central peak frequency offset showing that thermal tuning

can effectively implement dispersion compensation. Experimental results are in good agreement with the transfer matrix simulation results. The simulation results indicate that zero FSR detuning is achievable. [66] ..... 56

Figure 6-1 Schematics of the ring resonator ..... 62

Figure 6-2 Sample transmission of a ring resonator ..... 64

Figure 6-3 Crack of LPCVD Si<sub>3</sub>N<sub>4</sub> due to internal stress of the film. A Trench can stop the propagation of the crack. [64] ..... 67

Figure 6-4 Setup of LPCVD deposition. (a) Vertical mode (b) Horizontal mode. The inset shows how the individual chips are placed on the carrier wafer. .... 69

Figure 6-5 Mode profile of the ring and bus waveguide. (a-b) Mode profile of the  $2\ \mu\text{m} \times 0.6\ \mu\text{m}$  ring waveguide. The waveguide geometry supports three guided TE mode. (c) Mode profile of the  $0.8\ \mu\text{m} \times 0.6\ \mu\text{m}$  bus waveguide. .... 70

Figure 6-6 Simulated mode profile of the ring-bus coupler. .... 71

Figure 6-7 SEM images of the ring resonator. (a) ring-bus coupling region. (b) tilted view of the ring resonator, a smooth sidewall is achieved with the CHF<sub>3</sub>/O<sub>2</sub> ICP-RIE etch. .... 72

Figure 6-8 Experimental result of the ring resonator with geometry of  $2 \times 0.6\ \mu\text{m}$  and  $200\ \mu\text{m}$  radius. (a) Overall transmission of the ring resonator from  $1450\ \text{nm}$  to  $1640\ \text{nm}$ . (b) Transmission of three ring resonators with different ring-bus gaps at  $1630\text{-}1639\ \text{nm}$ . Three sets of resonances are observed in the ring resonator with  $0.5\ \mu\text{m}$  gap while only two sets of resonances are observed in the ring resonator with  $0.6\ \mu\text{m}$  and  $0.7\ \mu\text{m}$  gap. (c) Zoomed in transmission

of the red circle in (b), resonance split is observed due to the coupling between clockwise (CW) and counter-clockwise (CCW) propagating light, because of imperfect waveguide sidewall. Blue line: experimental results, Black line: Fitting results. .... 73

Figure 6-9 (a) Mode profile of the bus waveguide. (b) Mode profile of the ring waveguide. (c) Bending loss simulation of the TE mode with different bending radius, with the ring waveguide geometry. The bending loss is negligible when the bending radius exceeds  $150 \mu m$ . (d) Mode profile of the ring waveguide with  $250 \mu m$  bending radius. (e) Ring-bus coupling simulation. .... 76

Figure 6-10 SEM images of the ring resonator. (a) Ring waveguide after the SiO<sub>2</sub> etch. (b) Ring waveguide after the AlN etch. .... 78

Figure 6-11 Experimental Results of the AlN ring resonator. (a) The overall transmission of the ring resonators with different gaps. (b) The zoomed-in transmission at 1545-1554 nm of the ring resonator with a gap of  $0.6 \mu m$ . (c) The zoomed in transmission of the  $0.6 \mu m$  gap at 1546nm. The linewidth of the resonance is measured to be 10.8 pm. (d) The zoomed-in transmission at 1625-1634 nm in the ring resonator with a gap of  $0.4 \mu m$ . .... 79

Figure 6-12 SEM image of the etched AlN waveguide. Nanocolumns and dislocations are seen on the waveguide top. .... 82

Figure 7-1(a) Schematic layout of the nulling interferometer. the optical path from the star (OPS) and the optical path from the exoplanet (OPE) is shown. (b) Schematic of the working principle of the nulling interferometer. .... 85

Figure 7-2 (a) Schematic of Y-branch nulling interferometer [92]. (b) Schematic of the MMI-based nulling interferometer [96]...... 89

Figure 7-3 Simulation Results. (a) Simulation results of the MZI with 15  $\mu m$  MMI transmission at the null port and anti-null port. (b) Simulation results of the MZI with 10  $\mu m$  MMI transmission at the null port and anti-null port. (c) Simulated mode profile of the MMI-MZI..... 92

Figure 7-4 (a) Simulated mode profile of the 15  $\mu m$  MMI-MZI with a TM input. (b) Simulated transmission results of the 15  $\mu m$  MMI-MZI with a TM input. (c) Simulated extinction ratio of the MZI with 15  $\mu m$  MMI with a TM input (d)TM transmission on the MMI needs to be simulated. (e)Experimental results of the bend waveguide TM filter. .... 94

Figure 7-5 SEM images of the fabricated devices. (a)Overall device (b)Zoomed in image of the MMI. .... 95

Figure 7-6 Experimental results of the MMI-MZI. (a) Transmission of the null port and anti-null port, normalized to the transmission of a straight waveguide. (b) Extinction ratio extracted from the transmission. .... 96

Figure 7-7 Microscope image of the microheater..... 97

Figure 7-8 Experimental results of the thermally controlled MZI-MMI. (a) Transmission of the null port and anti-null port, normalized to the transmission of a straight waveguide. (b)Extinction ratio extracted from the transmission. .... 97

Figure 7-9 Simulation results of a MMI with two inputs. The phase difference and power difference between the two inputs light is  $\pi/2$  and 0.1, respectively.

The inset table shows the simulated extinction ratio with different power difference..... 99

Figure 7-10 Schematics of cascaded MZI. [98]..... 100

## List of Table

Table 3-1 Echelle Grating Performance Comparison.....	21
---	----

## Publication List

- [1]. **Shengjie Xie**, Yang Zhang, Yiwen Hu, Sylvain Veilleux, Mario Dagenais, “On-Chip Fabry-Pérot Bragg Grating Enhanced Four Wave Mixing”, ACS Photonics 7 (4), 1009-1015 (2020)
- [2]. **Shengjie Xie**, Jiahao Zhan, Yiwen Hu, Yang Zhang, Sylvain Veilleux, Joss Bland-Hawthorn, Mario Dagenais, “Add-Drop Filter with Complex Waveguide Bragg Grating and Multimode Interferometer Operating on Arbitrarily Spaced Channels,” Opt. Lett. 43 (24), 6045-6048 (2018)
- [3]. **Shengjie Xie**, Yang Meng, Joss Bland-Hawthorn, Sylvain Veilleux, Mario Dagenais, “Silicon Nitride/Silicon Dioxide Echelle Grating Spectrometer for Operation Near 1.55  $\mu\text{m}$ ,” IEEE Photon. J. 10 (6), 1-7 (2018)
- [4]. Yiwen Hu, **Shengjie Xie**, Pradip Gatkine, Joss Bland-Hawthorn, Sylvain Veilleux, Mario Dagenais, “Integrated Arbitrary Filter with Spiral Gratings: Design and Characterization” J. Light. Technol. 38 (16), 4454-4461 (2020).
- [5]. Jiahao Zhan, Yang Zhang, Yiwen Hu, **Shengjie Xie**, Sylvain Veilleux, Mario Dagenais, “Investigation of Backward Cladding-mode Coupling in Bragg Gratings Implemented on a Si<sub>3</sub>N<sub>4</sub> Waveguide Platform”, J. Opt. Soc. Am. B 36 (12), 3442-3449 (2019)
- [6]. **Shengjie Xie**, Yang Zhang, Yiwen Hu, Sylvain Veilleux, Mario Dagenais, “On-Chip Fabry-Pérot Bragg Grating Enhanced Four Wave Mixing”, 2020 CLEO Conference (Poster Presentation)
- [7]. **Shengjie Xie**, Yang Zhang, Yiwen Hu, Sylvain Veilleux, Mario Dagenais, “Fabry-Pérot Bragg Grating Cavity Enhanced Four-Wave Mixing on Si<sub>3</sub>N<sub>4</sub> Chip”, 2020

Quantum 2.0 Conference (Poster Presentation)

- [8]. **Shengjie Xie**, Yang Meng, Joss Bland-Hawthorn, Sylvain Veilleux, Mario Dagenais, “Silicon Nitride Echelle Grating Spectrometer for Operation Near 1.55 um,” 2018 IEEE Photonics Conference (Oral Presentation)

## Chapter 1 : Introduction

Photonic integrated circuit (PIC) is an approach for integrating multiple optical functions on a chip just like an electronic integrated circuit. Comparing with free space optics, PIC shows superior performances in terms of its compactness and stability. Thus, many researchers are working on transforming the conventional free space optics to a PIC platform. Traditionally, most researches have focused on silicon on insulator (SOI) photonics since the SOI devices can be fabricated in the traditional complementary metal-oxide-semiconductor (CMOS) infrastructure and because of the great electrical reconfigurability of SOI devices. What's more, the high index contrast of SOI devices offers great compactness and can minimize the footprint of PIC devices. However, there are inherent limitation of PIC devices on an SOI platform. While the high index contrast of SOI provides the possibility of highly compact device, the device is very sensitive to the sidewall roughness and thus the linear propagation loss on SOI devices is high, typically above 0.5 dB/cm. In addition, due to the small bandgap of silicon (1.1 eV), it is not transparent for wavelength shorter than 1.1 $\mu$ m and it will have strong two photon absorption (TPA) when the light is strong. These facts seriously limit its application in the visible to the near infrared and in nonlinear optics. Thus, more and more optical applications have focused on alternative materials such as silicon nitride (Si<sub>3</sub>N<sub>4</sub>), indium phosphide (InP), and lithium niobate (LiNbO<sub>3</sub>). Among these materials, Si<sub>3</sub>N<sub>4</sub> stands out as a perfect candidate for next generation PIC devices. It has been shown that Si<sub>3</sub>N<sub>4</sub> can be an ultra-low-loss (propagation loss less than 1 dB/m) platform

with careful loss reduction techniques such as chemical mechanical polishing (CMP) and annealing [1], which have led to losses lower than in SOI.  $\text{Si}_3\text{N}_4$  has a larger band gap (5 eV) than silicon. Hence,  $\text{Si}_3\text{N}_4$  is transparent from 400 nm to mid-infrared and has no TPA effects. These properties have greatly benefited many applications where operation within the visible spectrum is required, like in astrophotonics, and where strong light beams are involved, such as in nonlinear optics.

Here, we present  $\text{Si}_3\text{N}_4$  PIC applications in astrophotonics and nonlinear optics. For astrophotonics applications, we demonstrate an Echelle grating spectrometer for on-chip, high resolution, low-loss spectroscopy, a multi-channel add-drop filter based on multimode interferometers (MMI) and complex waveguide Bragg gratings (CWBG) for exoplanet detection and quantum optics, and a high extinction ratio Mach-Zehnder interferometer (MZI) with active thermal control for exoplanet discovery. For nonlinear optics applications, we demonstrate a Fabry-Pérot Bragg grating enhanced four wave mixing (FPBG-FWM). We also demonstrate efforts on minimizing the waveguide losses, which is characterized by using a ring resonator. Furthermore, we also explore a new photonics platform, aluminum nitride on sapphire (AlN-on-sapphire). The fabrication process of the AlN-on-sapphire chip is established, and a loss measurement is also implemented using ring resonators.

## Chapter 2 : Fabrication Techniques for Integrated Photonics

### Devices

#### 2.1 Basic Fabrication Process of Integrated Photonics Devices

All integrated photonics devices fabrication starts from a wafer, either a widely used silicon wafer, or other wafer that uses special materials such as sapphire wafer. While different applications require slightly different fabrication techniques, here, as an example, we take the silicon wafer to briefly introduce the basic fabrication process of an integrated photonics circuit.

As shown in Fig. 2-1, the fabrication process starts from a silicon wafer with thermal oxide on top of the silicon substrate. The thermal oxide serves as the bottom cladding of the waveguide. The first step of fabrication is to deposit  $\text{Si}_3\text{N}_4$  with low pressure chemical vapor deposition (LPCVD) as the waveguide core. Then a resist should be coated on the chip for e-beam lithography (EBL) purpose. Depending on the type of resist, different etch masks are prepared after the EBL process. Afterward, we transfer the pattern from an etched mask to the  $\text{Si}_3\text{N}_4$  layer by inductive coupled plasma reactive ion etching (ICP-RIE). Then the etch mask is removed and a  $\text{SiO}_2$  top cladding is deposited with plasma enhanced chemical vapor deposition (PECVD). We will introduce each fabrication step in detail in the rest of this chapter.

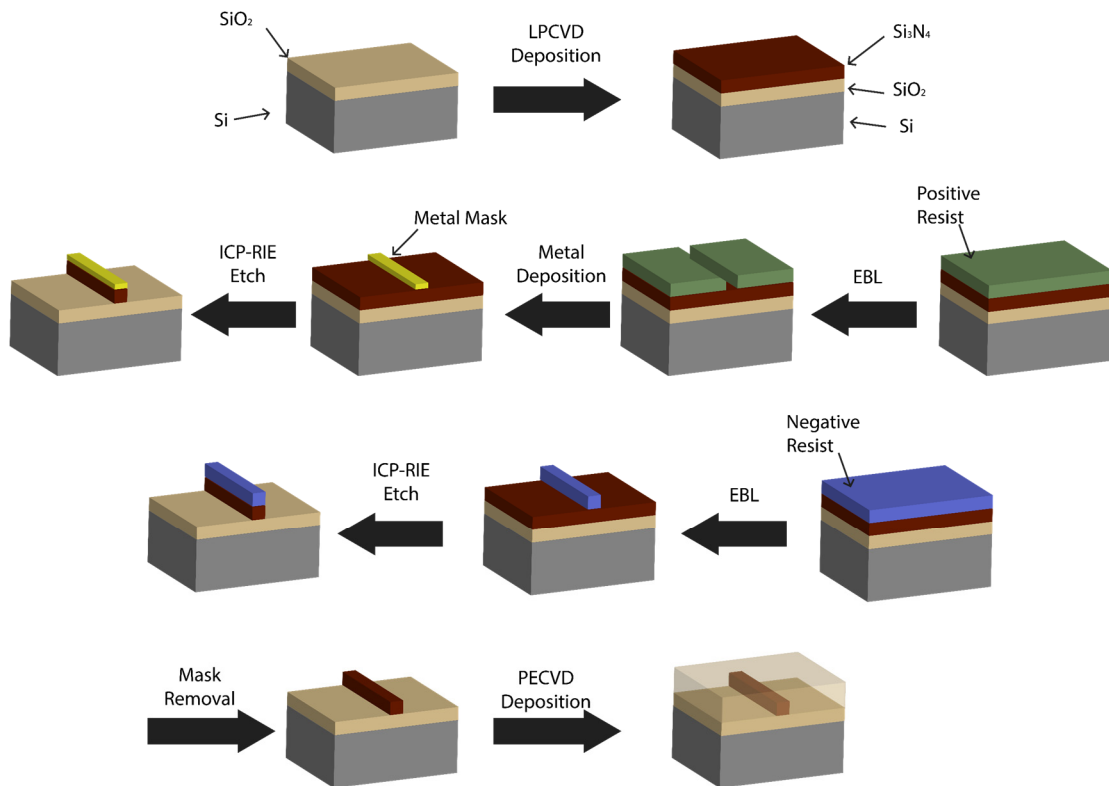


Figure 2-1 Fabrication flow of the Si<sub>3</sub>N<sub>4</sub> chip. Both a positive-tone resist process and a negative-tone resist process are shown.

## 2.2 E-Beam Lithography

E-beam lithography (EBL) is a fundamental approach in integrated photonics device fabrication. It provides exceptional precision and resolution in patterning. In this work, we use a 100 kV Elionix ELS G-100 system to implement the EBL process. The Elionix system can expose 20nm features with a beam current of up to 100 nA, which enables high precision fabrication with a relatively short exposure time. During the EBL process, the e-beam resist is exposed, and its physical and chemical characteristics change. As a result, the design is transferred to the resist after development. There are two types of e-beam resist. One is positive-tone resist. After exposure, the chemical

structure is changed so that the exposed area becomes more soluble in the developer. The other one is negative-tone resist. After exposure, the resist become crosslinked or polymerized so that the exposed area become less soluble in the developer. There are tradeoffs associated with these two types of resists. For the positive-tone resist, since a metal mask is usually deposited on the exposed area after development, the metal mask is capable for a more intense etching process. However, the metal deposition step adds complexity to the fabrication process and the metal lift-off can be problematic in some cases. For the negative resist, the crosslinked resist itself serve as a etch mask, thus the metal deposition step is not necessary. However, the resist mask is more vulnerable to the etching process. Thus, it may not be suitable for an intense etch. In addition, unlike the positive-tone resist, once the negative-tone resist is crosslinked, it cannot be easily removed with solvent. An additional cleaning process, such as an oxygen plasma cleaning, is required to completely remove the resist mask after etching as shown in Fig. 2-2. In this dissertation, we use ZEP-520A (positive) and maN-2405 (negative) as the resists. Detailed recipes can be found in the Appendix.

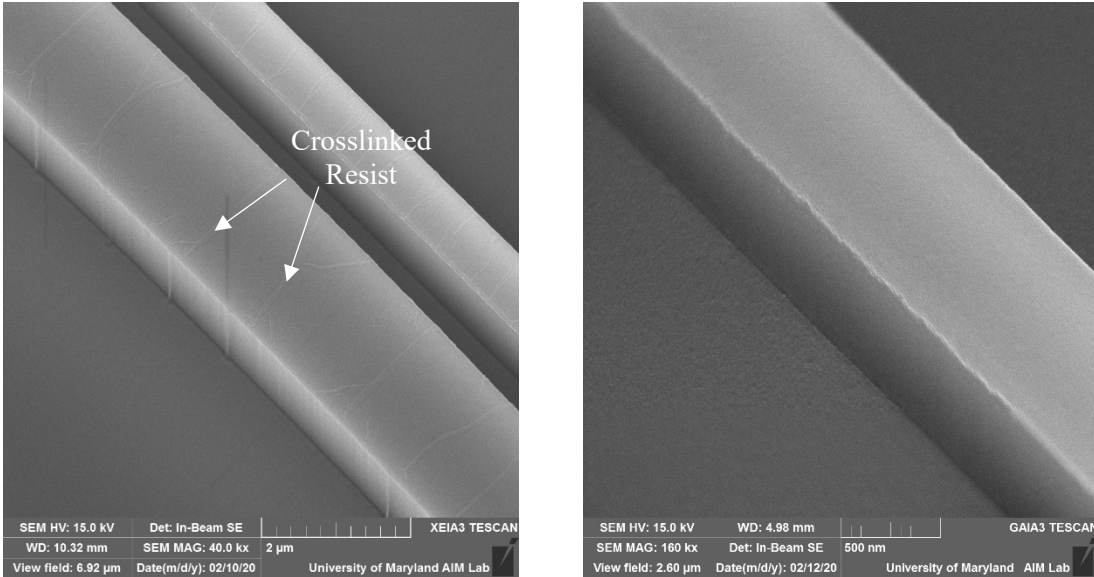


Figure 2-2 SEM images of the etched waveguide with negative resist mask. (a) Waveguide without oxygen plasma clean after ICP-RIE etching. Crosslinked resist is observed on top of the waveguide. (b) Waveguide with oxygen plasma clean after ICP-RIE etching. The crosslink are successfully removed.

### 2.3 Inductive Coupled Plasma Reactive Ion Etching (ICP-RIE)

The ICP-RIE is an anisotropic dry etching technique. It can deliver high directionality, high selectivity ratio, and low damage etching, thanks to the independent control of the plasma density and ion energy through separate DC bias control. In this dissertation, we use two ICP-RIE systems (Oxford Plasmalab System 100) supporting fluorine-based gases, and chlorine-based gases. The fluorine etcher is primarily used for silicon or silicon nitride etch and the chlorine etcher is used mainly for III-V materials and aluminum. Detailed etching recipes for these two types of etcher can be found in the Appendix.

## 2.4 Plasma Enhanced Chemical Vapor Deposition (PECVD) SiO<sub>2</sub>

An integrated photonics device usually requires a top cladding layer to reduce the waveguide loss, protect the waveguide core, and implement thermo-optical or electro-optical modulation. SiO<sub>2</sub> is the most popular top cladding material and PECVD can conveniently deposit SiO<sub>2</sub> layer with low loss and fast speed. While there are different types of PECVD processes for SiO<sub>2</sub> deposition, we only use the silane chemistry to deposit the top cladding in this work. Standard protocol of the PECVD deposition can be found in the Appendix.

It is worth noting that, due to the N-H bond generated during the silane PECVD SiO<sub>2</sub> deposition process, the waveguide will suffer from absorption loss at 1505 nm wavelength. The absorption strength is dependent on the mode profile of the waveguide. When the mode is less confined, a larger portion of the mode extends into the cladding area, resulting in a more significant absorption. In addition, the silane PECVD deposition may have poor step coverage so that a void can form when a high aspect ratio structure exists on the chip [2]. It has been reported that the tetraethoxysilane (TEOS) PECVD deposition process can avoid both the N-H bond generation [3,4] and the step coverage problem [5], but that is beyond the scope of this dissertation.

So far, we have introduced most of the fabrication techniques used in this work, all these techniques enable the devices that will be introduced in the remaining of this dissertation.

## Chapter 3 : Echelle Grating Spectrometer for Operation Near

1.55  $\mu\text{m}$

### 3.1 Introduction to Echelle Grating

It is expected that an on-chip spectrometer will become an important building block for wavelength-division-multiplexed nanophotonics applications. Among many types of on-chip spectrometers, the echelle gratings and the arrayed waveguide gratings (AWG) are the two major candidates. The echelle grating can be designed to have a smaller footprint when compared with an AWG of similar performance, which makes it easier to integrate echelles grating spectrometer with other photonic integrated devices [6]. Furthermore, its small footprint can also minimize the phase error generated due to modal index variation in the light transmission, which is an important source of crosstalk and losses. Hence echelle has attracted increasing interest in recent years. Different material systems have been reported as potential platforms for implementing echelle grating, including silicon-on-insulator (SOI) [7–13], silicon nitride ( $\text{Si}_3\text{N}_4$ ) [14], silicon-germanium [15], indium phosphide [16], etc. While most research centers on SOI, which benefits from its high index contrast and its CMOS compatibility, the large bandgap and acceptable index contrast of  $\text{Si}_3\text{N}_4$  give it unique advantages as mentioned in Chapter 1. This is of great importance for many photonic applications, such as for astrophotonics spectrometers and filtering applications for quantum information [17].

Echelle grating is in fact a special case of a blaze grating. For a blazed grating, the grating is optimized to achieve maximum grating efficiency in a non-zero diffraction order. Echelle grating, as a special form of a blazed grating, is characterized by particularly large blazed angle, typically larger than  $45^\circ$ . Fig. 3-1(a) shows the schematic of an echelle grating. The input light travels to the echelle grating with an incident angle  $\alpha$  and constructively interferes toward an output angle  $\beta$ . The relationship between  $\alpha$  and  $\beta$  is described by:

$$m\lambda = d(\sin \alpha + \sin \beta) \quad (3 - 1)$$

where  $d$  is the grating period,  $\lambda$  is the wavelength of the light, and  $m$  is the order of the grating, which is an arbitrary positive integer. For a given diffraction order, different wavelengths correspond to different output angle, thus the light is diffracted.

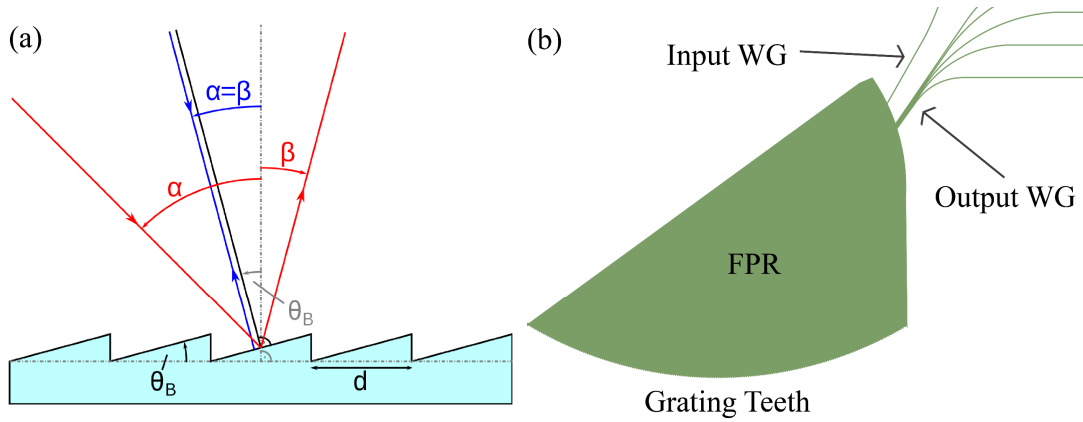


Figure 3-1 (a) Schematic of echelle grating. (b) Schematic of integrated echelle grating.

The integrated counterpart of a free space echelle grating works in the same way. As shown in Fig. 3-1(b), here, light incidents from the input waveguide, propagates through a free propagation region (FPR), is reflected by a reflector and is

refocused on the output waveguide. Since there are constant phase differences between different paths, constructive interference occurs on each output waveguide at different wavelength and hence the incident light is spectrally resolved.

For the integrated echelle grating, most researchers have previously used a distributed Bragg grating (DBG) as the reflector because it can achieve high reflectivity within the designed stop band and it is easy to fabricate – the DBG reflector and the remaining part of the echelle grating can be defined at the same time [7–10]. However, according to the Bragg grating theory, the photonic stopband bandwidth of a DBG is given by

$$\Delta\lambda_{gap} = 2 \left| \frac{n_1}{n_0} \right| \lambda_0 \quad (3 - 2)$$

where  $n_0$  is the average refractive index,  $n_1$  is the amplitude of the index modulation. The  $\text{Si}_3\text{N}_4$  DBG bandwidth is roughly evaluated to be around 200 nm given its modest index contrast. Thus, a  $\text{Si}_3\text{N}_4$  DBG is not considered as an ultra-broad band reflector if spectroscopy over a wide spectral range is required, such as in astrophotonics applications. Silver, instead, is a perfect candidate because of its ultra-high reflectivity (more than 98%) over an ultra-wide bandwidth (from 400 nm to more than 20  $\mu\text{m}$ ) [18]. In the following parts of Chapter 3, we demonstrate the design, fabrication and characterization of a low-loss, high resolution, potentially broadband  $\text{Si}_3\text{N}_4$  echelle grating centered at 1550 nm with silver as a reflector.

### 3.2 Design and Fabrication

To start the design, we first chose the  $\text{Si}_3\text{N}_4$  layer thickness to be 300 nm. There are several reasons for choosing this thickness. When silver is used as a reflector, the metal needs to be coated on the facet of the etched grating grooves to cover the whole optical mode in the vertical direction and achieve ultra-high reflectivity (~98-99% at 1550 nm). Thinner  $\text{Si}_3\text{N}_4$  leads to larger optical mode that requires deeper etching for that light reflection. Very deep etching, however, is difficult to achieve and may potentially create large sidewall roughness and non-vertical facets, which will result in large optical losses. Although thicker  $\text{Si}_3\text{N}_4$  can achieve a more confined slab waveguide optical mode, it is more difficult to control the film stress in a thick  $\text{Si}_3\text{N}_4$  film. Therefore, the vertical mode should be moderately confined. A 300 nm  $\text{Si}_3\text{N}_4/\text{SiO}_2$  slab waveguide has a calculated  $0.73 \mu\text{m}$  vertical mode size for the transverse electric (TE) mode at 1550 nm and is chosen in this work.

We use EPIPPROP, a commercial software specifically for echelle grating simulation, to design the echelle grating. The simulation is based on a “Rowland Circle” configuration. As shown in Fig. 3-2, the inner circle, with a radius of  $r$ , is the circle for the input and output waveguide position. The outer circle (partially shown as the grating teeth curve), with a radius of  $2r$ , is the circle for the echelle grating position. Here, the Rowland circle radius is set to be  $700 \mu\text{m}$  and the grating length is set to be  $1400 \mu\text{m}$ . The waveguide dimension is designed to be  $900 \times 300 \text{ nm}$  to meet the single mode condition. High efficiency coupling tapers, with a width that varies from 300 nm to 900 nm and a length of  $500 \mu\text{m}$ , are used at the input and output facets of the sample

as mode converters to minimize the fiber waveguide coupling loss [19]. We use the 10th diffraction order to define the input and output waveguide positions. We have simulated 5 channels spaced by 5 nm centered at 1550 nm and optimized for TE polarization. Three reference waveguides are designed to extract the on-chip loss of the echelle grating.

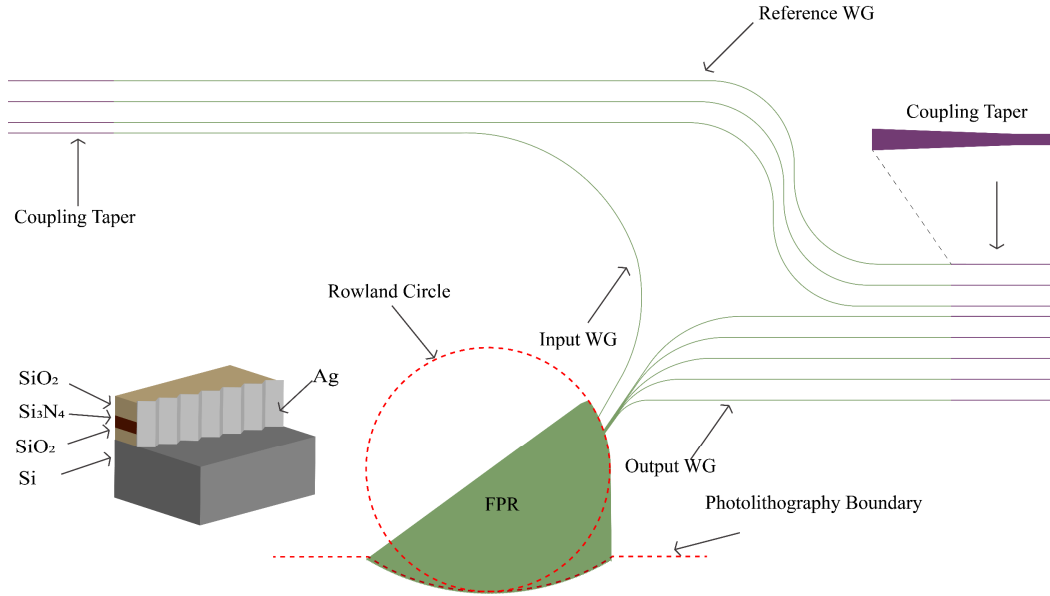


Figure 3-2 Schematic layout of the echelle grating. The light incidents from the input waveguide, propagates through the FPR, is reflected by the grating, and is refocused on the output WGs. 3 Reference WGs are used to extract the propagation loss and coupling loss.

As shown in Fig. 3-3, the fabrication starts with a silicon wafer with a 10  $\mu\text{m}$  thermally grown oxide ( $\text{SiO}_2$ ) layer on top. Then, 300 nm low-pressure chemical vapor deposition (LPCVD)  $\text{Si}_3\text{N}_4$  is deposited and 1.3  $\mu\text{m}$  plasma-enhanced chemical vapor deposition (PECVD)  $\text{SiO}_2$  is finally deposited. After dicing the wafer into  $2.4 \times 1.8$

cm<sup>2</sup> size, we then spin coat ZEP-520A, a positive tone e-beam resist. Then the echelle grating is patterned with 100 kV e-beam lithography (EBL) system (Elionix ELS-G100). An 80 nm chromium hard mask is deposited by e-beam deposition as the etching hard mask. After that, fluorine gas based inductively coupled plasma (ICP) etching is used to form waveguides and deep, vertical grating facet. As mentioned before, silver should cover the vertical mode at the grating teeth to get perfect reflectivity. Here, we have etched 1.3  $\mu\text{m}$  PECVD SiO<sub>2</sub>, 300 nm LPCVD Si<sub>3</sub>N<sub>4</sub>, and 1.5  $\mu\text{m}$  thermal SiO<sub>2</sub>. Then another photolithography step is used to define the boundary for silver deposition. As shown in Fig. 3-2 and 3-3, after the photolithography process, all patterns above the photolithography boundary are protected by the photoresist, silver will only be deposited on the surface below the photolithography boundary so that only the grating facets are covered by silver while the FPR and WGs are free from silver deposition. To make sure the silver is deposited on the grating sidewall, the sample is tilted 90 degrees during silver deposition so that the sidewall is facing toward the silver source. A 130 nm silver thickness is deposited with the e-beam deposition system. Finally, 6  $\mu\text{m}$  of PECVD SiO<sub>2</sub> is deposited as a top cladding layer.

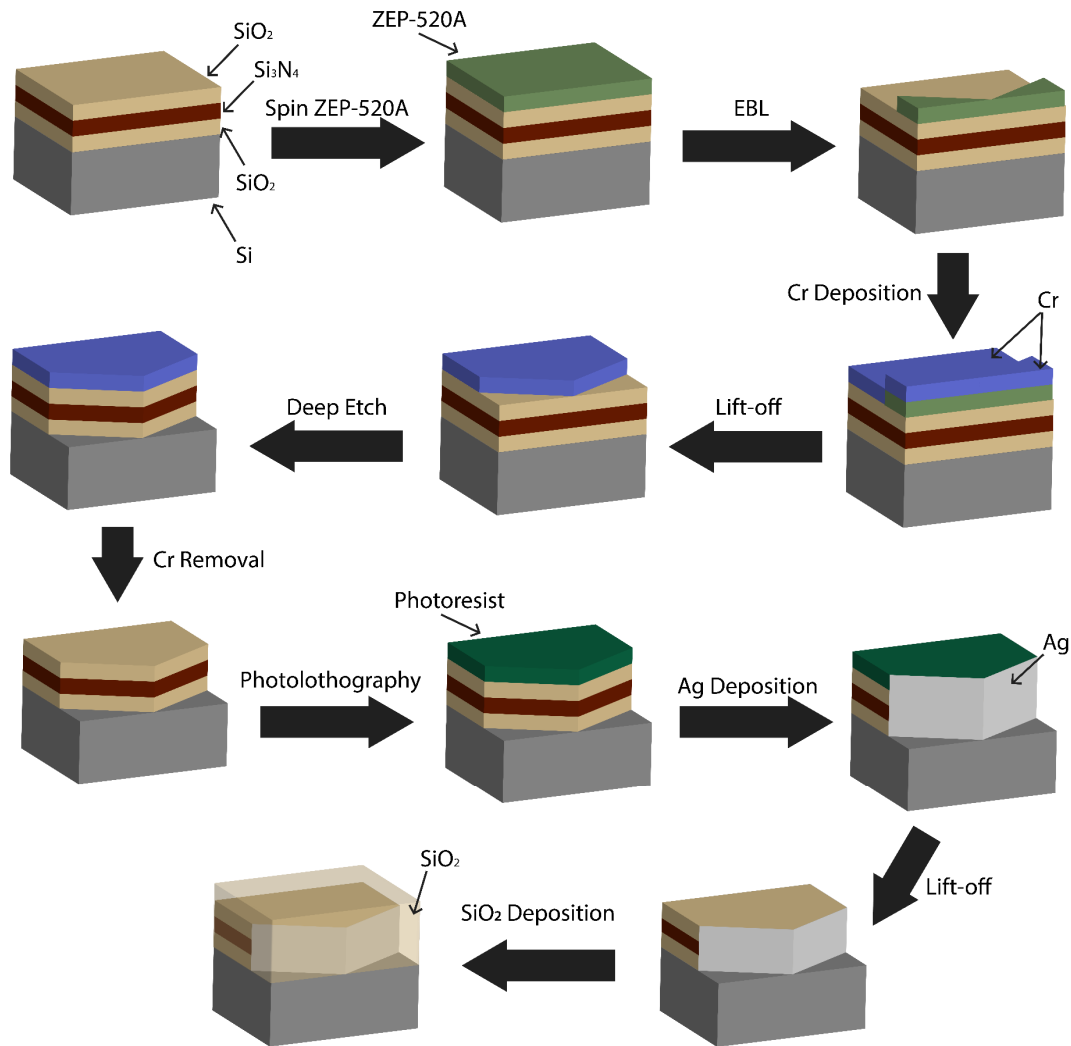


Figure 3-3 Fabrication process of the proposed echelle grating.

Fig. 3-4 shows the SEM images of the fabricated echelle grating. Fig. 3-4(a) shows the SEM image of the whole pattern of the echelle grating with input waveguide, output waveguides, FPR and grating teeth. Thanks to the high voltage EBL system, the waveguides, gratings, and the bulk FPR region can be pattern directly with EBL within a reasonable time. EBL ensures that a precise and smooth grating is created with good waveguide definition. In Fig. 3-4(b-c), we can see that the ICP etching process achieved

vertical and deep etch with smooth boundary definition, all of which are critical for low loss echelle grating.

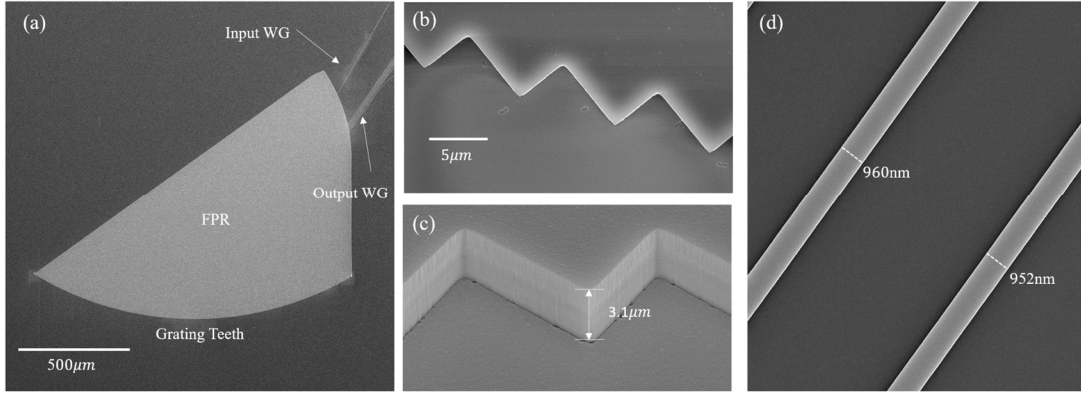


Figure 3-4 SEM image of the echelle grating. (a) Top view of the echelle grating showing the relative position of WGs and grating teeth. (b) Zoom in image of the grating teeth before deep etching. Grating teeth get precise definition with EBL. (c) The etched facets of the echelle grating covered with silver.  $3.1 \mu\text{m}$  deep etch was achieved by ICP etching with perfect verticality. (d) Zoom in image of the output WGs with smooth edge.

### 3.3 Experimental Result

Since the proposed echelle grating is optimized for TE polarization, in order to characterize the transmission spectrum of the echelle grating, a TE polarized tunable laser is used as the light source. Fig 3-5 shows the diagram of the measurement setup. The light comes out from the tunable laser, travels through a polarization-maintaining (PM) fiber. A fiber rotator is used to adjust the light polarization to TE polarization. After fiber-chip butt coupling, the light propagates through the chip and is analyzed by a power meter.

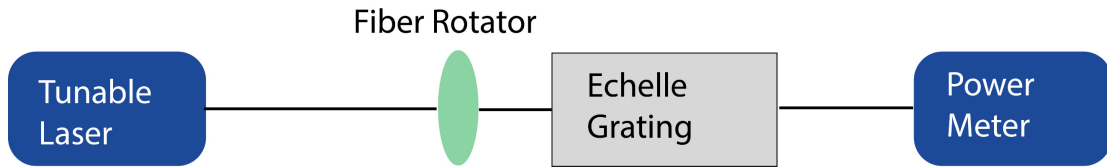


Figure 3-5 Schematic diagram of the measurement setup.

Fig 3-6 (a) shows the transmission pattern of the echelle grating. The insertion loss is normalized to the reference waveguide to subtract the linear propagation loss and fiber-waveguide coupling loss. The echelle grating is centered at 1545.622 nm with a  $4.929 \pm 0.075$  nm channel spacing. The best on-chip loss of the echelle grating is measured to be 1.39 dB showing that the silver reflector works perfectly as a low-loss high-reflectivity reflector. The full width half maximum (FWHM) of each channel is 1.207 nm and hence the spectral resolution ( $\lambda/\Delta\lambda$ ) is about 1300. The adjacent channel crosstalk is more than 30 dB down for all 5 channels. Comparing with the simulation result, the channel center wavelength is shifted by 4.578 nm from the designed center wavelength. This is mainly attributed to the refractive index uncertainty of ( $\text{Si}_3\text{N}_4/\text{SiO}_2$ ) and to phase error generated in the FPR propagation, both of which can be corrected by carefully measuring the indices of the materials we use and by fabrication process optimization. Fig. 3-6 (b) shows that the channel non-uniformity is 1.2 dB. All of this indicates that  $\text{Si}_3\text{N}_4/\text{SiO}_2$  echelle grating with a silver reflector is a good platform for implementing future broadband on-chip spectrometer and deserves proper consideration.

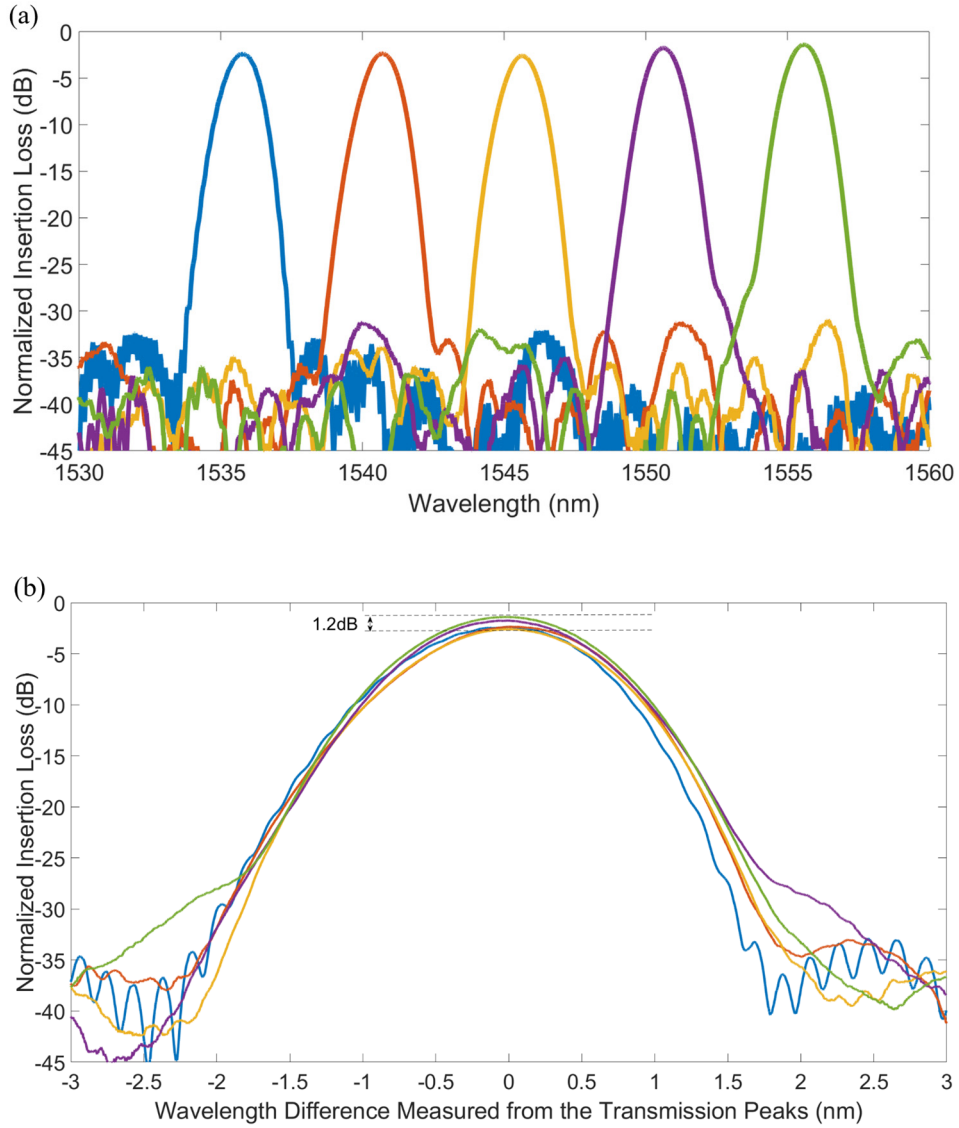


Figure 3-6 (a) Measured TE mode transmission pattern of the echelle grating. (b) Superimposed transmission pattern of the fabricated echelle grating's five channels. Very good overlap and a maximum transmission power non-uniformity of 1.2 dB are achieved in our echelle grating.

Crosstalk is always a concern in spectroscopy. Typically, for echelle grating, the main source of the crosstalk is phase error generated from the non-uniformity of

FPR. However, we discovered that for an EBL fabricated echelle grating, the stitching error can be a dominant source of crosstalk [20]. As shown in Fig. 3-7, the e-beam system works in the following way: the software divides the whole pattern into several grids, which are called writing fields (WFs). The electron beam gun will sit on a single WF, write all patterns inside the WF, and then move to the next WF until all WFs are written. The stitching error comes from the imperfect WF alignment and imprecise stage moving. This can happen in a periodic manner at every WF boundary. For general e-beam fabricated structures, such stitching errors may just add extra losses. Such periodic stitching error, however, will work like another grating structure overlapping with the original design and thus will deteriorate the performance of the echelle grating.

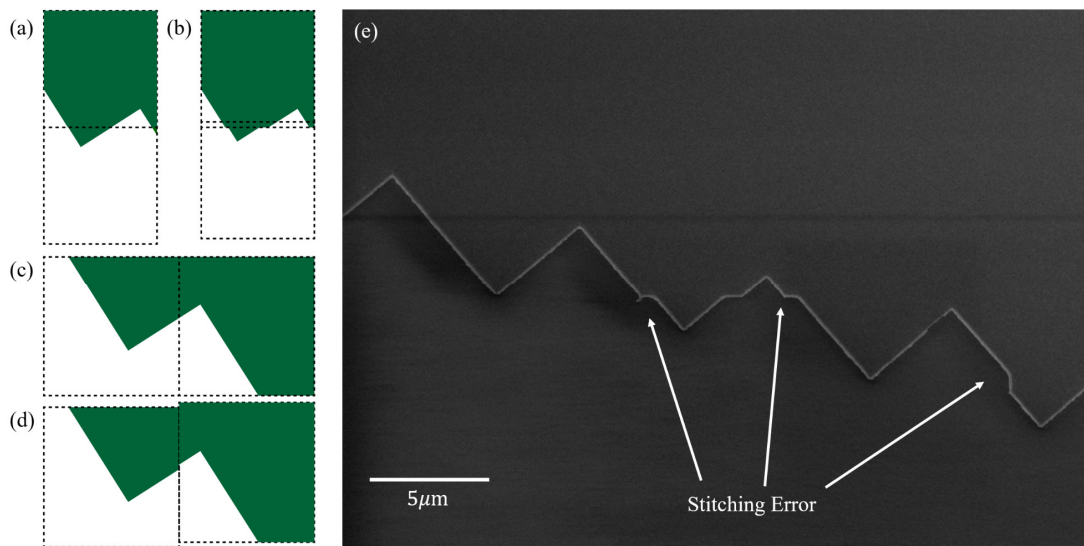


Figure 3-7 Schematic layout and SEM image of stitching error. (a-d) Schematic layouts of stitch-free e-beam patterning and e-beam patterning with stitching error. These errors can happen at both left-right boundaries and up-down boundaries (e) SEM image of stitching errors on grating grooves.

We have used 100  $\mu\text{m}$  and 200  $\mu\text{m}$  WF size in our experiment. As shown in Fig. 3-8 (a) and (c), by adding periodic but random offset to the original echelle grating design, which is in analogy to the occurrence of the stitching error, the EPIPPROP simulation shows that, when 100  $\mu\text{m}$  periodic stitching error exists on the grating, there are several satellite peaks in each channel with 10 nm spacing, while for 200  $\mu\text{m}$  the satellite peaks spacing decrease to 5 nm. This is because, in the original design, we were using the 10th order for our echelle. If we view the periodic stitching error as a grating that has the same Rowland circle geometry but now 100  $\mu\text{m}$  or 200  $\mu\text{m}$  grating period, then the 125th, or 250th, order of light is focused in the center of the output channels. The corresponding free spectral ranges (FSRs) are 10 nm and 5 nm. Such small FSRs are undesirable for the echelle grating because it overlaps with the normal signals and increases the crosstalk level dramatically. Experimentally, we observed the small FSR indicated in the simulation. The crosstalk level increased from less than -30 dB to about -10 dB as shown in Fig. 3-8 (b) and (d). The insertion loss also increased from 1.39 dB to more than 5 dB and 2.8 dB, when the echelle grating suffers from periodic 100  $\mu\text{m}$  and 200  $\mu\text{m}$  stitching error, respectively. Compared with phase errors in the FPR, the stitching errors can be a dominant factor for crosstalk in EBL fabricated echelle grating. Potential solutions to the stitching error problem include: better field alignment; spin coating a conducting layer (i.e. Aquasave) on top of the e-beam resist to get rid of charging effects; use of a larger writing field so that the grating grooves will be patterned in one single writing field; use a more stable e-beam system or an

advanced photolithography system so that no writing field is involved in the exposure process.

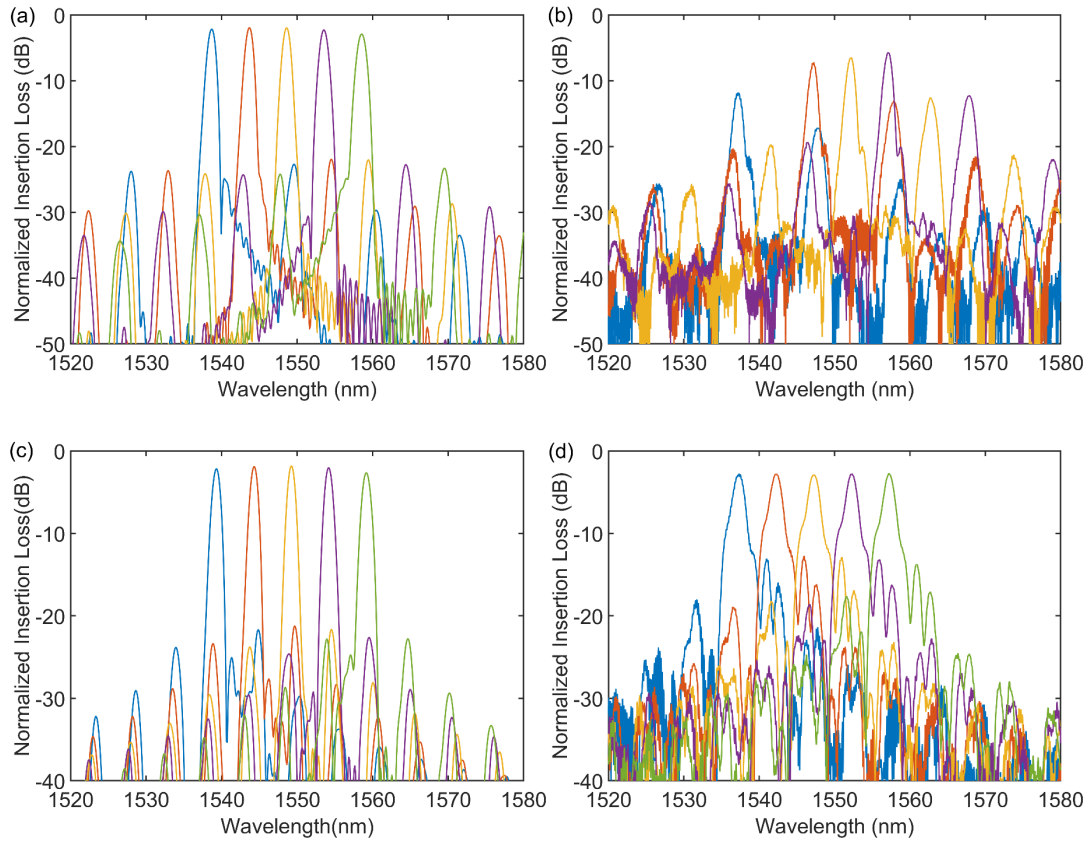


Figure 3-8 Influence of stitching errors on adjacent channel crosstalk. (a) Simulation results of 100 μm WF transmission pattern with stitching errors. (b) Experimental results of 100 μm WF transmission pattern with stitching errors. (c) Simulation results of 200 μm WF transmission pattern with stitching errors. (d) Experimental results of 200 μm WF transmission pattern with stitching errors. [21]

Table 3-1 Echelle Grating Performance Comparison

	Reflector	Insertion Loss (dB)	Crosstalk (dB)	Channel Spacing	Resolving Power	Channel Uniformity (dB)
[7]	DBR	2	15	100 GHz	n/a	n/a
[8]	DBR	3	>27	800 GHz	n/a	0.8
[14]	DBR	1.5	34	6nm	~500	7.5
[22]	DBR	2.8	18	3.96	n/a	n/a
[11]	Aluminum	1.7	25	8nm	<300	Very uniform
[23]	DBR	6.9	15	0.8nm	5571	1.7
This work	Silver	1.2	>30	4.929nm	1300	1.2

### 3.4 Conclusion

In this work, we have demonstrated the design, fabrication and characterization of a 5-channel  $\text{Si}_3\text{N}_4/\text{SiO}_2$  echelle grating with silver as a reflector. The grating experimentally achieved 1.39 dB insertion loss, 4.929 nm channel spacing, a 1300 spectral resolution, a 1.2dB channel non-uniformity and better than -30 dB crosstalk. As shown in the Table 3-1, the combined performance is better than for any other echelle grating reported in literature. We also report that stitching errors that can arise in e-beam written patterns can be a dominant crosstalk mechanism for photonic gratings unless stitching errors are minimized. In our measurements, we have demonstrated that good performance can be obtained for e-beam written echelle gratings. This should lead to new applications in future where on-chip broadband and low loss spectrometers are desired.

# Chapter 4 : Add-Drop Filter with Complex Waveguide Bragg Gratings and Multimode Interferometers Operating on Arbitrarily Spaced Channels

## 4.1 Introduction to Add-Drop Filters

Optical filters have always been a building block of many optical applications. For example, in astronomy, the ground telescopes are always suffering from the O-H bond emissions from the atmosphere, particularly in the near infrared. Without filtering the strong O-H emission from the atmosphere, it is difficult to get good signal-to-noise ratio from the target star. The on-chip version of the optical filter has recently attracted great interests for on-chip photonics integration. Multiple approaches have been proposed to realize on-chip optical filtering such as techniques based on arrayed waveguide gratings (AWG) [24], echelle gratings [8], and Bragg gratings [25]. However, in many applications, both transmitted and rejected signals are required. For example, in exoplanet detection, astronomers wish to separate the spectral components at certain wavelengths from the background and compare them to determine whether water and oxygen exist in the atmosphere of the observed exoplanet. Neither AWG, or echelle gratings, nor many other on-chip multiplexing/demultiplexing techniques can separate and collect both transmitted and reflected signals simultaneously. On-chip add-drop filters provide a unique solution to this issue. The principle of an add-drop filter is illustrated in Fig. 4-1. The light goes into the input port, the transmitted signal is filtered by the filter while the rejected signal goes toward the drop port rather than

go back to the input port. By injecting light on resonance with the filter, the light will be added to the through port, which is corresponding to the “add” operation. Hence, such a add-drop filter can also facilitate, for instance, the separation between a strong pump and weak idler and signal beam in quantum information applications [17], and new optical switches using thermal [26] or electrical tuning [27].

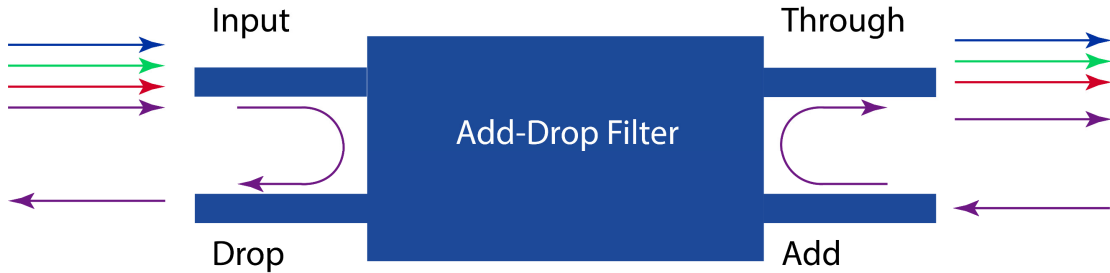


Figure 4-1 Schematics of an add-drop filter.

Many on-chip add-drop filters have been implemented recently. The majority of the add-drop filters focus on ring resonator based add-drop filters due to its simplicity [28,29]. As shown in Fig. 4-2, for a ring resonator, the light can couple between the bus waveguide and the ring resonator through evanescent coupling. After the on-resonant light is coupled into the ring resonator from the input bus waveguide, it will travel clockwise in the ring resonator. The clockwise propagating light will then be coupled to the drop port and travel towards the opposite direction after another evanescent coupling. The on-resonant light incident from the add port will be coupled into the ring resonator and coupled to the through port. Thus, the add-drop operation is implemented with a simple ring resonator. However, since the ring resonator has periodic resonance dependent on its radius, one can only implement add-drop operation

on periodic channels. Similarly, while the add-drop filter has also been implemented using contradirectional coupler [30,31], phase-modulated shifted Bragg gratings [32,33], multimode interferometer (MMI) and WBG systems [34–36], and multimode anti-symmetric waveguide Bragg gratings [37], none of these is capable to implement add-drop operation on arbitrary channels, i.e. on any arbitrary channel of a given wavelength. Hence, such an arbitrarily spaced multi-channels on-chip add-drop filter is highly desirable for many photonics applications.

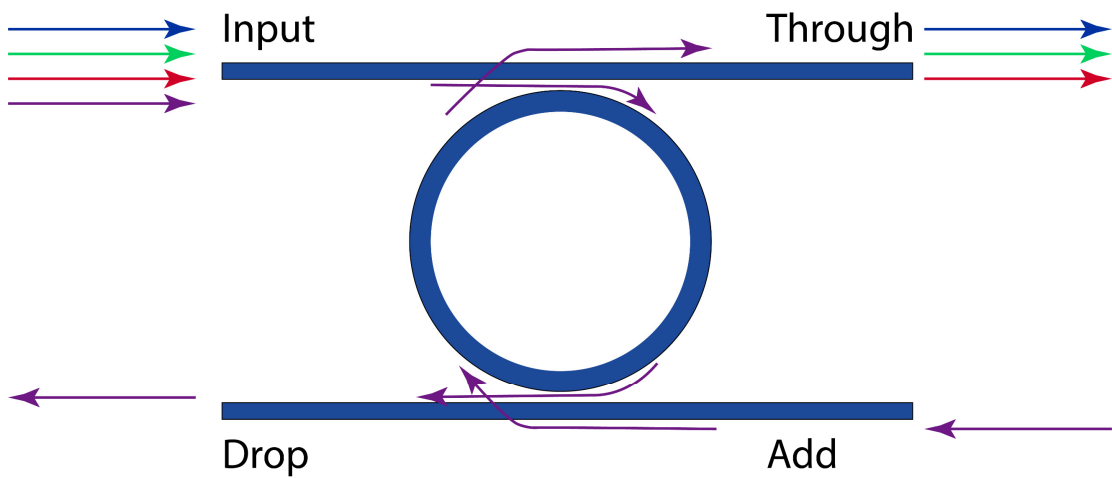


Figure 4-2 Schematic of ring resonator based add-drop filter.

In the rest of Chapter 4, we demonstrate the design, fabrication and measurement of an add-drop filter based on two complex waveguide Bragg gratings (CWBG) and two multimode interferometers (MMI) which are capable to work on arbitrarily spaced channels.

## 4.2 Device Design and Fabrication

While we survey several different methods to implement the add-drop operation, waveguide Bragg gratings (WBG) MMI systems have demonstrated a highly flexible add-drop operation capability by changing the WBGs from simple Bragg gratings to gratings of different types, such as phase-shifted Bragg gratings and apodized Bragg gratings [34–36]. The operating principle of the WBG-MMI filter is shown in Fig 4-3. Light injected into the input port is evenly split into two branches by the first  $2\times 2$  MMI, then both light beams are injected in the following identical WBGs. The transmitted signals from the two arms goes to the through port while reflected signals converge to the drop port. The add port does not receive any light in this whole process, which minimizes the on-chip loss. In fact, this technique is particularly attractive because it can realize the add-drop operation with any type of WBG in between if the two WBGs are identical and their Bragg wavelength is located within the bandwidth of the MMI. This flexibility enables us to extend the add-drop operation from single channel to multi-channels when the WBG is designed to have multiple resonant wavelengths. By optimizing the design of the  $2\times 2$  MMI, the 3-dB bandwidth of WBG-MMI can be as broad as several hundreds of nanometers, thus making the WBG-MMI promising for ultra-broadband multi-wavelength add-drop operation.

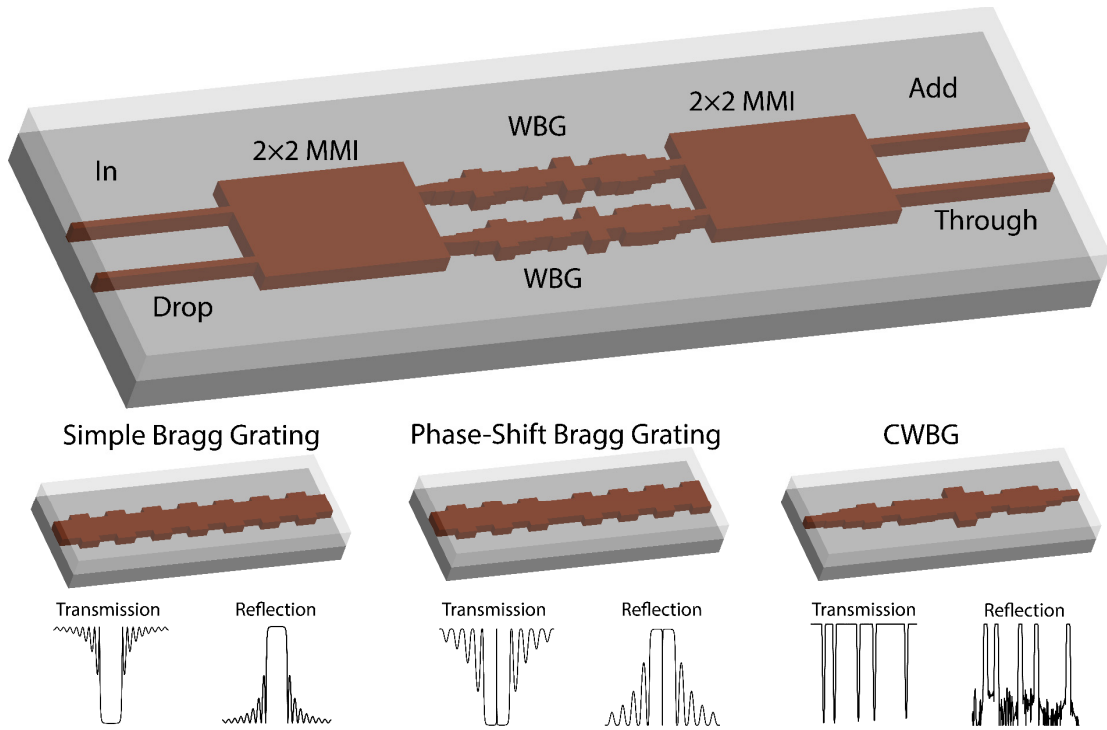


Figure 4-3 Schematic layout of the WBG-MMI add-drop filter. Light injects from the input channel waveguide, is evenly split after the first 2x2 MMI. The transmitted light goes towards the through port after the second 2x2 MMI while the reflected light refocuses on the drop port. The WBGs between two MMIs can be of arbitrary types, i.e. simple Bragg grating, phase shift Bragg grating and complex waveguide Bragg grating, for different applications.

MMI works based on the “self-imaging” principle [38]. Light entering the multimode propagation region excites modes of different orders that are supported in the multimode waveguide. Along the propagation direction, these modes interfere with each other and different number of images of the input optical field can be obtained at different propagation lengths.

In our add-drop filter application, since we need to separate the transmitted and reflected light signal using gratings, we design a  $2 \times 2$  MMI that can divide the incoming optical power from one of the input ports equally into two output branches with a  $\pi/2$  phase shift between the two output channels. This power uniformity plays an important role in the final extinction ratio between the through and add ports.

There are several design parameters. First, a better power uniformity is achieved when a larger number of modes is supported in the multimode region. Therefore, a wider multimode section is desired. However, on the other hand, the larger the width difference between the multimode waveguide and the access waveguide (which is fixed to satisfy the single-mode condition), the more the power is radiated away at the junctions because of the width mismatch. A second parameter is the offset of ports from the center of the multimode waveguide. If the two output ports are already sufficiently separated from each other, there is no need to add bends to further increase their separation (to eliminate the directional coupling between the two subsequent Bragg gratings). But then it is usually the case that the MMI will not be working in the “paired interference” mode [38], thus tripling the length of the multimode region, making the device unnecessarily large and degrading the bandwidth performance.

Here we set the width to be  $28 \mu\text{m}$ , supporting 13 guided modes. For the  $28 \mu\text{m}$ -wide multi-mode waveguide, the spacing between the two output ports is  $9.7 \mu\text{m}$ , which is not enough to completely avoid the mutual coupling. Thus, additional bends are added to widen this spacing further to  $19.7 \mu\text{m}$ . A simulation using a commercial software FIMMWAVE gives 47.27% and 48.91% of input power received at the two

output ports. As for the second issue, we implement two  $2 \times 2$  MMIs with different offsets, satisfying different interference conditions and we compare their 3-dB bandwidths. Measured results are shown in Fig. 4-4. The MMI works in “paired interference” mode. Paired interference mode is a mode that only mode pairs  $TE_0$ - $TE_1$ ,  $TE_3$ - $TE_4$ ,  $TE_6$ - $TE_7$ , ... have been selectively excited. With the paired interference mode, the MMI length can theoretically be reduced by three time and the bandwidth can be expanded by three times as a result. Experimentally, such a paired interference mode has a more than 200 nm 3-dB bandwidth while the MMI not working in “paired interference” mode has a 3-dB bandwidth of only  $\sim 80$  nm. Clearly, the device working in the paired interference mode exhibits a much better bandwidth performance. We adopt this design in the following WBG-MMI and CWBG-MMI add-drop filter since it enables our filter to operate with an ultra-broadband add-drop operation.

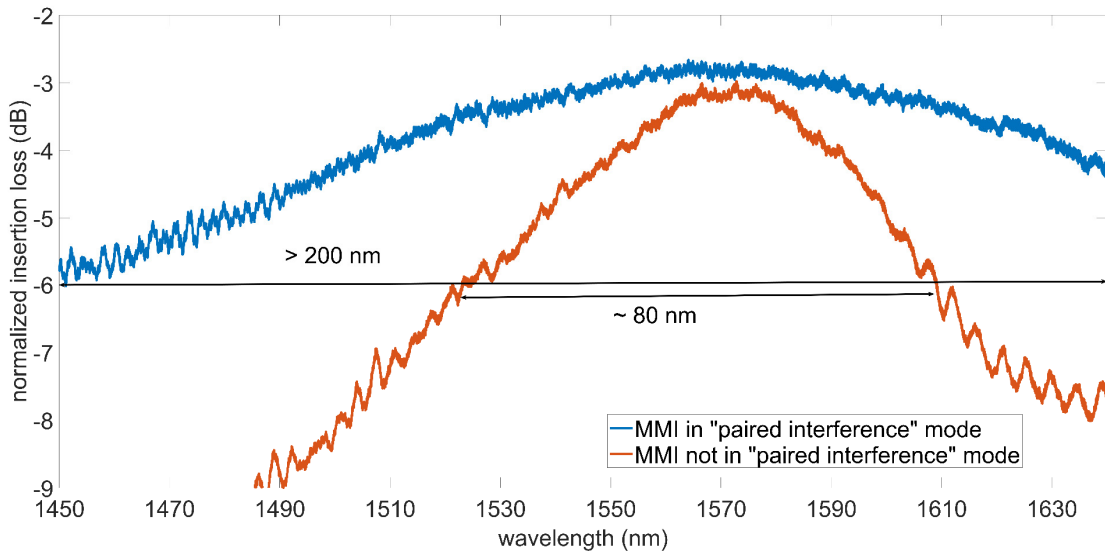


Figure 4-4 The comparison of the bandwidth performance of the two implemented MMIs, with the power normalized to the input power. The one satisfying the paired

interference condition shows a 3-dB bandwidth of more than 200 nm, while the other one only 80 nm.

As mentioned before, the WBG-MMI based add-drop filter is particularly attractive since the WBG between two MMIs can be any kinds of WBG so that a multi-wavelength add-drop operation can be implemented with a specially designed WBG. CWBG, a WBG that has complex period and phase information, has been shown to successfully implement an arbitrary on-chip optical filter [25]. The CWBG is designed with the layer peeling/layer adding (LP/LA) algorithm. The detailed description of the LP/LA algorithm can be found in [25,39]. As a summary, the LP/LA algorithm is based on Equation 4-1 to 4-3, where  $z$  is the grating position,  $\delta$  is the wavenumber detuning from the central wavelength,  $\rho$  is the complex reflection coefficient,  $\Delta$  is the layer peeling segment length and  $r(z, \delta)$  is the reflectivity at  $z$  position with  $\delta$  detuning, which contains wavelength information. When given the target reflection spectrum, we know  $r(0, \delta)$ ,  $\rho(0)$  and  $r(\Delta, \delta)$  can be calculated from Equation 4-1. Since in real simulation the spectrum information must be discrete, we can convert continuous  $r(\delta)$  to discrete  $r(m)$  and calculate  $\rho$  in the next segment with Equation 4-3. By iterating through this process, we can obtain  $\rho$  along the whole grating. We can also reconstruct  $r(0, \delta)$ , the target reflection spectrum, which is called the layer adding process, with the layer peeling calculated  $r(L, \delta)$  by using Equation 4-2 to verify the correctness of the simulation. Finally, we map the complex reflection coefficient  $\rho(z)$  to the physical width  $w(z)$  of the CWBG and build the physical CWBG structure. Fig 4-5 illustrate the

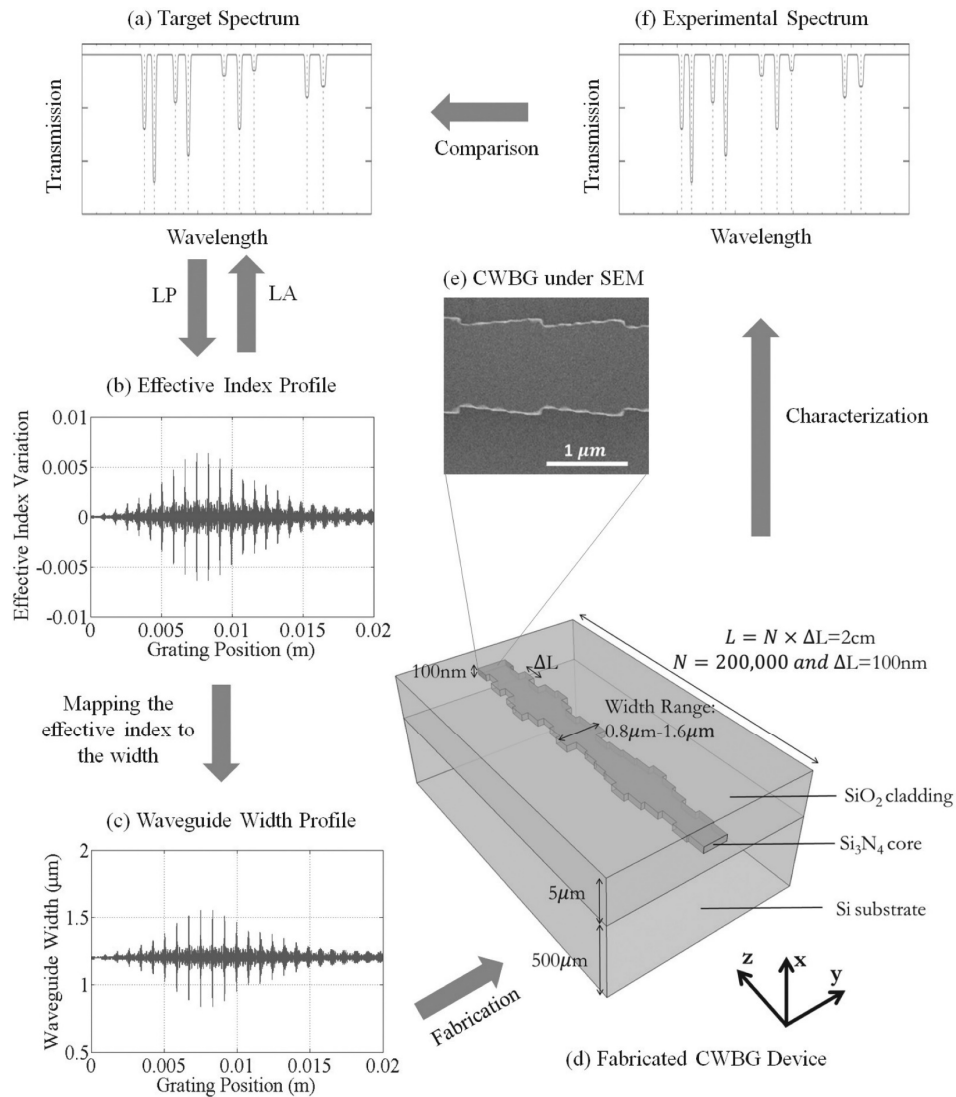


Figure 4-5 Schematic of the LP/LA algorithm process [25].

schematics of how the LP/LA algorithm works. It is worth noting that theoretically the target spectrum in LP/LA algorithm can include any number of dips with arbitrary positions, line widths and rejection ratios. This is fundamentally different from other filtering techniques, such as the one based on ring resonators, which can only generate periodic reflection patterns. Our CWBG maximizes the flexibility of filter design and

has already shown usefulness in applications requiring arbitrary light filtering such as OH-line suppression in the atmosphere for astronomy applications [40,41].

$$r(z + \Delta, \delta) = \exp(-i2\delta\Delta) \frac{r(z, \delta) - \rho(z)}{1 - \rho^*(z)r(z, \delta)} \quad (4 - 1)$$

$$r(z, \delta) = \frac{r(z + \Delta, \delta) + \rho(z) \exp(-i2\delta\Delta)}{\exp(-i2\delta\Delta) + \rho^*(z)r(z + \Delta, \delta)} \quad (4 - 2)$$

$$\rho(z) = \frac{1}{M} \sum_{m=1}^M r(m) \quad (4 - 3)$$

In this work, with LP/LA algorithm introduced above, we have designed a CWBG with five channels resonant at 1550, 1554, 1563, 1569, 1581 nm respectively, which is arbitrarily spaced. Each channel has a rejection ratio of 65 dB and a 3-dB linewidth of 1.4 nm. The length of the CWBG is 5 mm and the widths of the different segments varies from 1.4 to 2.9  $\mu m$ , corresponding to the coupling strength  $\kappa$  which varies from 0 to 160cm<sup>-1</sup>. The length of each segment in our CWBG is 100nm.

The fabrication of the CWBG-MMI add-drop filter starts from a silicon wafer with 10  $\mu m$  thermal grown silicon oxide. 100 nm-thick silicon nitride is deposited as the waveguide core using low-pressure chemical vapor deposition (LPCVD) techniques. Then, the CWBG-MMI add-drop filter is patterned by e-beam lithography with ZEP-520A, a positive tone resist. Next, chromium is deposited on the chip as the etching mask, followed by a lift-off process. After the inductively coupled plasma (ICP) etching of 100 nm, the silicon nitride core is covered with 6  $\mu m$  silicon oxide, deposited by plasma-enhanced chemical vapor deposition (PECVD), as the cladding layer. Finally, the sample is cleaved for fiber-chip coupling. Scanning electron

microscope (SEM) images are shown in Fig. 4-6. The two CWBGs between the two MMIs are identical and are only  $19.7 \mu\text{m}$  apart, which contributes to its relatively small footprint. The zoomed-in SEM images shows that features as small as  $100 \text{ nm}$  are precisely defined and etched by e-beam lithography and ICP etching, both of which are critical for low-loss and accurate CWBG filters.

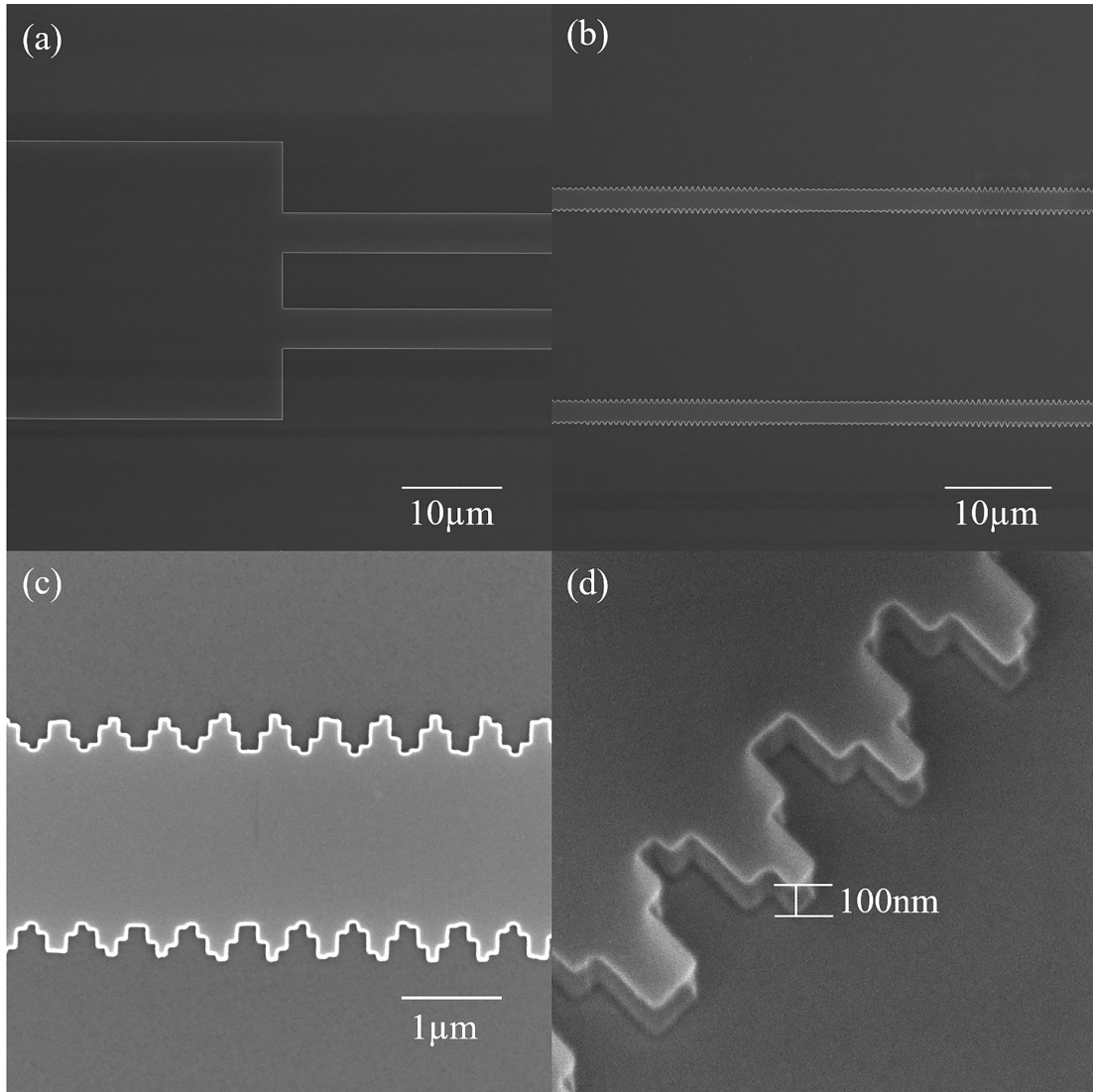


Figure 4-6 SEM images of the CWBG-MMI add-drop filter. (a) The MMI and its output waveguides. (b) Identical CWBGs in two arms. The designed CWBG is highly

aperiodic. (c) Zoomed-in image of one of the CWBGs showing the precise definition of tiny structures with e-beam lithography. (d) 45° tilted view of the CWBG before final PECVD deposition. A smooth sidewall is achieved with the dry-etching process.

### 4.3 Experimental Results

To demonstrate the feasibility of the WBG-MMI based add-drop filter, we first designed a simple Bragg grating for the WBG-MMI add-drop filter. The simple Bragg grating is designed using a quarter-wave-stack and it is centered at 1550 nm with a bandwidth of 10 nm. 800 grating periods ensures a reflection ratio of ~57 dB at the Bragg wavelength. To characterize the add-drop filter, a TE-polarized tunable laser beam is launched into a polarization maintaining (PM) fiber and then coupled into the chip with a carefully designed high efficiency coupling taper [21]. After propagating through the sample, the light is again coupled out to a PM fiber and is analyzed by a power meter. The measured result of this WBG-MMI add-drop filter is shown in Fig. 4-7. Here, all linear propagation losses and fiber-taper coupling losses are removed by normalizing the result to a reference waveguide. The center wavelength and the bandwidth of the implemented Bragg grating are 1558 nm and 8 nm, respectively. The discrepancy of the center wavelength between simulation and measurement results is mainly attributed to the material refractive index difference between experiment and simulation, which could be corrected by adjusting the index used in simulation. The on-chip losses of through and drop signals are less than 1 dB. The rejection ratio within the grating stop band is more than 50 dB. The in-add transmission is more than 25 dB lower than the in-through transmission, meaning that more than 99.5% of the

transmitted light is refocused on the through port, thus contributing to the ultra-low on-chip loss. Clearly, all these features prove the effectiveness of the WBG-MMI add-drop filter platform.

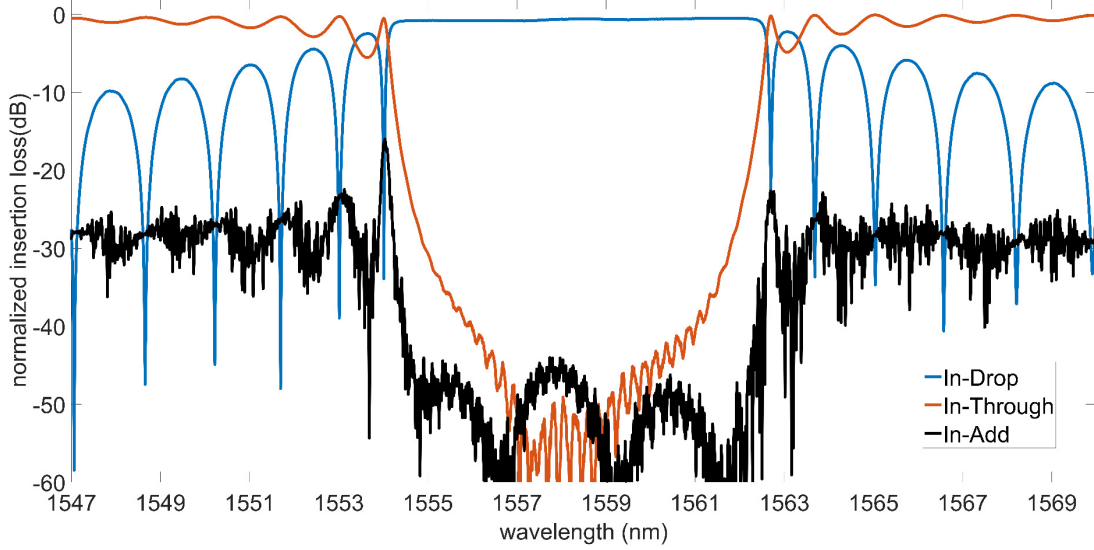


Figure 4-7 Transmission and reflection signals of the WBG-MMI add-drop filter.

We then tested the CWBG-MMI we designed and fabricated in Section 4.2. Fig. 4-8 shows the experimental result of the CWBG-MMI add-drop filter. The on-chip losses of both the transmission and reflection spectra are less than 1 dB from 1551 nm to more than 1590 nm. The total fiber-to-fiber loss of the CWBG-MMI is <9.5 dB. We expect to improve the throughput to <5 dB by optimizing the coupling taper. All five channels have rejection ratios of more than 40 dB and 3-dB bandwidth of 1.2 nm. The positions of the five channels are at 1549.40, 1553.40, 1562.27, 1568.28, and 1580.07 nm, respectively. Compared with the simulation result, the actual locations are blue-shifted by 0.73 nm. This is again mainly attributed to the material index difference between simulation and experiment, although we have already corrected the index used

in the simulation based on the previous result of the WBG-MMI filter. This could be further improved by carefully measuring the refractive index of silicon nitride and silicon oxide. By aligning the position of the third channel in simulation and experimental results, we find that the precision of the channel spacing is better than  $\pm 0.2\text{nm}$ . We also notice that the reflectivity at each channel is lower, and the bandwidth is narrower than the design. In the simulation, we assume that the mode can fully react to the index variation whenever the width is changed. However, in the experiment, the mode travels to the next segment before it is fully coupled to the eigenmode of the current segment. Hence the actual coupling strength of the CWBG is weaker than that in the design. According to the Bragg grating theory, the grating bandwidth is related to the coupling strength  $\kappa$  (which is proportional to  $\rho$  in the LP/LA algorithm) and the reflectivity is related to  $\kappa L$ . A weaker  $\kappa$  results in a shallower and narrower stop band. As shown in Fig. 4-8 (b), the simulation shows that by changing the coupling strength  $\kappa$  to  $0.73 \kappa_{LP}$  (LP calculated  $\kappa$ ), the simulation result fits perfectly with the experimental result.

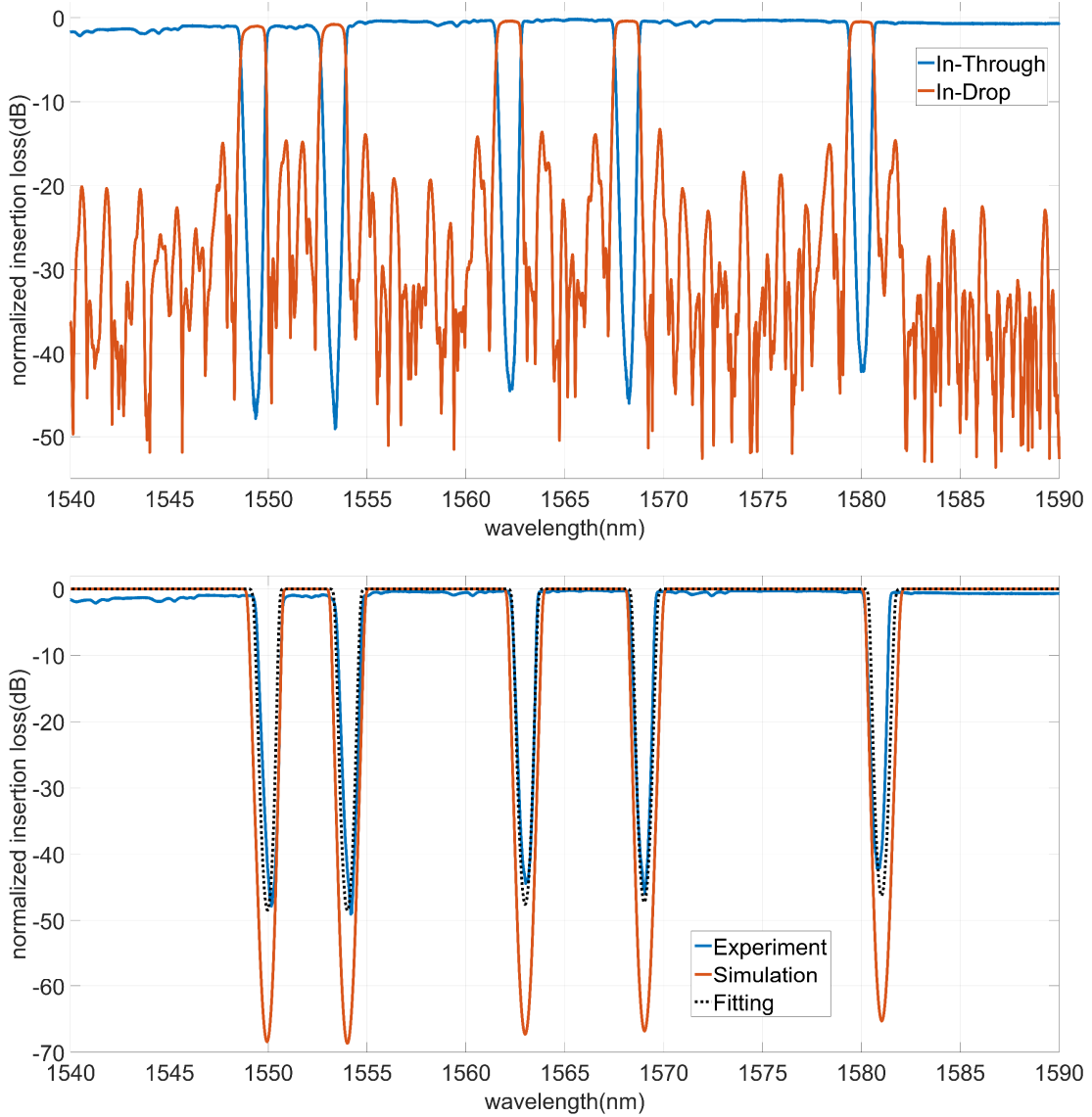


Figure 4-8 (a) The experimental result of the transmission (blue line) and reflection (red line) spectrum. All five channels show an on-chip loss of  $< 1$  dB, a blue-shift of  $0.73$  nm of center wavelengths, a spectral precision of better than  $\pm 0.2$ nm, a rejection ratio of  $> 40$  dB and a 3-dB bandwidth of  $1.2$  nm. (b) Comparison between the initial simulation result, the experimental result, and the fitted simulation result. The

experimental result is red-shifted by 0.73 nm to compensate for the mismatch of the positions of center wavelengths due to the index variation.

The results of both the CWBG-MMI and the previous WBG-MMI filters confirm that the WBG-MMI platform is robust and promising for ultra-low loss, ultra-broadband and spectral-accurate add-drop operation. Since the MMI we use has a 3-dB bandwidth of more than 200 nm, the CWBG-MMI filter can potentially work over this whole wavelength range. By increasing the length of the CWBG and reducing the index variation, more reflection lines can be added into the spectrum with narrower line widths, while maintaining the high channel rejection ratio.

#### **4.4 Conclusion**

In this work, we have demonstrated the optimization of the design of a  $2 \times 2$  MMI, a WBG-MMI add-drop filter with simple WBG, and a CWBG-MMI add-drop filter that has five arbitrarily spaced channels. The CWBG-MMI filter features an on-chip loss of  $< 1$  dB, a rejection ratio of  $> 40$  dB, a 3-dB line width of 1.2 nm, and a spectral precision of better than  $\pm 0.2$  nm. To our knowledge, this is the first CWBG-MMI multi-channel add-drop filter ever made. The LP/LA algorithm gives further flexibility to design filters with more notches with narrower line widths. The designed MMI ensures a large bandwidth of  $> 200$  nm for the proposed CWBG-MMI filter to work in. The CWBG-MMI platform provides a solution for ultra-broadband arbitrary-channel add-drop operation.

## Chapter 5 : On-Chip Fabry-Pérot Bragg Grating Cavity

### Enhanced Four-Wave Mixing

#### 5.1 Introduction to Four-Wave Mixing

In the past decades, four-wave mixing (FWM), a third-order nonlinear process, has become an important optical parametric process that has attracted increased interest. FWM has enabled useful applications for all-optical signal processing such as high-speed sampling, switching, wavelength conversion, amplification and comb generation [42–45].

For the integrated implementation of FWM, silicon (Si) has been widely considered due to its high third-order nonlinearity and high index contrast [46,47]. However, a large amount of research have also focused on exploring nonlinear materials as an alternative to Si, such as silicon nitride ( $\text{Si}_3\text{N}_4$ ) [1], AlGaAs [48], and lithium niobate [49–51], since the nonlinear losses originating from two-photon absorption (TPA) and free carrier absorption at telecom wavelengths limit the maximum power that can be sent in Si.  $\text{Si}_3\text{N}_4$  stands out as one of the most promising candidates as it can take advantage of the mature technologies of CMOS processing for integrated optics, which makes the mass production of optical components possible and thus tremendously reduces the processing cost. The availability of low-loss dielectric waveguide ( $<1$  dB/cm) is critical for light propagation and processing in integrated photonics circuits. Although the nonlinear Kerr coefficient of  $\text{Si}_3\text{N}_4$  is one order of magnitude smaller than the one in Si, the relatively lower propagation loss enables a

more efficient Kerr process. In addition, due to the smaller refractive index contrast with silicon dioxide ( $\text{SiO}_2$ ),  $\text{Si}_3\text{N}_4$  is a more appropriate material for dispersion engineering than Si, since typical fabrication inaccuracies will have a lower impact on dispersion. The FWM effect can be dramatically amplified when using resonators without compromising speed because of their small dimensions compared to a fiber based FWM approach [46,52,53]. While researchers have put enormous efforts in ring resonator based FWM processes, including stimulated FWM, spontaneous FWM (SFWM) and optical comb and soliton generation [1,51,54–57], few work has focused on the Fabry-Pérot Bragg grating cavity enhanced FWM (FPBG-FWM) process [58–60] and not until very recently has it been implemented on an integrated platform [60]. Unlike ring resonator, which will automatically generate a set of FWM signals after careful dispersion engineering, FPBG-FWM process will only generate FWM signals on the resonance peaks inside the stopband. Thus, as compared to conventional optical comb generation, by carefully designing the grating and the cavity, it is possible to generate a finite number of FWM signals, which may have applications in quantum optics.

In the following sections of Chapter 5, we study the FPBG-FWM process on a  $\text{Si}_3\text{N}_4/\text{SiO}_2$  platform, from analytical derivations to experimental demonstrations. A numerical model based on the ABCD matrix method of Bragg grating is developed to optimize the structural design of FPBG-FWM device. We achieve a conversion efficiency of -38.9 dB with a low on-chip pump power of 3.6 dBm. A unique loss reduction and dispersion engineering strategy are also proposed and experimentally

demonstrated in this paper, both of which are critical for efficient FWM process. We further demonstrate that with the proposed dispersion engineering strategy, zero dispersion is deterministically achievable without having to adjust the waveguide geometry.

## 5.2 Theory of FPBG-FWM

In this section we first consider the FWM phenomena inside a waveguide without resonator. We then consider how a resonator will enhance the FWM effect and thus derive the overall nonlinear conversion efficiency of a FPBG-FWM process.

First, we consider the FWM effect inside a waveguide that has a length of  $L$ . The field amplitudes of the pump wave  $E_p$ , the signal wave  $E_s$ , and the converted FWM wave  $E_c$  satisfy the following nonlinear propagation equations, for  $E_p \gg E_s \gg E_c$  (small-signal analysis) [53,61],

$$\frac{\partial E_p}{\partial z} = -\frac{\alpha_p}{2} E_p \quad (5-1)$$

$$\frac{\partial E_s}{\partial z} = -\frac{\alpha_s}{2} E_s \quad (5-2)$$

$$\frac{\partial E_c}{\partial z} = -\frac{\alpha_c}{2} E_c + i\gamma E_p^2 E_s^* e^{i\Delta k z} \quad (5-3)$$

where  $E_s^*$  is the complex conjugate of  $E_s$ , and  $\Delta k = 2k_p - k_s - k_c$ , where  $k_p, k_s, k_c$  are the propagation constants of the pump, the signal and the converted wave, respectively. The nonlinear coefficient  $\gamma$  is related to the Kerr coefficient  $n_2$ , the effective mode size  $A_{eff}$  and the converted frequency  $\omega_c$  by  $\gamma = n_2 \omega_c / (c A_{eff})$ . For

relatively small pump-signal frequency detuning as in our case, we can assume a constant propagation loss coefficient, that is  $\alpha \approx \alpha_p \approx \alpha_s \approx \alpha_c$ . Since there is no converted wave generated at  $z=0$ , where the pump and signal are sent in, by applying the boundary conditions  $E_p(z=0) = E_{p0}$ ,  $E_s(z=0) = E_{s0}$ ,  $E_c(z=0) = 0$ , we get

$$\eta = \frac{P_c^{out}}{P_s^{in}} = |\gamma P_p L'|^2 \quad (5-4)$$

where  $L'^2 = L^2 \exp(-\alpha L) \left| \frac{1 - \exp(-\alpha L + i\Delta k L)}{\alpha L - i\Delta k L} \right|^2$ .

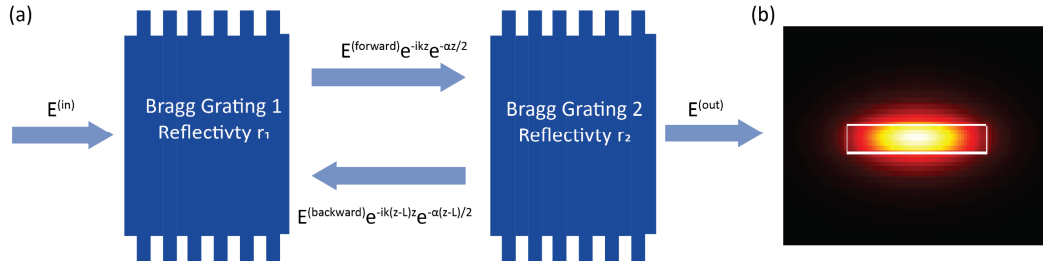


Figure 5-1 (a) Electric fields in a Fabry-Pérot resonator. (b) Mode profile in a Si3N4 waveguide

Fig. 5-1(a) illustrates the electric fields in a Fabry-Pérot resonator when an electric field  $E^{(in)}$  is incident upon mirror 1. Inside the cavity, there are the forward-traveling wave and the backward-traveling wave, which can be represented as follow:

$$E^{(forward)} = t_1 E^{(in)} + r_1 e^{-\frac{\alpha L}{2} - ikL} E^{(backward)} \quad (5-5)$$

$$E^{(backward)} = r_2 e^{-\frac{\alpha L}{2} - ikL} E^{(forward)} \quad (5-6)$$

$r_1$ ,  $r_2$  are the electric-field mirror reflectivities, and  $t_1$ ,  $t_2$  are the electric-field mirror transmittivities. They satisfy  $|r|^2 + |t|^2 \approx 1$ , neglecting the propagation loss due to the

mirrors. Solving the above equation, the expression for the intensity enhancement (IE) is given by:

$$\begin{aligned}
 IE &= \left| \frac{E^{(forward)}}{E^{(in)}} \right|^2 + \left| \frac{E^{(backward)}}{E^{(in)}} \right|^2 \\
 &= \left| \frac{t_1}{1 - r_1 r_2 \exp(-\alpha L - i2k_i L)} \right|^2 \left( 1 + \left| r_2 e^{-\frac{\alpha L}{2}} \right|^2 \right) \quad (5 - 7)
 \end{aligned}$$

where  $i$  can be substituted by  $p$ ,  $s$ , and  $c$ . The field enhancement is maximized at the cavity resonant frequencies. So, the small-signal FWM conversion efficiency enhanced by a Fabry-Pérot cavity is finally given by

$$\eta = |\gamma P_p L'|^2 (IE_p)^2 IE_s IE_c \quad (5 - 8)$$

It contains all the physics of both FWM and the resonator enhancement. The first factor,  $|\gamma P_p L'|^2$ , is the FWM conversion efficiency in a straight waveguide with an effective length of  $L'$ . The effective length  $L'$  contains both the phase mismatch and the propagation loss. The last three factors,  $(IE_p)^2 IE_s IE_c$  give the intensity enhancement inside the cavity for the pump, the signal, the converted wave, respectively. The enhancement comes equally from light recirculation and the energy buildup. As indicated above, the nonlinear coefficient  $\gamma$  is related to the Kerr coefficient  $n_2$ , effective mode size  $A_{\text{eff}}$  and the converted frequency  $\omega_c$ . Since the Kerr coefficient of  $\text{Si}_3\text{N}_4$  is 10 times larger than that of  $\text{SiO}_2$ , a better mode confinement will provide a larger nonlinear coefficient. In this paper, we work on 300 nm thick low-pressure chemical vapor deposition (LPCVD)  $\text{Si}_3\text{N}_4$ , which provides a good mode confinement and is free from excessive film stress.

Correctly estimating the nonlinear coefficient  $\gamma$  is essential to calculate the FWM conversion efficiency. Since the optical mode covers the Si<sub>3</sub>N<sub>4</sub> core and SiO<sub>2</sub> cladding and these two materials have different Kerr coefficient  $n_2$ , the nonlinear coefficient  $\gamma$  can not be simply defined by  $\gamma = n_2 \omega / (c A_{\text{eff}})$ . Here, we can calculate the converted idler power in the core and the cladding separately and derive the overall conversion efficiency and thus derive the nonlinear coefficient  $\gamma$  for a given waveguide geometry.

As shown in Fig. 5-1(b), the outer ellipse represents the optical mode size and the inner rectangle represents the waveguide core. We assume that the SiO<sub>2</sub> cladding is infinitely large so that the optical mode outside of the core will be in the SiO<sub>2</sub>. We define a power filling factor  $F$  as the power confined in the core region. Thus, for a total input pump  $P_p$  and signal  $P_s$ , the  $P_p F$  and  $P_s F$  will be in the core region while  $P_p(1-F)$  and  $P_s(1-F)$  will be in the cladding region. By the definition of the nonlinear conversion efficiency,  $\eta$  is defined as:

$$\eta = (\gamma_t P_p L)^2 = \frac{P_i}{P_s} = \frac{P_i^N + P_i^O}{P_s^N + P_s^O} \quad (5 - 9)$$

where  $\gamma_t$  is the overall nonlinear coefficient of the waveguide,  $P_i^N, P_i^O$  is the converted, or idler light intensity in Si<sub>3</sub>N<sub>4</sub> and SiO<sub>2</sub>, respectively and  $P_s^N, P_s^O$  is the signal light intensity in Si<sub>3</sub>N<sub>4</sub> and SiO<sub>2</sub>, respectively.

We then calculate  $P_i^N, P_i^O$  separately:

$$P_i^N = P_s^N (\gamma P_p^N L)^2 = P_s F \left( \frac{n_2^N \omega}{c A_N} L \right)^2 (P_p F)^2 \quad (5 - 10)$$

$$P_i^O = P_s^O (\gamma P_p^O L)^2 = P_s (1 - F) \left( \frac{n_2^O \omega}{c A_O} L \right)^2 \left( P_p (1 - F) \right)^2 \quad (5 - 11)$$

Where  $n_2^N$  and  $n_2^O$  are the Kerr coefficient of Si<sub>3</sub>N<sub>4</sub> and SiO<sub>2</sub>, respectively and  $A_N$  and  $A_O$  are the effective area of the Si<sub>3</sub>N<sub>4</sub> and SiO<sub>2</sub>, respectively.  $A_N$  is the Si<sub>3</sub>N<sub>4</sub> core area and  $A_O$  is the mode effective area less the Si<sub>3</sub>N<sub>4</sub> core area. Combining them together, we get:

$$\begin{aligned} P_i = P_i^N + P_i^O &= P_s (P_p L)^2 \left( \left( \frac{n_2^N \omega}{c A_N} \right)^2 F^3 + \left( \frac{n_2^O \omega}{c A_O} \right)^2 (1 - F)^3 \right) \\ &= (\gamma_t P_p^N L)^2 P_s \end{aligned} \quad (5 - 12)$$

Thus, we get:

$$\gamma_t = \sqrt{\left( \frac{n_2^N \omega}{c A_N} \right)^2 F^3 + \left( \frac{n_2^O \omega}{c A_O} \right)^2 (1 - F)^3} \quad (5 - 13)$$

This is the nonlinear coefficient  $\gamma_t$  for any given waveguide geometry.

### 5.3 Bragg Grating Design and Losses Reduction

From Equation 5-7, it is obvious that the larger the reflectivity  $r$  and the lower the loss  $\alpha$ , the higher the IE on resonance. Thus, to achieve high FWM efficiency, a Bragg grating with strong coupling strength and low loss is highly desirable. Here, the ABCD matrix method, developed in our previous work [62], is the perfect tool to implement the theoretical analysis of the FWM efficiency for a given Bragg grating geometry. From Equation 5-6, the only unknown parameters of the IE factor are the mirrors reflectivity and transmittivity. We use the ABCD matrix to calculate the  $r$  and  $t$  and to simulate the IE factor and thus simulate the FWM efficiency. As shown in Fig.

5-2, by fixing the grating loss to be 0.4 dB/cm, the cavity loss to be 0.3 dB/cm, the input pump power to be 0 dBm, the nonlinear coefficient to be  $1.6 \text{ m}^{-1}\text{W}^{-1}$ , and by increasing the grating coupling strength from  $54\text{cm}^{-1}$  to  $193\text{cm}^{-1}$ , the simulated FWM conversion efficiency  $\eta$  is improved by more than 10 dB.

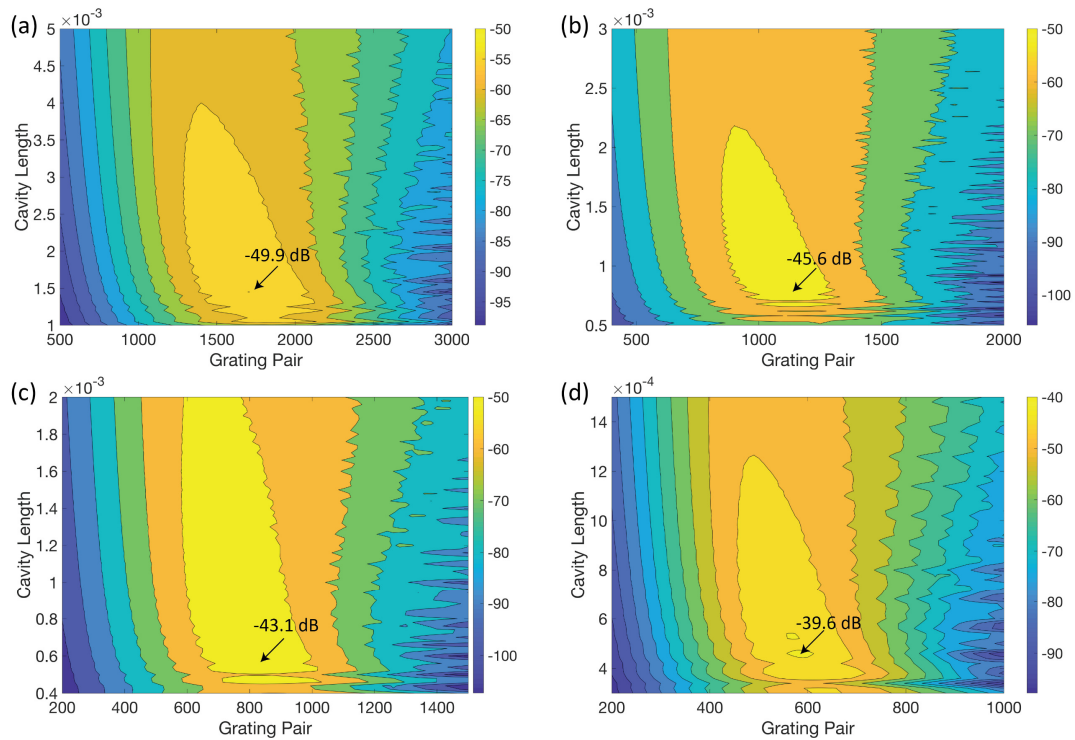


Figure 5-2 Simulation of the relationship between FWM efficiency and grating coupling strength by fixing other parameters. (a) taking the coupling strength to be  $\kappa = 54 \text{ cm}^{-1}$ , maximum efficiency  $\eta = -49.9 \text{ dB}$  in simulation (b) coupling strength  $\kappa = 94\text{cm}^{-1}$ , maximum efficiency  $\eta = -45.6 \text{ dB}$  (c) coupling strength  $\kappa = 133\text{cm}^{-1}$ , maximum efficiency  $\eta = -43.1 \text{ dB}$  (d) coupling strength  $\kappa = 193\text{cm}^{-1}$ , maximum efficiency  $\eta = -39.6 \text{ dB}$

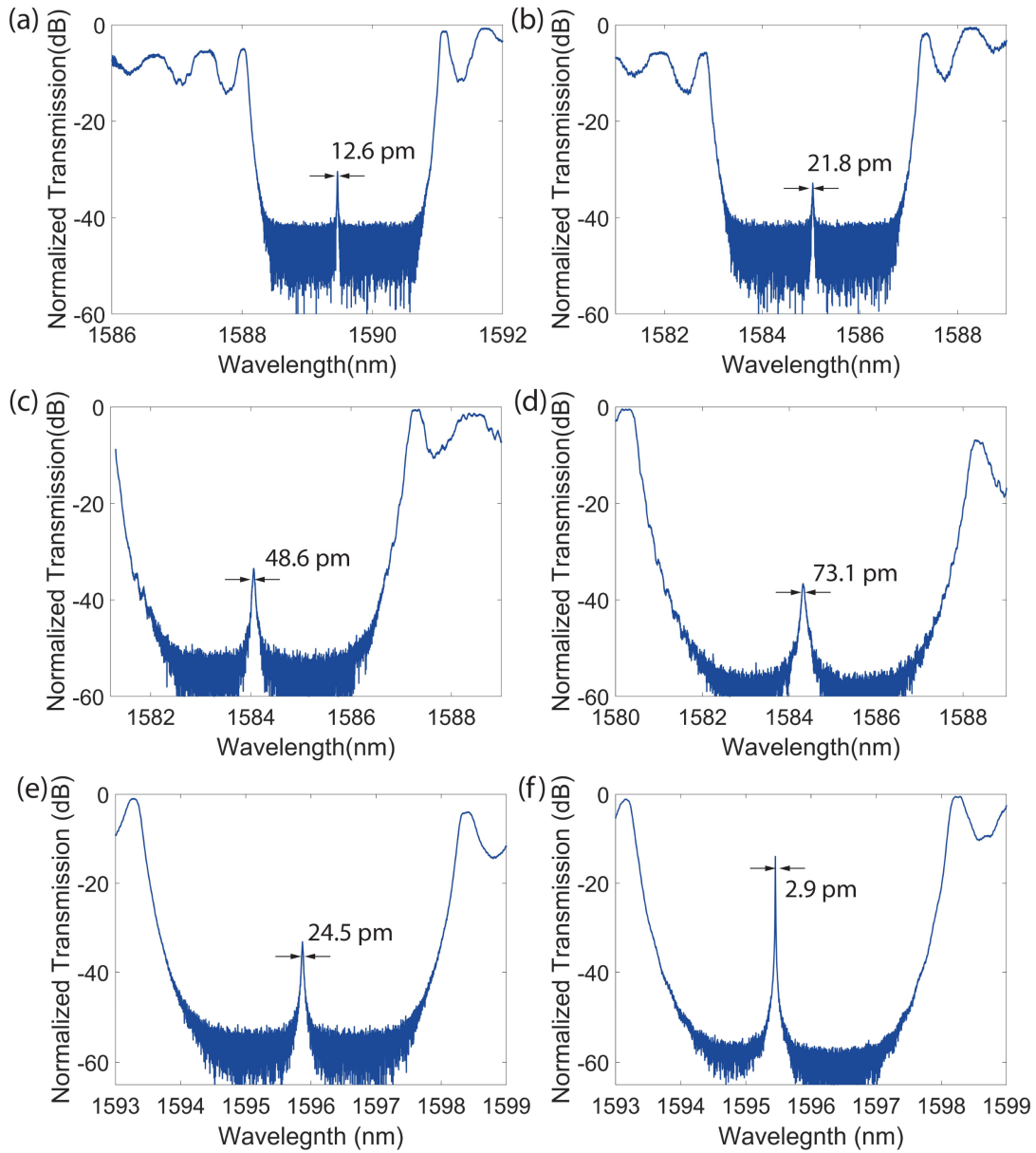


Figure 5-3 Experimental characterization of grating loss of different grating coupling strength. (a) coupling strength  $77\text{ cm}^{-1}$ , measured grating loss  $1.95\text{ dB/cm}$ . (b) coupling strength  $110\text{ cm}^{-1}$ , measured grating loss  $3.1\text{ dB/cm}$ . (c) coupling strength  $155\text{ cm}^{-1}$ , measured grating loss  $6.6\text{ dB/cm}$ . (d) coupling strength  $201\text{ cm}^{-1}$ , measured grating loss  $12.0\text{ dB/cm}$ . (e) Transmission pattern of a normal PSBG with a coupling strength of

125cm<sup>-1</sup> (f) Transmission pattern of PSBG with tapered grating with a coupling strength of 125cm<sup>-1</sup>.

Next, the ABCD matrix method is also used to extract the small losses,  $\alpha_{\text{grating}}$  and  $\alpha_{\text{cavity}}$ , for the given Bragg grating geometry [62]. To characterize the grating loss of a given grating geometry, we design a set of phase-shifted Bragg grating (PSBG) with different coupling strengths. The quality factor of the PSBG resonant peak is directly related to the grating loss. As shown in Fig. 5-3 (a-d), when the grating coupling strength increases from 77 cm<sup>-1</sup> to 201 cm<sup>-1</sup>, the measured 3-dB linewidth of the resonant peak increases from 12.6 pm to 73.1 pm, corresponding to a grating loss increase from 1.95 dB/cm to 12 dB/cm. This is not desirable since significantly higher grating loss will lead to excessive penalties for the FWM efficiency. Even though the stronger grating will provide higher FWM efficiency, the total FWM efficiency will not be improved. In fact, like 1-D photonic crystal, the large grating loss of the strongly coupled grating mainly comes from the mode mismatch between the waveguide mode and the grating Bloch mode [63–65]. Whenever the light travels through the interface between the Bragg grating and the cavity, it will experience such a mode mismatch loss. Thus, an adiabatic tapered grating is added between the Bragg grating and the cavity, which facilitates the adiabatic mode conversion between a cavity mode and a grating Bloch mode, and significantly reduces the grating loss. Fig. 5-3(e, f) shows that, by introducing a tapered grating (schematic as shown in Fig 5-5(b)), which linearly reduces the grating width variation, the measured 3-dB linewidth of the resonant peak reduces from 24.5 pm to 2.9 pm, corresponding to a grating loss reduction from 3.5

dB/cm to 0.36 dB/cm, which is comparable to the grating loss of weakly coupled Bragg grating.

#### 5.4 FWM Experimental Results and Analysis

Experimentally, the Bragg grating has a coupling strength of  $193 \text{ cm}^{-1}$ . The grating is defined by a sidewall corrugation and the width variation is from  $1.0 \text{ um}$  to  $1.2 \text{ um}$ . The cavity geometry is designed as  $1.0 \text{ um} \times 0.3 \text{ um}$ . The Bragg grating and the cavity geometry guarantee that only the fundamental mode is excited on chip so that no multimode noise will be observed in the transmission signal. The nonlinear coefficient  $\gamma$  of our current design is calculated to be  $0.99 \text{ m}^{-1}\text{W}^{-1}$ . Following the ABCD matrix method, we extract a grating loss of  $0.36 \text{ dB/cm}$  and a cavity loss of  $0.33 \text{ dB/cm}$  for a tapered PSBG and a Fabry P erot Bragg grating (FPBG), respectively. Based on all the losses and grating coupling strength information, we optimize our FWM Bragg grating with Equation 5-7. It is worth noting that, in Equation 5-7, since the nonlinear coefficient  $\gamma$  and pump power  $P$  can be viewed as preset parameters if the waveguide geometry and input power are fixed, only  $|L'|^2(IE_p)^2IE_sIE_c$  will be optimized by engineering the grating and the cavity design. As shown in Fig. 5-4, the optimized FWM cavity design is found to be 625 periods of Bragg grating, including 20 periods of linearly tapered grating, for each mirror and a 390-um long cavity. The maximum enhancement from the cavity is 40.21.

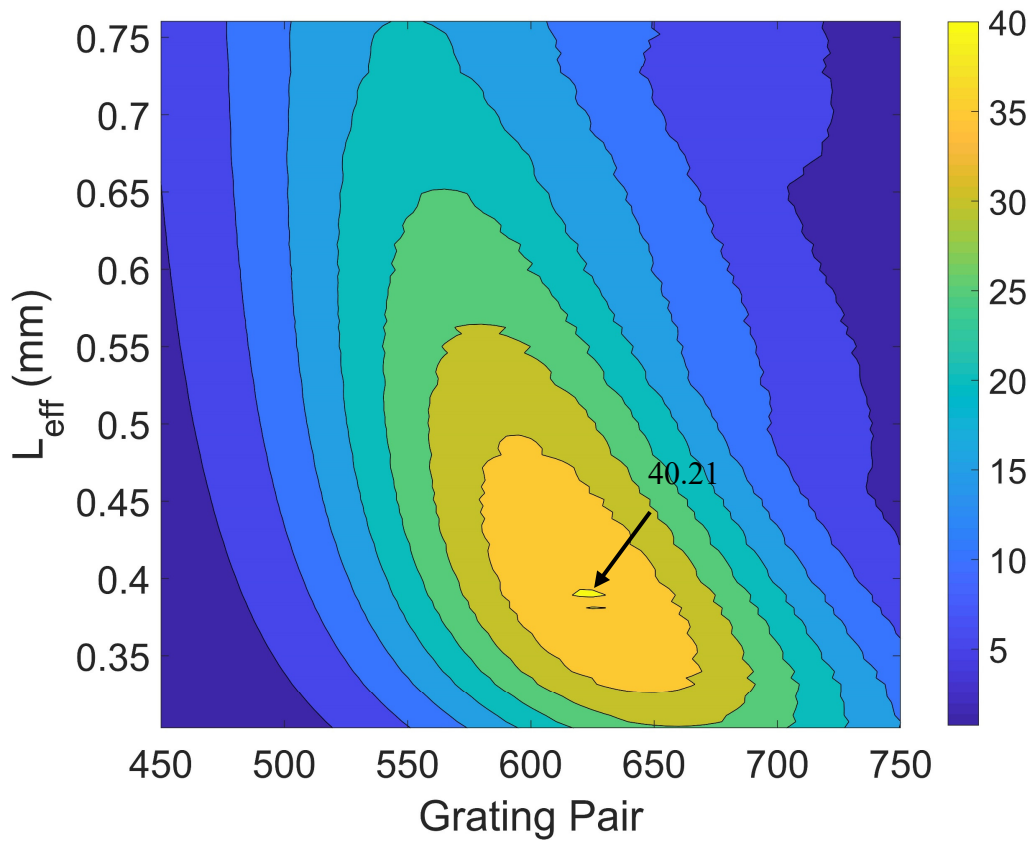


Figure 5-4 Simulation of the  $|L'|^2(IE_p)^2IE_sIE_c$  with a grating loss of 0.36 dB/cm and a cavity loss of 0.33 dB/cm. The  $|L'|^2(IE_p)^2IE_sIE_c$  reaches the peak, 40.21, with 625 periods of Bragg grating in each mirror and 390  $\mu\text{m}$  cavity length.

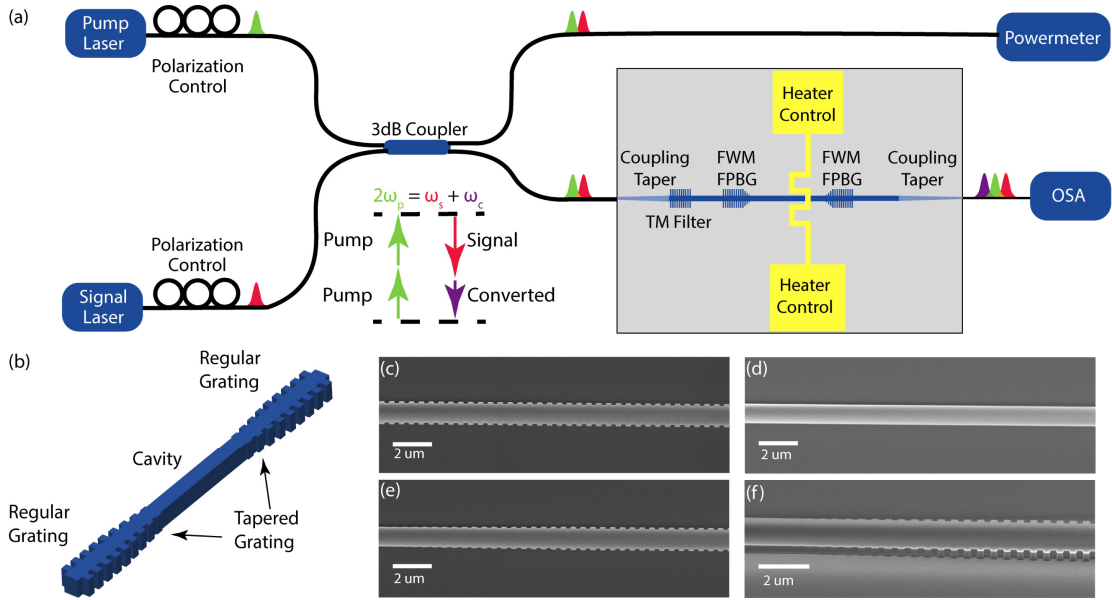


Figure 5-5 (a) Schematic of the experimental setup. The CW pump laser is a thermally tuned butterfly laser diode with a maximum output power of 13 dBm and the CW signal laser is an electrically tunable laser with a maximum output power of 4 dBm. (b) Schematic of the FPBG, tapered grating is added between regular grating and cavity to facilitate mode conversion between cavity mode and grating Bloch mode. (c-f) SEM images of the FPBG. (c) Periodic Bragg grating. (d) Straight waveguide between two Bragg grating mirrors. (e) Linearly tapered grating connecting regular Bragg grating and cavity. (f) Tilted view of the linearly tapered Bragg grating.

The experiment schematic is shown in Fig. 5-5 (a). We use two tunable continuous wave (CW) laser as the pump light and signal light, respectively, whose polarization are controlled independently. After the polarization controllers (PCs), the polarization states of both waves are aligned to be TE polarized. The wavelengths of both waves are tuned to match one of the resonant peaks. The lights are combined by a

3-dB coupler and then half of the combined light is monitored by a powermeter while the other half is coupled on chip using a fiber-chip butt coupling. A low loss coupling taper is designed to facilitate efficient coupling [19]. The output light is analyzed by an optical spectrum analyzer (OSA). Our fabrication starts from a Si substrate with 10  $\mu\text{m}$  thermal  $\text{SiO}_2$ . 300 nm LPCVD  $\text{Si}_3\text{N}_4$  is then deposited on the substrate. The chip is patterned by e-beam lithography (EBL) with ZEP-520A, a positive tone resist. After development, a 20 nm chromium mask is deposited using a lift-off approach, which works as a dry etch hard mask followed by an induced coupled plasma (ICP) etching. After chromium removal, the sample is deposited with 4  $\mu\text{m}$  plasma-enhanced chemical vapor deposition (PECVD)  $\text{SiO}_2$  as a top cladding layer. As shown in Fig. 5-5 (c-f), the regular Bragg grating, tapered Bragg grating, and the cavity are patterned by EBL with smooth boundaries. A smooth sidewall is achieved with ICP dry etching.

Since the polarization-maintaining (PM) fiber we use can only ensure a 20-25 dB polarization extinction ratio, there is still TM polarized light injected on chip. Due to different effective index of the TE mode and TM mode, the central wavelengths of the TE stopband and TM stopband of the designed Bragg grating geometry are separated by 30-40 nm. Hence, the TM mode will not be rejected in the TE stopband. That is an important noise source and must be removed, otherwise it will cover the weak FWM signal and make the FWM measurement impossible. Here we add an additional integrated Bragg grating whose TM stopband aligns with the TE stopband of the FWM Bragg grating to remove the residual on-chip TM noise. As shown in Fig. 5-6, without the TM filter, the TE stopband depth is limited to less than 20 dB by the TM noise.

After adding an integrated TM filter and carefully aligning its stopband with the existing TE Bragg grating's stopband, the TE stopband depth is improved to better than 40 dB, which is favorable for FWM measurement.

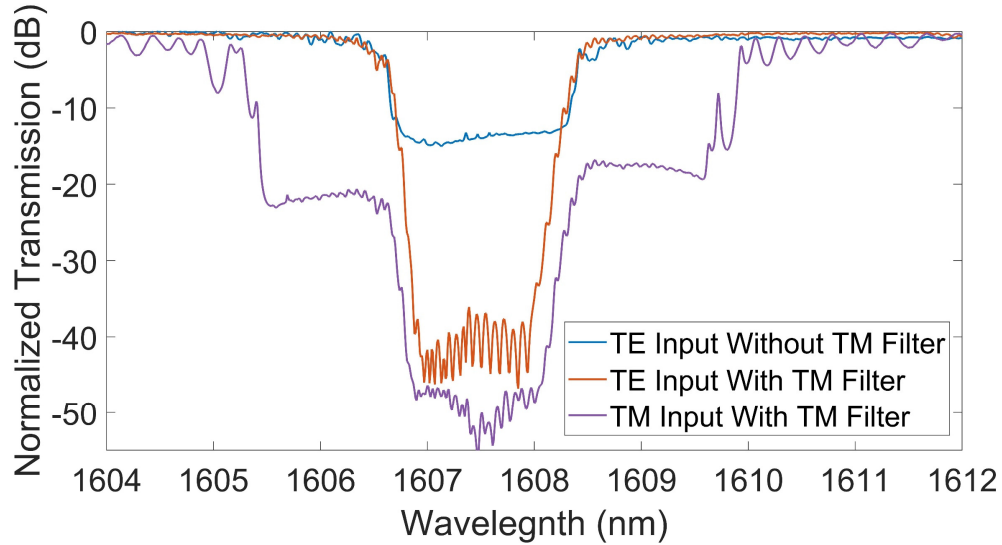


Figure 5-6 Transmission pattern of TE Bragg grating without TM noise filter and transmission pattern of TE Bragg grating with TM noise filter. The TE and TM stopbands overlap so that the TM noise inside the TE stopband is suppressed by around 30 dB.

The experimental FWM measurement result is shown in Fig. 5-7. With the FWM Bragg grating, we observe five resonant peaks inside the stopband with the narrowest peak having a 3-dB linewidth of 3.3 pm (388MHz). This corresponds to a quality factor of 470k. The pump and signal wavelengths are offset by one free spectral range (FSR) near 1587 nm. As shown in Fig. 5-7 (c), the resonance enables more than 100 times intensity enhancement on all three resonant wavelengths. The FSR of the resonant peaks are measured to be around 1.39 nm (165.97 GHz). A -29 MHz FSR

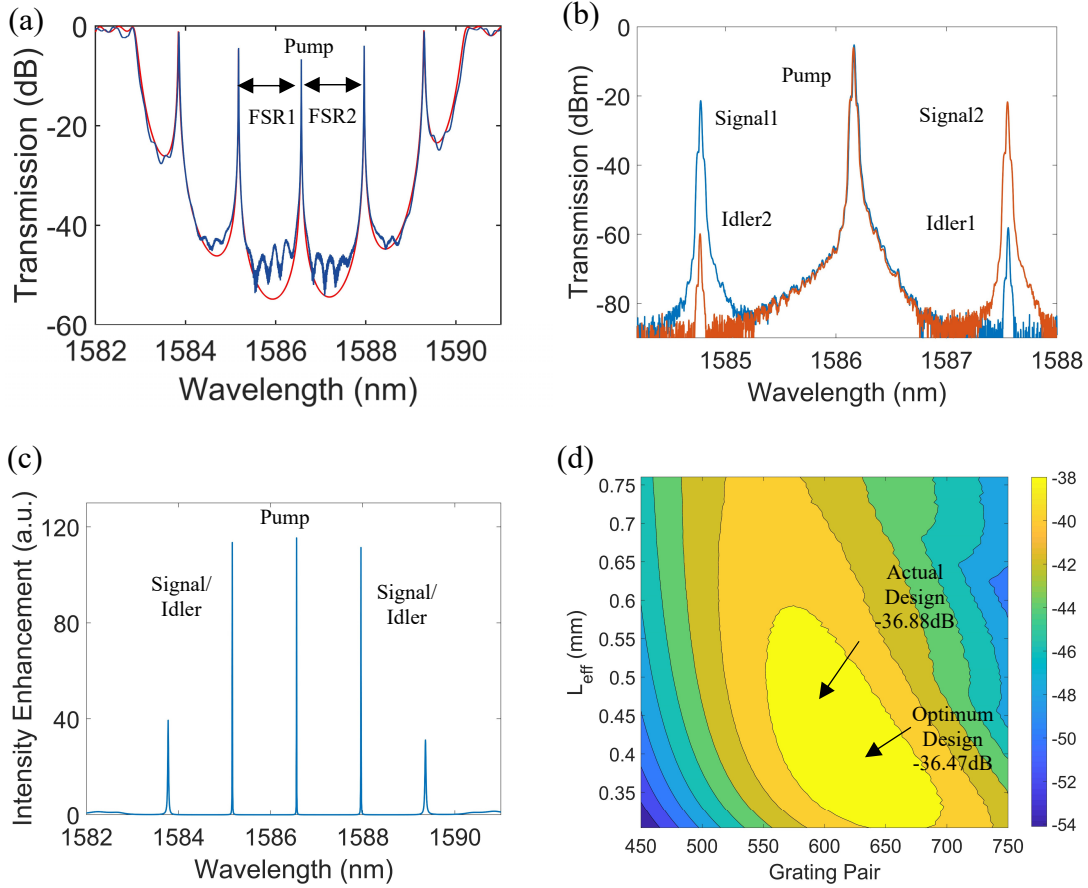


Figure 5-7 (a) Transmission of the FWM Bragg grating. The 3-dB linewidth of the resonant peak is measured to be 3.3pm, corresponding to a quality factor of 480k. (b) The calculated IE factor inside the stopband. (c) The measured FWM signals. A -37.7 dB conversion efficiency is experimentally observed. (d) Simulation of the FWM conversion efficiency. The theoretical conversion efficiency of the actual device is slightly less than that of the optimum design due to fabrication uncertainty.

detuning, defined as  $FSR1 - FSR2$ , is measured as shown in Fig. 5-7(a). With an incident pump power of 5.3 dBm and a signal power of -11.9 dBm, we observed an FWM conversion efficiency of -37.7 dB. From Equation 5-8, the calculated FWM efficiency

should be -36.47 dB. As shown in Fig. 5-7 (d), the calculated FWM efficiency of the optimum design should be -36.47 dB from Equation 5-8. The actual fabricated device slightly deviates from the optimum design due to fabrication uncertainty. For the estimated experimental parameters, the maximum theoretical efficiency is calculated to be -36.88dB, which is in reasonably good agreement with our experimental result and thus support the validity of our theory.

Dispersion is a critical factor in FWM since the FWM process is optimum when both energy conservation and momentum conservation are both satisfied. A mismatch between the converted frequency and the resonant frequency of the cavity will limit the FWM efficiency. In most ring resonator based nonlinear applications, a zero or anomalous dispersion within a certain frequency range is favorable and is usually realized by carefully designing a thick Si<sub>3</sub>N<sub>4</sub> core, typically more than 600 nm. Such thick LPCVD Si<sub>3</sub>N<sub>4</sub> requires additional stress release process including annealing, multi-layer deposition [66,67] or the use of a photonic damascene process [68]. These methods increase the fabrication complexity, and some are not compatible with a CMOS process. However, in a FPBG-FWM platform, the grating induced dispersion can be a powerful tool to counteract the waveguide induced dispersion without requiring thick Si<sub>3</sub>N<sub>4</sub> deposition and dispersion engineering. As shown in Figure 5-8 (a-b), the grating induced dispersion is not only way larger than the waveguide dispersion, which is around -1400 ps/(nm·km), but also nonuniform and symmetrical with respect to the stopband center. An extremely strong, nonuniform and symmetrical grating dispersion indicates that, even if a conventional dispersion engineering

approach is implemented, the resonances of the FPBG cavity will still not be equally distant unless the resonances, whose position are determined by the combination of grating phase and cavity phase, are symmetrical within the stopband. While the grating dispersion is an additional dispersion mechanism compared with a ring resonator, it provides a new tool to offset the waveguide dispersion without having to adjust the waveguide geometry. One can always locate three resonances where the grating dispersion can fully compensate the waveguide dispersion such that the phase matching condition is satisfied and the FWM efficiency is maximized. Taking waveguide dispersion into account, such three equal distant resonances are quasi-symmetrical with respect to the stopband center. Such mechanism does not rely on the waveguide geometry and can be adjusted with careful tuning of the cavity phase. The FSR of the resonances in a FPBG cavity is determined by,

$$\phi_m + \frac{2Ln\pi\nu_m}{c} = m\pi \quad (5 - 14)$$

$$\phi_{m+1} + \frac{2Ln\pi\nu_{m+1}}{c} = (m + 1)\pi \quad (5 - 15)$$

$$\nu_{FSR} = \nu_m - \nu_{m+1} \quad (5 - 16)$$

where  $m$  is the order of resonance,  $\phi_m, \phi_{m+1}$  are the phases generated from a single Bragg grating reflection at the wavelength of the  $m$  and  $m+1$  order, respectively,  $\nu_m, \nu_{m+1}$  are the resonant frequency of the  $m$  and  $m+1$  order, respectively, and  $L$  is the cavity length. Thus, by tuning the cavity phase ( $n$ , or  $L$ ), the resonances will drift across the stopband, and it is possible to controllably move the three resonances to the equal

distant position and thus realize the phase matching condition, i.e., zero FSR detuning ( $FSR_1 = FSR_2$ ).

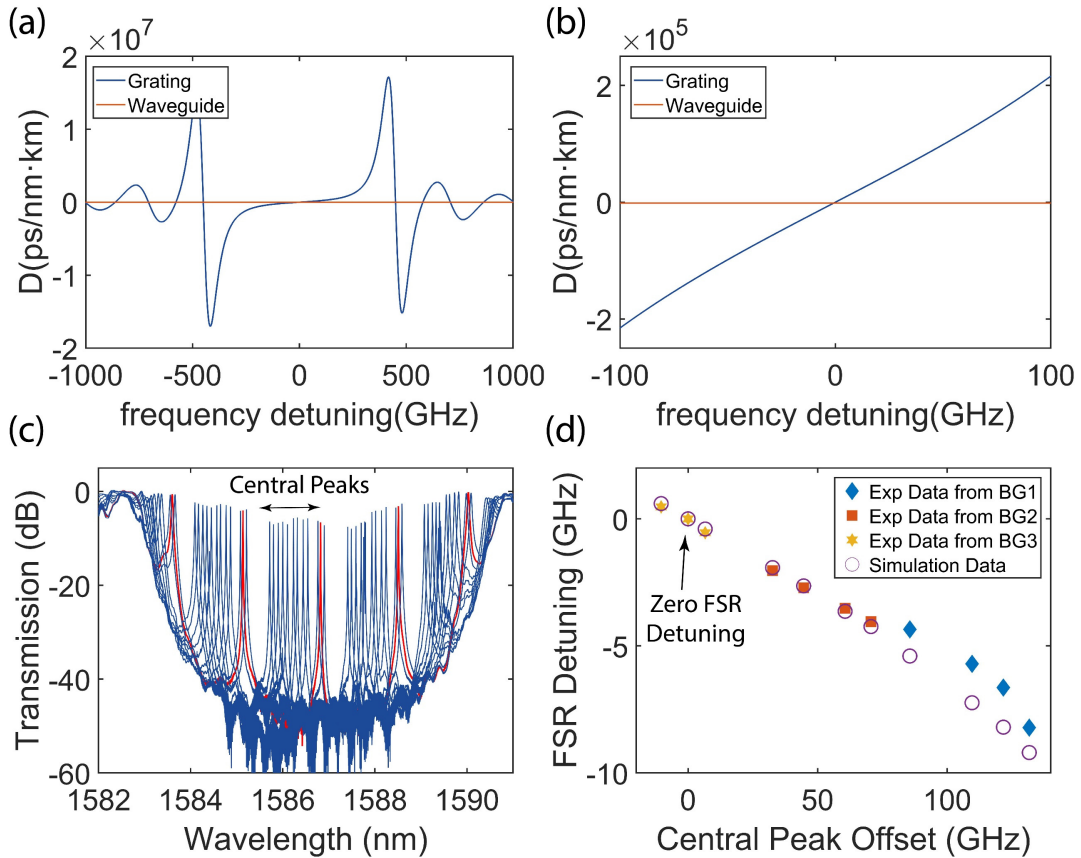


Figure 5-8 (a) Comparison of grating induced dispersion and waveguide induced dispersion. The grating dispersion is dominant compared to the waveguide dispersion (b) A zoom-in dispersion comparison shows that the grating dispersion is still dominant around the stopband center. (c) The experimental results of thermal-tuning based dispersion engineering. Resonant peaks drift inside the stopband while leaving the stopband position unchanged. The red line represents the -5.6 MHz FSR detuning position. (d) the FSR detuning changes with the central peak frequency offset showing that thermal tuning can effectively implement dispersion compensation. Experimental

results are in good agreement with the transfer matrix simulation results. The simulation results indicate that zero FSR detuning is achievable. [69]

Here, we have integrated nickel-chromium heaters on the chip to tune the cavity phase. To avoid thermal diffusion that will heat up the grating, the heater is designed to be small compared to the cavity. A single tiny heater, however, cannot provide enough thermal tuning range because it can only sustain limited heating powers. We experimentally designed three FPBGs whose cavity lengths have  $1/3$  grating period  $\Lambda$  difference between each other so that the three FPBGs together can sweep across the stopband and thus realize the phase matching condition. Figure 5-8 (c) shows that, by applying power on the heaters, the resonant peaks drifts inside the stopband while leaving the stopband position unchanged. As shown in Figure 5-8 (d), experimentally, the FSR detuning of the central three peaks are tuned from -8.22 GHz to +0.55 GHz and is dependent on the central peak offset, namely the offset from the position of the central peak corresponding to zero FSR detuning. The larger the central peak detuning, the larger the FSR detuning will be. Although the best FSR detuning we got is -5.6 MHz, corresponding to the red line as shown in Figure 5-8 (c), phase matching condition is achievable with better temperature control over the integrated heater since we have successfully tuned the FSR detuning from negative to positive. By simulating the transmission spectrum of the FPBG with different cavity lengths through the transfer matrix method, we calculate the relationship of the FSR detuning and the central peak frequency detuning and it shows good agreement with the experimental results despite some discrepancy between the experimental data of Bragg grating 1

(BG1) and the simulation results due to fabrication imperfection. This experimental result is remarkable since the simulated dispersion parameter of our current waveguide geometry is around  $-1400 \text{ ps}/(\text{nm}\cdot\text{km})$ , which is in a highly normal dispersion region. It corresponds to an inherent FSR detuning of  $-100 \text{ MHz}$  for a  $1.39 \text{ nm}$  FSR. We successfully compensated it by controllably leveraging the huge grating dispersion. It is worth noting that, while the FSR detuning coming from the waveguide inherent dispersion is comparable to the linewidth of the resonance, it will be substantial if the  $Q$  of the cavity is improved to several millions. Without the thermal tuning phase matching strategy, it would be impossible to achieve efficient wavelength conversion. Thus, such thermal tuning strategy in fact paves the way for future FPBG-FWM applications for ultra-high- $Q$  FPBG.

## **5.5 Conclusion and Proposed Future Work**

In this work, we have studied the FPBG-FWM process in  $\text{Si}_3\text{N}_4/\text{SiO}_2$  on Si platform, from theory development, grating optimization to experimental demonstrations near  $1590 \text{ nm}$ . A  $-37.7 \text{ dB}$  FWM conversion efficiency is observed with a  $5.3 \text{ dBm}$  on chip pump power. We demonstrate that by using a tapered grating the grating loss can be largely reduced from  $3.5 \text{ dB/cm}$  to  $0.36 \text{ dB/cm}$ , which makes the high efficiency FWM process possible. We also demonstrate that, by thermally tuning the phase of the Fabry-Pérot cavity, the phase matching condition can be realized on a relatively thin  $\text{Si}_3\text{N}_4$  film after compensating the waveguide inherent dispersion. This phase matching technique removes the need for thick  $\text{Si}_3\text{N}_4$  deposition, which is one of the major fabrication challenges for micro-ring cavity based FWM process. It is worth

noting that, the phase matching strategy demonstrated in this work can be extended to the cases where more resonances are involved in the FPBG cavity. By adjusting the FPBG design, more resonances can exist in the stopband. Following the phase matching strategy demonstrated here, the phase matching condition can be satisfied in multiple symmetrical resonances (e.g. satisfied for resonances  $(-1, 0, 1)$ ,  $(-2, 0, 2)$  but not for  $(-2, -1, 0)$ ), due to the nonuniform but symmetrical grating dispersion. This can be advantageous for multiplexed entangled photon pairs generation when spontaneous FWM is available since the photon pairs can only be generated on the symmetric resonances in the stopband, rather than spread out until phase matching condition is no longer satisfied, as shown in multiplexed entangled photon pairs generated by ring resonator [70,71]. In the FPBG case, the power of the generated signals and the photon rates in every channel will be more uniform. Thus, such a uniform signal intensity over a given bandwidth can be preferable for applications in quantum communications. Above all, the FPBG platform is shown to be a promising approach to realize high efficiency FWM and potentially spontaneous FWM (SFWM). While the SFWM is not observable since the noise level of our OSA is higher than the SFWM level, given that the FWM efficiency is quadratically proportional to the pump power and depends on losses, we are optimistic that efficient SFWM would be achievable in future experiments with our grating approach when the losses can be further minimized, and the pump power is higher. We envision that the FPBG-FWM will be used in many interesting applications such as controllable photon pairs generation and quantum communication.

## Chapter 6 : On-Chip High Q Ring Resonator

### 6.1 Introduction

As we discussed in Chapter 5, further reducing the losses of grating and cavity, and increasing the nonlinearity, would greatly improve the nonlinear conversion efficiency of the FWM process, and thus make SFWM process possible. There are different approaches to achieve these goals. First, there has been extensive research [67,72–74] on on-chip ring resonators which use thicker silicon nitride ( $\text{Si}_3\text{N}_4$ ) films. With a thicker  $\text{Si}_3\text{N}_4$  film and a carefully designed waveguide supporting multiple guided modes, the fundamental mode of the given waveguide geometry will be strongly confined in the waveguide so that the mode will experience less boundary roughness, and as a result, a lower loss. In addition, from Equation 5-13, a more confined mode will decrease the effective area and increase the filling factor, contributing to a higher nonlinearity even if the material remains the same. However, a major challenge for the thick  $\text{Si}_3\text{N}_4$  film is that LPCVD grown  $\text{Si}_3\text{N}_4$  has high internal stress, which requires extra efforts to grow a thick  $\text{Si}_3\text{N}_4$  film without cracks due to the stress. Secondly, different materials with high nonlinearity, low loss, and a broad transparency window are emerging, such as lithium niobate ( $\text{LiNbO}_3$ ) [50,51], aluminum nitride (AlN) [75–77], etc. Particularly, AlN has been shown as a promising platform for astrophotonics and nonlinear optics application because it has a large transparent window (205nm – 7.5 $\mu\text{m}$ ) [78], high second order nonlinearity ( $d_{33} = 1 -$

$3 \times 10^{-23} \text{C/V}^2$ ) [79] , and low loss. Recently a loss of 0.13-0.14dB/cm has been reported [76,77] by researchers.

In the following sections of Chapter 6, we will investigate and optimize the losses of a waveguide on thicker  $\text{Si}_3\text{N}_4$  film and AlN film. Without loss of generality, we use ring resonators to characterize the losses since the design of ring resonators is less complicated than FPBG, as demonstrated in Chapter 5. Theoretically, the loss characterized with the ring resonator should be the same as measured by the FPBG approach. Thus, we may directly employ all the techniques that minimize the loss of ring resonators waveguide to future FPBG cavity. We will first introduce the theory of ring resonators. We will then discuss our work on ring resonators with 600nm  $\text{Si}_3\text{N}_4$ -on- $\text{SiO}_2$  platform and with AlN-on-sapphire platform. We demonstrate that, with a ring resonator on 600nm  $\text{Si}_3\text{N}_4$  film, the loss can be reduced from 0.33dB/cm, as shown in Chapter 4, to 0.18dB/cm, corresponding to a loaded Q of 1.81 million and an intrinsic Q of 1.86 million; with a ring resonator on 400nm AlN-on-sapphire platform, the measured loaded Q is 141000, corresponding to a loss of 1.95 dB/cm. All these results pave the way for future on-chip nonlinear optics applications.

## **6.2 Theory of Ring Resonator**

Figure 6-1 shows the schematics of a ring resonator. Usually, a ring resonator comprises of one bus waveguide and a ring resonator. The coupler allows the possibility of energy exchange between the bus waveguide and the ring resonator at the location of the coupler. At the coupler, while most of the light  $t$  will propagate along the bus waveguide, depending on the coupling strength  $\kappa$ , a fraction of the input light

will be coupled into the ring. Then the light coupled into the ring will circulate along the ring, while another fraction of the light will be coupled out of the ring when the light passes the coupler.

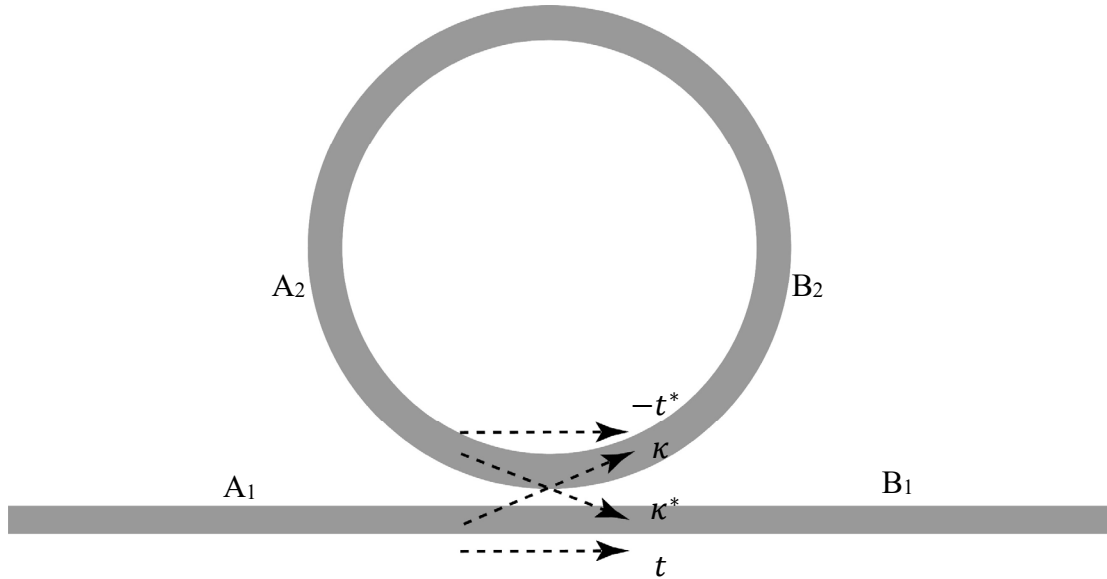


Figure 6-1 Schematics of the ring resonator

Now, we investigate the coupling between the bus waveguide and the ring in detail [80,81]. Let  $A_1$  and  $A_2$  be the mode amplitudes of the input light at the bus waveguide and the ring,  $B_1$  and  $B_2$  be the mode amplitudes of the output light at the bus waveguide and at the ring, respectively. The input-output relationship can be described as

$$\begin{bmatrix} B_1 \\ B_2 \end{bmatrix} = \begin{bmatrix} t & \kappa^* \\ \kappa & -t^* \end{bmatrix} \begin{bmatrix} A_1 \\ A_2 \end{bmatrix} \quad (6 - 1)$$

where  $t$  is the bus-bus coupling coefficient, and  $\kappa$  is the bus-ring or ring-bus coupling coefficient. Due to the unitary property, the coupling coefficients  $t$  and  $\kappa$  satisfy the following relationship:

$$|t|^2 + |\kappa|^2 = 1 \quad (6 - 2)$$

We can also relate  $A_2$  and  $B_2$  with  $A_2 = B_2 a e^{i\theta}$ , where  $\theta$  is the round-trip phase shift and  $a = e^{-\alpha\pi R}$  represents the remaining mode amplitude after a round trip in the ring in the presence of the loss coefficient  $\alpha$ . Here a factor of two is canceled because the  $a$  represents the mode amplitude instead of the intensity.

After solving the above equations, we can find that the transmission in the bus waveguide is governed by:

$$T = \left| \frac{B_1}{A_1} \right|^2 = \frac{a^2 + t^2 - 2at\cos\theta}{1 + a^2t^2 - 2at\cos\theta} \quad (6 - 3)$$

From Equation 6-3, we can calculate the transmission spectrum. A sample transmission of a ring resonator is shown in Fig. 6-2. The linewidth or loaded quality factor  $Q_L$ , of the resonance is related to the losses of the ring resonator and the coupling condition. Besides  $Q_L$ , there are two additional quantities, the intrinsic quality factor  $Q_i$  and the coupling quality factor  $Q_c$  describing the losses due to the intrinsic loss of the ring waveguide and the power dissipation at the ring-bus coupler, respectively. The  $Q_L$ ,  $Q_i$ , and  $Q_c$  are related by:

$$\frac{1}{Q_L} = \frac{1}{Q_i} + \frac{1}{Q_c} \quad (6 - 4)$$

$$Q_i = \frac{2\pi n_g}{\alpha\lambda_0} \quad (6 - 5)$$

where  $n_g$  is the group index of the ring waveguide, and  $\alpha$  is the loss coefficient of the ring waveguide. Thus, by fitting the transmission and linewidth, we can extract the loss coefficient of the ring waveguide.

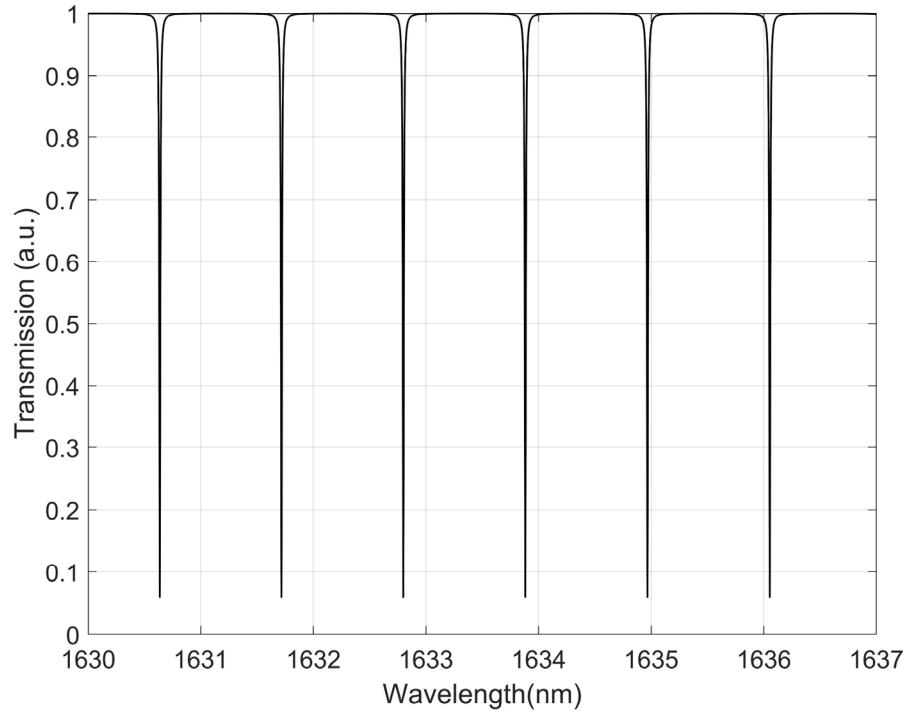


Figure 6-2 Sample transmission of a ring resonator

It is worth noting that, there are different designs for the ring-bus coupler in addition to the straight coupler shown in Fig. 6-1. One of the most widely used design is the Pulley coupler [77], in which the bus waveguide is a bend waveguide that is concentric with the ring. Since the Pulley coupler can effectively increase the coupling length, it is very useful for loosening the fabrication requirement by allowing a wider ring-bus gap for given coupling strength  $\kappa$ , when the modes in both the ring and the

bus waveguide are too confined. Other types of coupler, such as a symmetric coupler or a weakly tapered gap coupler has also been demonstrated by other researchers [82], but a detailed description is beyond the scope of this dissertation.

A ring resonator has three different coupling conditions. When  $a = t$  and  $\cos\theta = 0$ , the transmission  $T = 0$ , which is known as the “critical coupling” condition. When  $a < t$ , in which case the power in the ring resonator is mainly dissipated through the propagation loss of the ring waveguide, it is known as the “under coupled” condition. When  $a > t$ , in which case the power in the ring resonator is mainly dissipated through the ring-bus coupling, it is known as the “over coupled” condition [83]. It is worth noting that, with the same losses in the ring, one can get a higher  $Q_L$  when the ring resonator is in the under coupled condition than when the ring resonator is in the over coupling condition. In addition to the method described by Equation 6-3, 6-4 and 6-5, an alternative way to relate the  $Q_L$  and  $Q_i$  is [84]

$$Q_i = \frac{2Q_L}{1 \pm \sqrt{T}} \quad (6 - 7)$$

where “+” corresponds to the under coupled condition and “-” corresponds to the over coupled condition. Obviously, for a given  $Q_i$ , the  $Q_L$  is higher when the ring resonator is in the under coupled condition. Thus, researchers usually design the ring resonator in the under coupled condition so to achieve a higher  $Q_L$  and realize other nonlinear optics applications such as optical comb generation and soliton generation.

### 6.3 Ring Resonator Based on 600nm Si<sub>3</sub>N<sub>4</sub> Film

The first step to characterize the ring resonator performance on 600nm Si<sub>3</sub>N<sub>4</sub> film is to deposit such film on a silicon wafer. A low loss, crack-free Si<sub>3</sub>N<sub>4</sub> film is essential for low loss photonics applications. Plasma-enhanced chemical vapor deposition (PECVD) and low-pressure chemical vapor deposition (LPCVD) are two methods to deposit Si<sub>3</sub>N<sub>4</sub> film in the standard CMOS process. While PECVD can easily deposit several microns Si<sub>3</sub>N<sub>4</sub> film, due to the N-H bond generated in PECVD deposition process, an absorption peak exists at 1.5  $\mu\text{m}$ , which will significantly degrade the device performance at the communication band [3,4]. LPCVD, instead, can get rid of the N-H bond absorption problem. Hence, it is an ideal solution to get low loss Si<sub>3</sub>N<sub>4</sub> film. However, a significant disadvantage of LPCVD deposited Si<sub>3</sub>N<sub>4</sub> film is the high intrinsic film stress [67]. The film stress can easily build up as the thickness of LPCVD deposited Si<sub>3</sub>N<sub>4</sub> grows. As shown in Fig 6-3, without proper treatment, the film can easily crack during the following fabrication processes due to minor mechanical shocks. The crack due to film stress usually originates from the wafer's edge and will propagate across the wafer, making the whole wafer full of cracks. In our experiments, when the film is as thick as 600nm, it may crack immediately after the LPCVD deposition, making the photonics application based on such thick Si<sub>3</sub>N<sub>4</sub> film impossible.

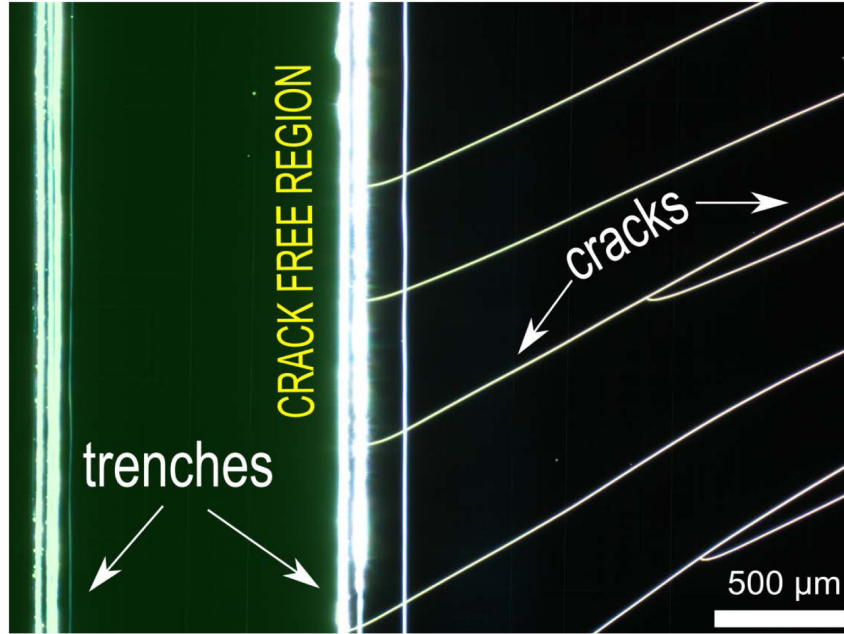


Figure 6-3 Crack of LPCVD Si<sub>3</sub>N<sub>4</sub> due to internal stress of the film. A Trench can stop the propagation of the crack. [67]

Researchers have shown solutions to this problem. Luke *et al.* [67] demonstrated that, by placing several trenches to isolate the region with photonics devices from propagating cracks, the area surrounded the trenches can be crack-free. However, such a strategy does not work in our case. Since we are using e-beam lithography (EBL) to define the photonics device patterns, it is impossible to use EBL for wafer-scale processing. Thus, a wafer dicing is necessary after the LPCVD deposition to yield individual chips with suitable sizes for the subsequential processing. While the trenches can stop the cracks originating from the edge from propagating across the wafer after the LPCVD deposition, the dicing process will introduce a set of new cracks along the dicing path, which leaves the trenches completely useless. To

avoid this problem, we change the fabrication process from deposition-then-dice to dice-then-deposition to bypass the mechanical shock due to dicing. Typically, the LPCVD deposition is done in vertical mode to ensure the uniformity of the film as shown in Fig 6-4 (a). Here, we first dice the wafer into  $2 \times 1.5\text{cm}^2$  chips, and deposit it in horizontal mode, as shown in Fig 6-4 (b). To reduce the intrinsic film stress, the deposition process is done in two 300nm deposition steps. With this process, we yield 600nm crack-free  $\text{Si}_3\text{N}_4$  film with a nonuniformity of better than  $\pm 0.2$  nm, which paved the way for ring resonator research based on a 600nm thick  $\text{Si}_3\text{N}_4$  film.

The next step is to design the ring resonator. We first define the geometry of the ring resonator and the bus waveguide. When the ring resonator supports multiple guided modes, the fundamental mode will be more confined, thus suffers from less scattering losses due to the sidewall roughness, corresponding to a higher Q. Compared with the higher order modes, the fundamental mode always shows the lowest propagation loss due to less overlap with the waveguide boundary. However, if the ring resonator supports too many guided modes, the ring-bus coupling can be more complicated and multiple sets of resonances originating from different orders of guided mode will be observed. Hence, the geometry of the ring resonator is designed to be  $2\ \mu\text{m} \times 0.6\ \mu\text{m}$ , supporting three guided TE modes, and the geometry of bus waveguide is designed to be  $0.8\ \mu\text{m} \times 0.6\ \mu\text{m}$ , supporting one guided TE mode, respectively, as shown in Fig. 6-5. Comparing Fig 6-5 (a) with Fig. 6-5 (c), the fundamental mode in the wider waveguide has less overlap with the waveguide sidewall.

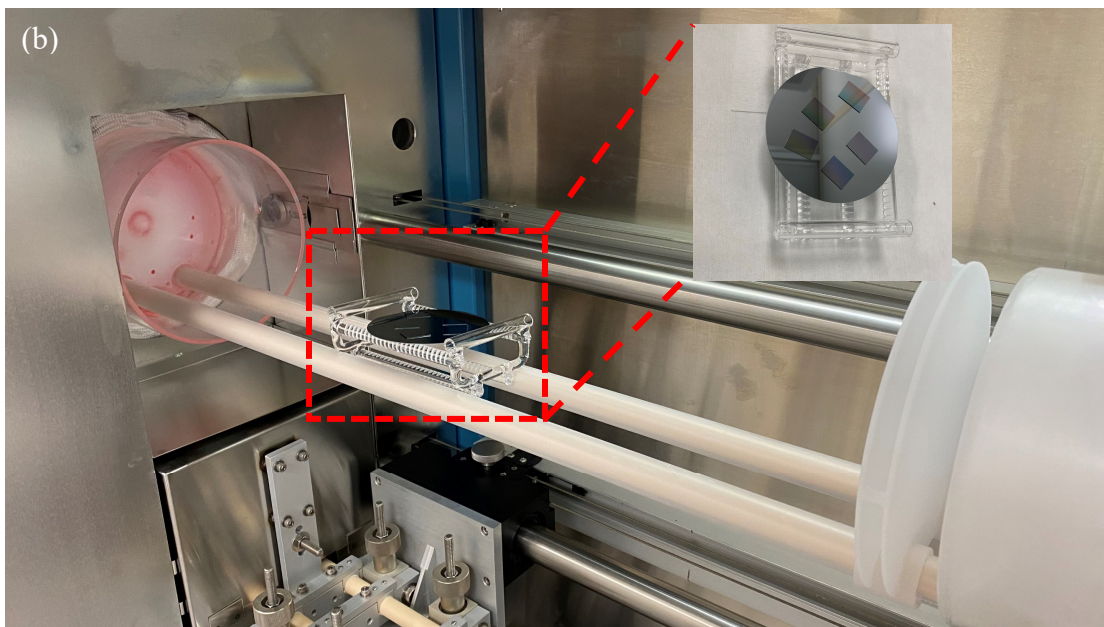
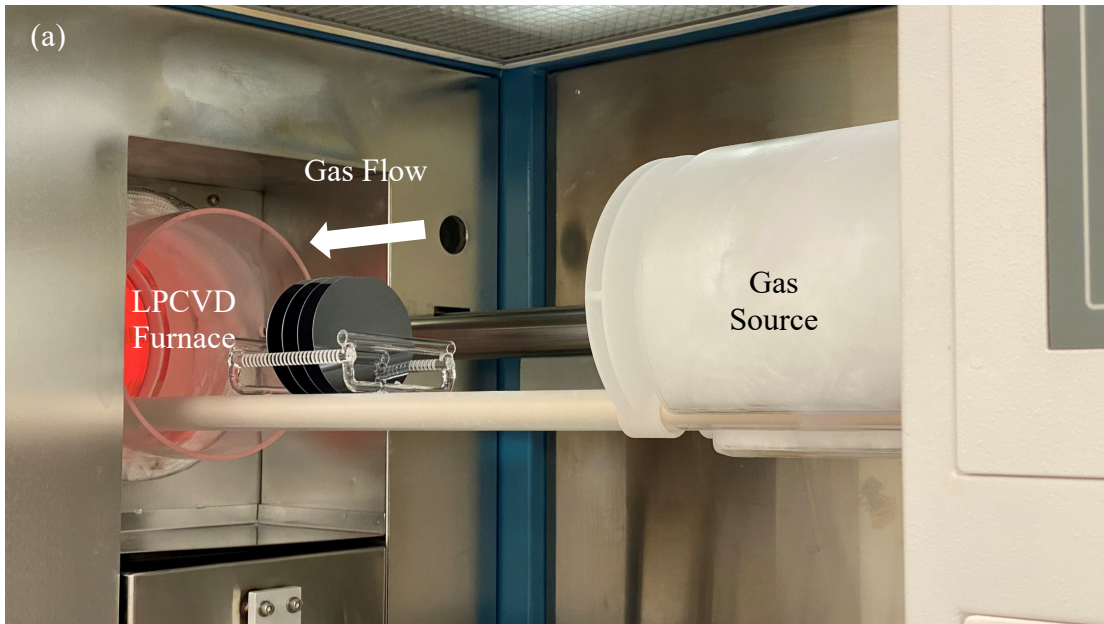


Figure 6-4 Setup of LPCVD deposition. (a) Vertical mode (b) Horizontal mode. The inset shows how the individual chips are placed on the carrier wafer.

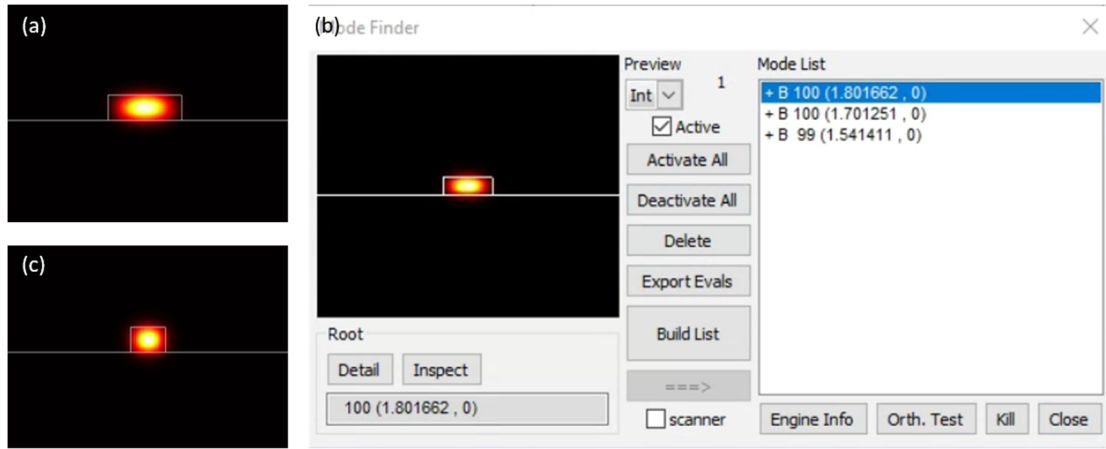


Figure 6-5 Mode profile of the ring and bus waveguide. (a-b) Mode profile of the  $2\ \mu\text{m} \times 0.6\ \mu\text{m}$  ring waveguide. The waveguide geometry supports three guided TE mode. (c) Mode profile of the  $0.8\ \mu\text{m} \times 0.6\ \mu\text{m}$  bus waveguide.

Then, the ring-bus gap and the radius of the ring resonator are designed. The bending loss of the ring resonator must be negligible so that the extracted intrinsic Q can reflect the loss purely due to scattering loss and material absorption. Fig. 6-6 shows the FIMMPROP simulated mode profile when a  $\text{TE}_0$  mode is injected from the input port of the bus waveguide to the ring resonator and the scattering matrix associated with the given ring resonator design. As shown in Fig 6-6 (b), the  $\text{TE}_0$  mode in the bus waveguide is mainly coupled to the  $\text{TE}_1$  mode of the ring resonator. Here we find that for the  $2\ \mu\text{m} \times 0.6\ \mu\text{m}$  waveguide with  $200\ \mu\text{m}$  bending radius, the  $\text{TE}_0$ - $\text{TE}_0$  coupling strength  $\kappa$  with a ring-bus gap of  $500\text{nm}$  is simulated to be  $0.0116$  at  $1630\text{nm}$ , corresponding to  $t = 0.9999$ . To achieve a critical coupled or under coupled condition, the minimum loss of the ring resonator should be  $>0.01\text{dB/cm}$  with the given  $t$ . We expect the loss of the waveguide on  $600\ \text{nm}\ \text{Si}_3\text{N}_4$  film is lower than on  $300\ \text{nm}\ \text{Si}_3\text{N}_4$

film. Without knowing the loss of the ring resonator, we design the ring-bus gap to be 500nm, 600nm, and 700nm for both ring resonator designs. With ring resonators having different gaps, we can better identify the coupling condition of the ring resonator and extract the loss.

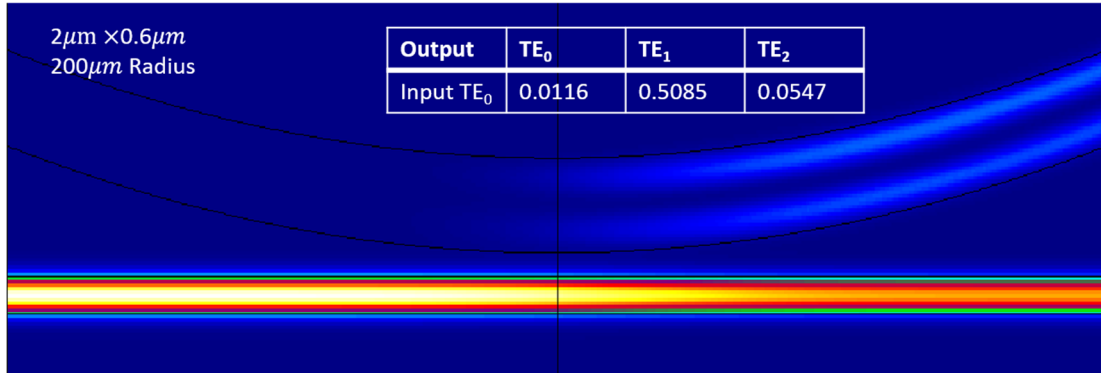


Figure 6-6 Simulated mode profile of the ring-bus coupler.

To improve the etch quality and get rid of the sidewall redeposition problem [72], we used CHF<sub>3</sub>/O<sub>2</sub> chemistry for the Si<sub>3</sub>N<sub>4</sub> etching. Also, since any ultrasonic process, such as liftoff, is strictly prohibited to keep the chip crack-free, we used negative resist, maN-2405, instead of positive resist ZEP-520A, for the 600nm Si<sub>3</sub>N<sub>4</sub> chip. After following the fabrication processes as described in Chapter 2, we successfully fabricated the device without crack, as shown in Fig. 6-7.

The experimental result for the ring resonator with a waveguide geometry of  $2 \mu m \times 0.6 \mu m$  is shown in Fig 6-8. Fig 6-8 (a) shows the overall transmission spectrum of the ring resonator from 1450 nm to 1640 nm with a gap of  $500 \mu m$ . Theoretically, the propagation loss should be lower at 1640 nm since the mode is less confined at longer wavelength, and it is far from the N-H absorption at 1505nm due to

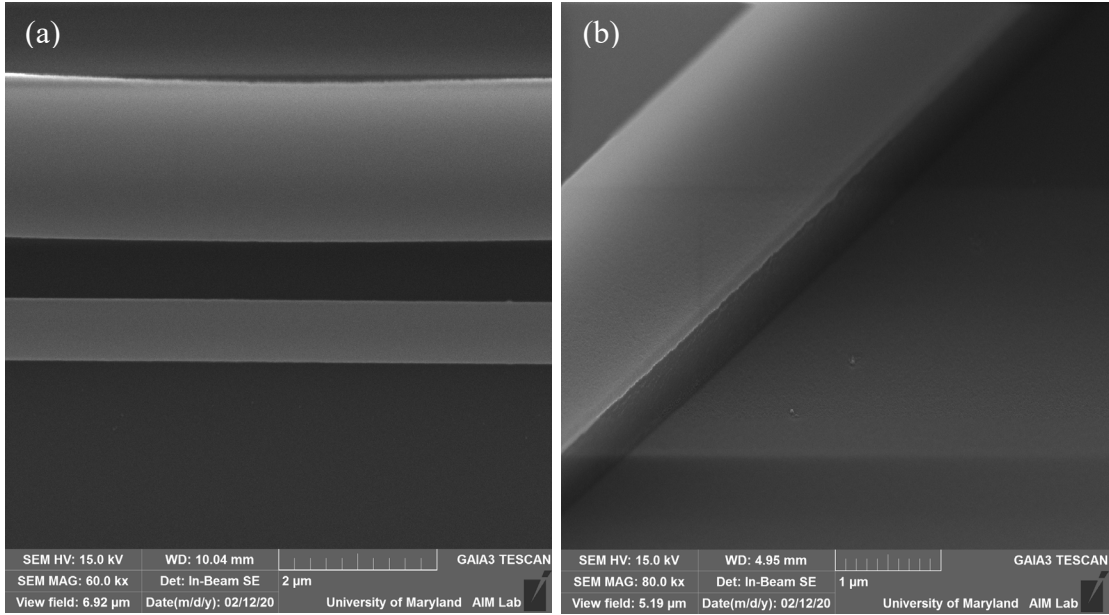


Figure 6-7 SEM images of the ring resonator. (a) ring-bus coupling region. (b) tilted view of the ring resonator, a smooth sidewall is achieved with the  $\text{CHF}_3/\text{O}_2$  ICP-RIE etch.

silane PECVD deposited  $\text{SiO}_2$ . Fig 6-8 (b) shows the detailed transmission at wavelength between 1630 nm to 1639 nm with different ring-bus gaps. There are three sets of resonances in the ring resonator with  $0.5 \mu\text{m}$  gap and only two sets of resonances in the ring resonator with  $0.6 \mu\text{m}$  and  $0.7 \mu\text{m}$  gaps. All the resonances show a FSR of  $\sim 1.03 \text{ nm}$  because the group index difference between different modes is negligible. Since the  $\text{TE}_0\text{-TE}_0$  coupling is the weakest ring-bus coupling pair according to the simulation, and we expect that the  $\text{TE}_0$  mode in the ring resonator has the lowest loss, we identify that the shallowest and narrowest resonances in the  $0.5 \mu\text{m}$  gap result originate from the  $\text{TE}_0\text{-TE}_0$  coupling in the under coupled condition. We do not observe the  $\text{TE}_0\text{-TE}_0$  resonances in the ring resonator with  $0.6 \mu\text{m}$  or  $0.7 \mu\text{m}$  gap because the

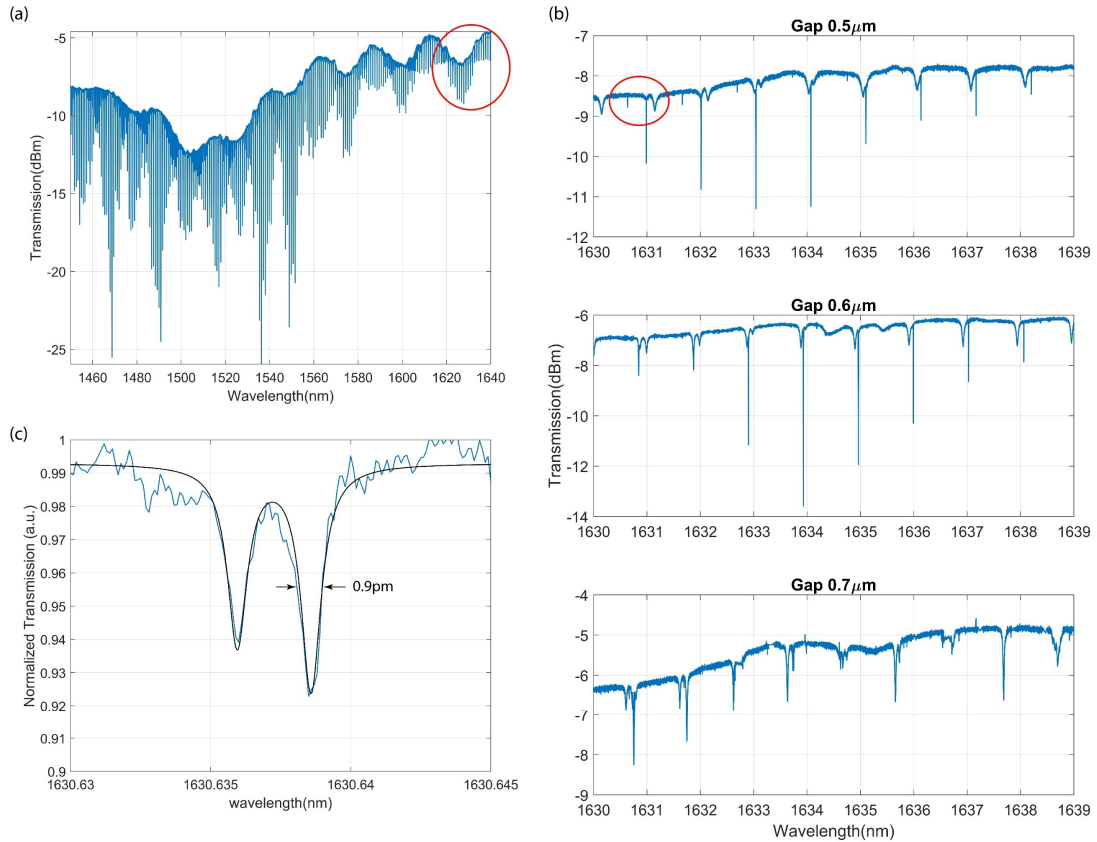


Figure 6-8 Experimental result of the ring resonator with geometry of  $2 \times 0.6 \mu\text{m}$  and  $200 \mu\text{m}$  radius. (a) Overall transmission of the ring resonator from 1450 nm to 1640 nm. (b) Transmission of three ring resonators with different ring-bus gaps at 1630-1639nm. Three sets of resonances are observed in the ring resonator with  $0.5 \mu\text{m}$  gap while only two sets of resonances are observed in the ring resonator with  $0.6 \mu\text{m}$  and  $0.7 \mu\text{m}$  gap. (c) Zoomed in transmission of the red circle in (b), resonance split is observed due to the coupling between clockwise (CW) and counter-clockwise (CCW) propagating light, because of imperfect waveguide sidewall. Blue line: experimental results, Black line: Fitting results.

ring-bus coupling is too weak so that the TE<sub>0</sub>-TE<sub>0</sub> resonances are not visible according to Equation 6-3. We further investigate the resonances from TE<sub>0</sub>-TE<sub>0</sub> coupling to extract the Q and losses of the ring resonator. Fig 6-8 (c) shows that the full width half maximum (FWHM) linewidth of the resonance is 0.9 pm, corresponding to a loaded Q of 1.81 million. With Equation 6-7, we can conveniently extract the  $Q_i$  to be 1.86 million, corresponding to a propagation loss of 0.18 dB/cm. We fit the experimental results with Equation 6-3 and extracted that the coupling strength  $\kappa$  is 0.0138, which agrees reasonably well with the simulation results, confirming the accuracy of the theory and the simulation results. As shown in Fig 6-8 (c), resonance splitting, coming from the light backscattering due to sidewall imperfection in the ring resonator, is observed. Such resonance splitting effect can only be observed when the loss is very low. [85]

#### **6.4 Ring Resonator Based on AlN**

AlN-on-sapphire has been demonstrated as an emerging platform for integrated photonics devices due to its low loss, and ultra-broad transparency window. Especially, AlN has one of the largest bandgaps in photonics materials ( $\sim 6.2\text{eV}$ ), which enables application from ultraviolet to mid-infrared range [78]. This is especially attractive for astrophotonics and quantum information applications. In addition, compared to Si<sub>3</sub>N<sub>4</sub>, which only has a third-order nonlinearity ( $\chi^{(3)}$ ), AlN has both second-order ( $\chi^{(2)}$ ) and third-order nonlinearities due to its non-centrosymmetric crystal structure. Hence, it has also been used for second harmonic generation and electro-optic devices.

There are different techniques to grow AlN on sapphire, such as molecular beam epitaxy (MBE), metal organic chemical vapor deposition (MOCVD), sputtering [75], and physical vapor deposition (PVD). In this work, we use commercially available AlN-on-sapphire wafers from Kyma Technologies, Inc. The AlN is deposited by PVD with nanocolumns (PVDNC). Compared to MBE and MOCVD AlN, PVDNC AlN has lower costs and better scalability. In this section, we investigate the AlN waveguide loss with an AlN thickness of 400nm.

It is worth noting that, while the refractive index of AlN is close to Si<sub>3</sub>N<sub>4</sub> (~2.1 at 1550 nm), the refractive index of sapphire (~1.75 at 1550nm) is higher than that of SiO<sub>2</sub>. Thus, the AlN-on-sapphire waveguide mode is less confined than the Si<sub>3</sub>N<sub>4</sub> waveguide with the same waveguide geometry. In this work, we design the bus waveguide to be  $1.6\mu\text{m} \times 0.4\mu\text{m}$ , supporting one guided TE mode, and the ring to be  $2.6\mu\text{m} \times 0.4\mu\text{m}$ , supporting two guided TE modes, as shown in Fig. 6-9 (a-b). We also simulated the bending loss of the ring waveguide. As shown in Fig. 6-9 (c), the bending loss decreases rapidly when the bending radius increases and is negligible when the bending radius is larger than  $150\mu\text{m}$ . Here, we design the bending radius to be  $250\mu\text{m}$ . Fig 6-9 (d) shows the mode profile of the ring waveguide with  $250\mu\text{m}$  bending radius. Compared to Fig. 6-9 (b), the mode is still well confined in the waveguide core and the selected bending radius can ensure a ring resonator without extra loss penalty from the bend. Next the ring resonator is simulated with FIMMPROP. As shown in Fig 6-9 (e), the TE<sub>0</sub> mode in the bus waveguide is coupled to the TE<sub>0</sub> and TE<sub>1</sub> modes of the ring waveguide. For the  $2.6\mu\text{m} \times 0.4\mu\text{m}$  waveguide with  $250\mu\text{m}$  bending radius and

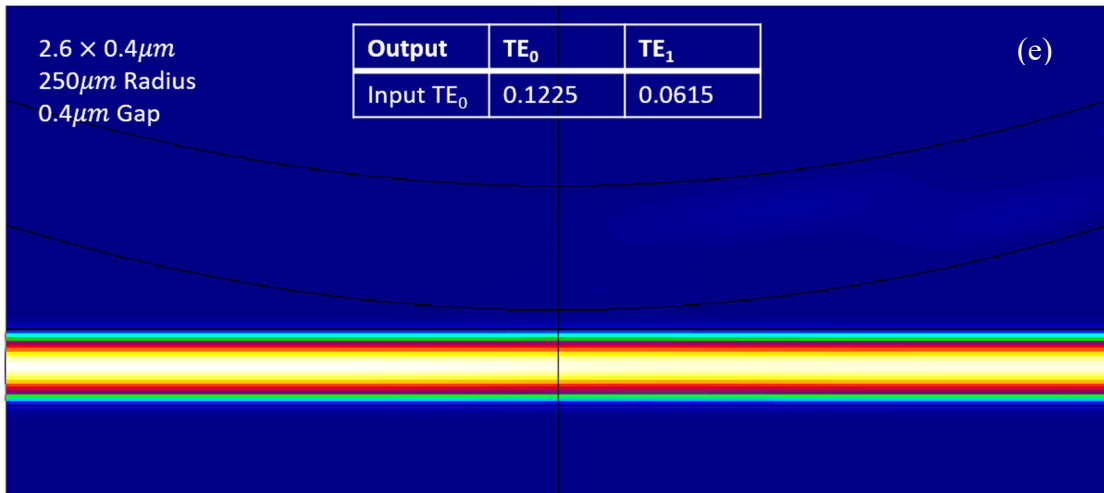
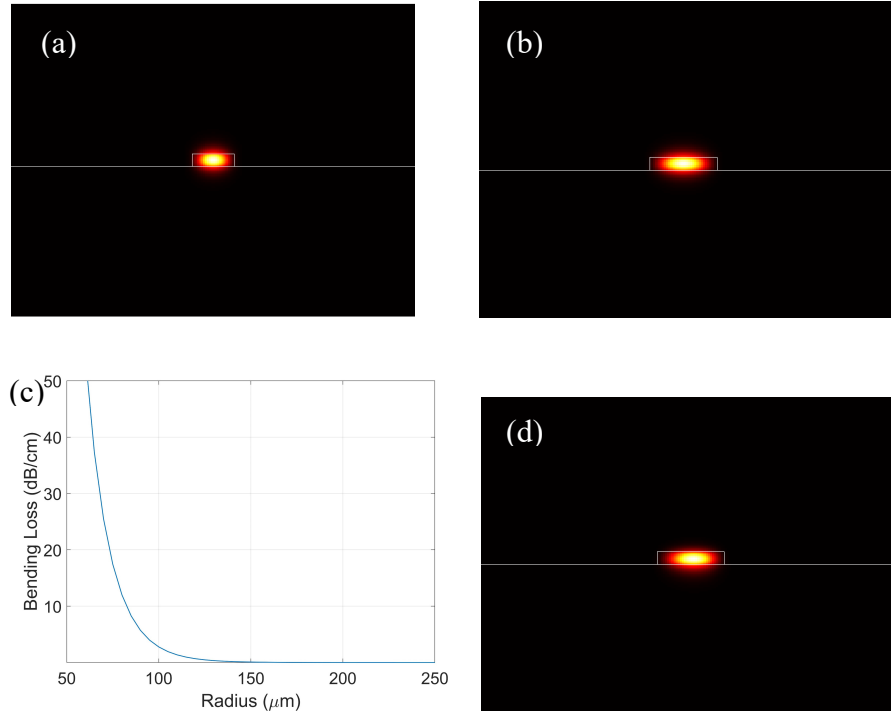


Figure 6-9 (a) Mode profile of the bus waveguide. (b) Mode profile of the ring waveguide. (c) Bending loss simulation of the TE mode with different bending radius, with the ring waveguide geometry. The bending loss is negligible when the bending radius exceeds 150  $\mu\text{m}$ . (d) Mode profile of the ring waveguide with 250  $\mu\text{m}$  bending radius. (e) Ring-bus coupling simulation.

400 nm gap, the TE<sub>0</sub>-TE<sub>0</sub> coupling strength  $\kappa$  with a ring-bus gap of 400nm is simulated to be 0.1225 at 1550nm, corresponding to  $t = 0.9925$ . To achieve a critically coupled or under coupled condition, the minimum loss of the ring resonator should be  $>0.4$  dB/cm with the given  $t$ . Experimentally, we design the gap to be 400, 600, and 800nm to identify the coupling condition better and extract the loss.

The fabrication of the AlN-on-sapphire chip is slightly different from Si<sub>3</sub>N<sub>4</sub> chip. For Si<sub>3</sub>N<sub>4</sub> chip, we use fluorine-based ICP-RIE to etch the Si<sub>3</sub>N<sub>4</sub>. In this case, the metal mask or negative resist mask works fine because they have a reasonably good selectivity ratio to the Si<sub>3</sub>N<sub>4</sub> film. However, chlorine-based ICP-RIE is required to etch the AlN because AlN is a III-V material. Neither metal mask nor negative resist can survive in the chlorine-based ICP-RIE. Instead, we deposit a layer of 500nm PECVD SiO<sub>2</sub> on top of the AlN before starting the fabrication process. Then, following the standard EBL process with ZEP-520A and metal deposition, the SiO<sub>2</sub> is etched with the fluorine-based ICP-RIE first. After removing the metal mask for the SiO<sub>2</sub> etch, the AlN is etched with chlorine-based ICP-RIE. As shown in Fig. 6-10, both the SiO<sub>2</sub> and AlN are etched correctly with the ICP-RIE. After the ICP-RIE etch, the remaining SiO<sub>2</sub> mask is removed by buffered oxide etchant (BOE), and a layer of 5 $\mu$ m PECVD SiO<sub>2</sub> is deposited as a top cladding layer.

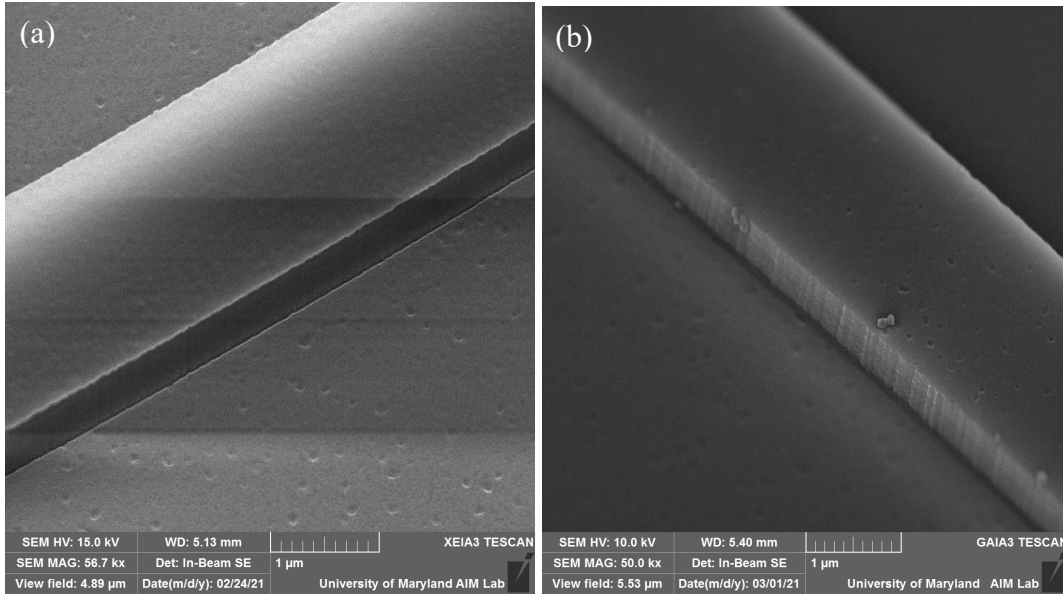


Figure 6-10 SEM images of the ring resonator. (a) Ring waveguide after the SiO<sub>2</sub> etch. (b) Ring waveguide after the AlN etch.

The experimental result is shown in Fig 6-11. Fig 6-11 (a) shows the overall transmission with different ring-bus gap. The resonance depth is more than 20 dB when the gap is 400 nm and at around 1630 nm, which is near critical coupled condition. As the ring-bus gap increases, the resonance depth decreases, indicating that the ring resonator with 600 nm and 800 nm gap is in under coupled condition. Fig 6-11 (b) shows the detailed transmission at wavelength between 1545 nm to 1554 nm with a 0.6  $\mu\text{m}$  ring-bus gap. There is one set of resonances in the ring resonator with a FSR of  $\sim 0.754$  nm. Since the TE<sub>1</sub> mode suffers a higher bending loss and scattering loss in the ring, the resonances observed comes from the TE<sub>0</sub>-TE<sub>0</sub> coupling. We further investigate the resonances from TE<sub>0</sub>-TE<sub>0</sub> coupling to extract the Q and losses of the ring resonator. Fig 6-11 (c) shows that the full width half maximum (FWHM) linewidth of the

resonance is 10.8 pm, corresponding to a loaded Q of 141000. With Equation 6-7, the  $Q_i$  is extracted to be 185000, corresponding to a propagation loss of 1.95 dB/cm. The extracted coupling strength  $\kappa$  is 0.1147, again agrees well with the simulation results and confirms the resonance originates from the TE<sub>0</sub>-TE<sub>0</sub> coupling.

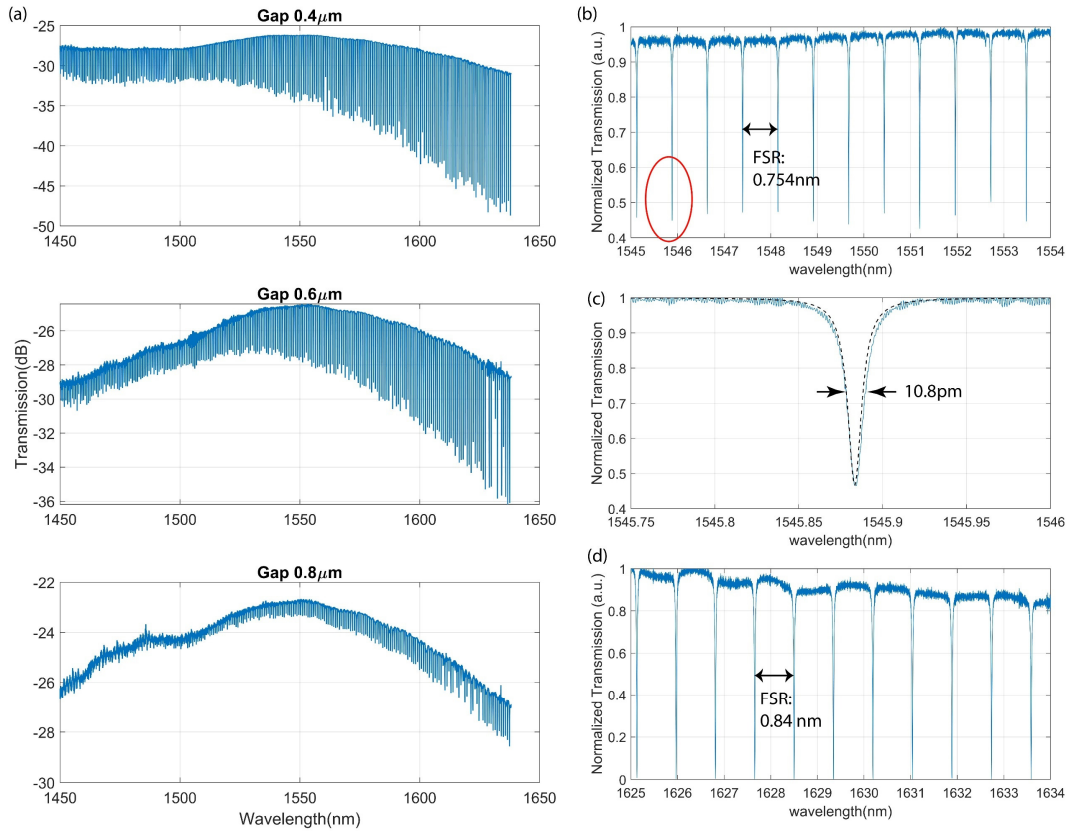


Figure 6-11 Experimental Results of the AlN ring resonator. (a) The overall transmission of the ring resonators with different gaps. (b) The zoomed-in transmission at 1545-1554 nm of the ring resonator with a gap of 0.6 μm. (c) The zoomed in transmission of the 0.6 μm gap at 1546nm. The linewidth of the resonance is measured to be 10.8 pm. (d) The zoomed-in transmission at 1625-1634 nm in the ring resonator with a gap of 0.4 μm.

Furthermore, we also investigate the waveguide losses at 1630nm since the overall transmission drops at a longer wavelength. As shown in Fig 6-11 (d), only the TE<sub>0</sub>-TE<sub>0</sub> coupling is observed at 1625-1634 nm in the ring resonator with a gap of 0.4  $\mu\text{m}$ . The FSR is measured to be 0.84 nm. The ring resonator is in the critically coupled condition at this wavelength because the mode is less confined at a larger wavelength, contributing to a larger coupling strength  $\kappa$ . The  $Q_L$  is measured to be 93000, corresponding to a  $Q_i$  of 186000 and a waveguide loss of 1.94 dB/cm. The extracted loss at 1630 nm is close to the loss at 1550 nm, showing no extra penalty at 1630nm due to a less confined mode. The bending loss with a 250  $\mu\text{m}$  bending radius at both 1550 nm and 1630 nm is negligible.

## 6.5 Discussion and Conclusion

In this chapter, we have investigated the waveguide loss performance on thicker Si<sub>3</sub>N<sub>4</sub> and AlN film with ring resonator, from theory to experiment. For the ring resonator based on 600nm Si<sub>3</sub>N<sub>4</sub> film, the loss is measured to be 0.18 dB/cm. Compared to the loss of 0.33 dB/cm that is measured on 300 nm Si<sub>3</sub>N<sub>4</sub> film, the loss is reduced by almost 50%, thanks to the loss reduction strategies that include increasing the waveguide thickness, using waveguide geometry that supports multiple modes, and using CHF<sub>3</sub>/O<sub>2</sub> gases in ICP-RIE etch to avoid sidewall redeposition. Compared to the best loss reported by other researchers [72,86,87], we still have room to improve the loss. Firstly, thermal annealing is an essential step to reduce the absorption peak at 1505 nm due to N-H bond, which exist in both the LPCVD Si<sub>3</sub>N<sub>4</sub> and silane PECVD SiO<sub>2</sub>. With thermal annealing, the N-H bond can be removed, and the loss due to material

absorption will be reduced, especially at the wavelength close to 1505 nm. The annealing process is also helpful in smoothening the waveguide boundary if the annealing is implemented before the top cladding SiO<sub>2</sub> deposition [2,57,67]. Secondly, a top cladding SiO<sub>2</sub> with higher quality, such as TEOS PECVD SiO<sub>2</sub>, HTO/LTO LPCVD SiO<sub>2</sub>, or thermal oxide from wafer bonding [72,88], will also be helpful to further reduce the loss. Thirdly, a chemical mechanical polish (CMP) process is also essential to achieve ultra-high-Q ring resonator ( $Q > 10$  million). Unlike the conventional polishing, CMP is assisted by chemical reaction to remove the surface materials. Compared to the conventional polishing, CMP can ensure a better film uniformity. While the LPCVD Si<sub>3</sub>N<sub>4</sub> has good film uniformity, the CMP can further improve film uniformity by polishing the Si<sub>3</sub>N<sub>4</sub> surface before the fabrication process. Ji *et al.* have shown that the root-mean-squared (RMS) roughness can be reduced from 0.38 nm to 0.08 nm with CMP [72], which can further reduce the scattering from the top surface roughness and improve the loss. Lastly, Spencer *et al.* reported that, in addition to the coupling loss and propagation loss, an excess loss at the ring-bus coupler  $\gamma$  may also reduce the  $Q_L$  [82], especially when the waveguide propagation loss  $\alpha L$  is low and comparable to  $\gamma$ . A specially designed weakly tapered gap coupler may help reduce the coupler excess loss as well as unwanted higher order or radiation modes coupling, and further improve the  $Q_L$ .

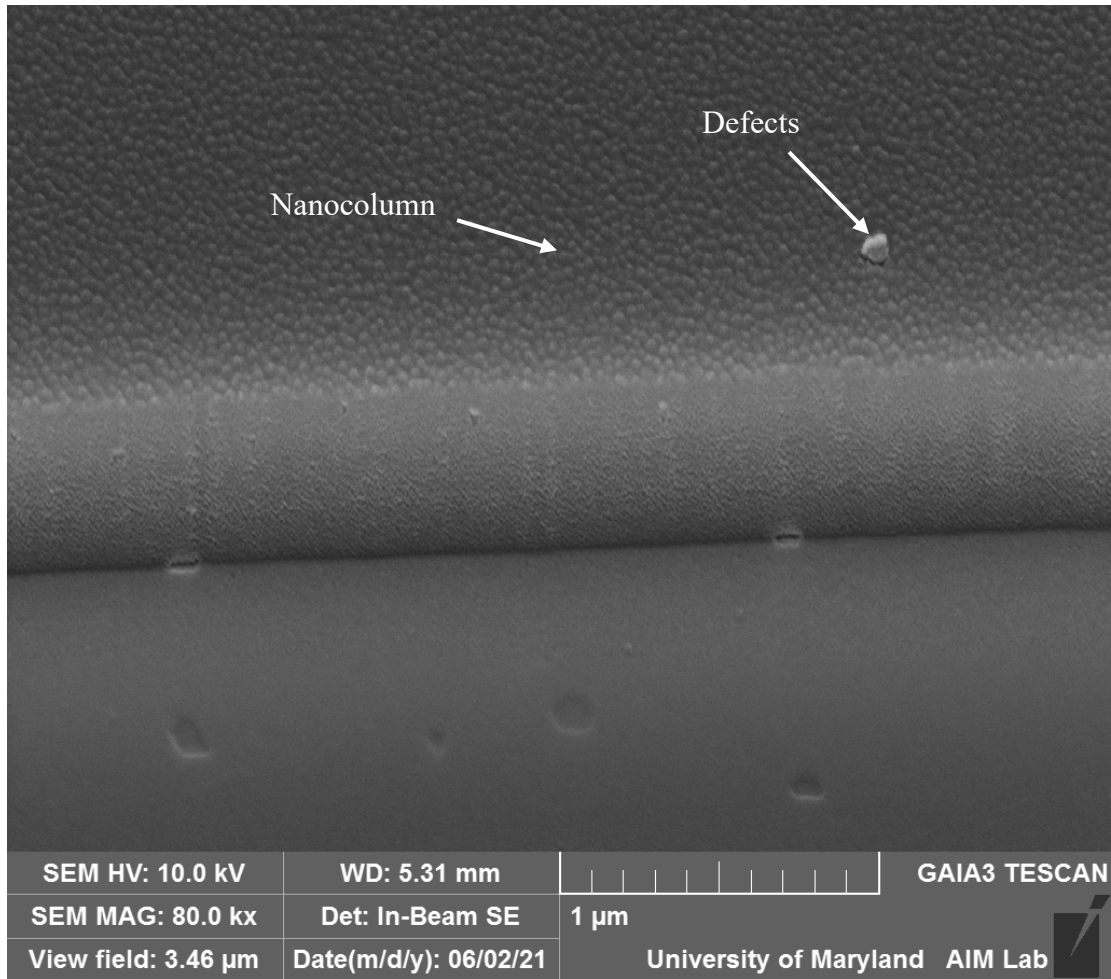


Figure 6-12 SEM image of the etched AlN waveguide. Nanocolumns and defects are seen on the waveguide top.

Compared to the loss results on the 600 nm  $\text{Si}_3\text{N}_4$  film, the loss results from the AlN film are less satisfactory. The primary reason is attributed to the film quality. As we mentioned in Section 6.4, the AlN is deposited with PVDNC. The surface of AlN grown by PVDNC is made of nanocolumns of AlN. While these nanocolumns may be beneficial for MBE growth applications, it can be problematic for etch-based photonics applications. The waveguide core, an unetched region, consists of AlN nanocolumns.

Thus, light scattering between nanocolumns within the waveguide core can be expected. The surface is also rough due to the nanocolumns. All these factors contribute to the higher loss of the AlN waveguide. By switching to a MBE-grown AlN film, the film quality can be improved. It has been shown that the loss in waveguide based on more than 1  $\mu\text{m}$  MBE-grown AlN can be as low as 0.13 dB/cm [76,77]. We envision a much lower loss with a MBE-grown AlN film, which can enable applications in astrophotonics and quantum information.

## Chapter 7 : On-Chip High Extinction Ratio Mach-Zehnder Interferometer for Exoplanet Discovery

### 7.1 Introduction to Exoplanet Discovery and Nulling Interferometer

Exoplanet discovery has always been of great interest to astronomer. However, it has long been difficult to directly detect an exoplanet not only because the exoplanet signal is several orders of magnitude weaker than its host star but because the distance between the exoplanet and its host star is way smaller than the distance between the exoplanet and earth. That's why astronomers didn't confirm any exoplanet detection until 1992 [89], and why a high angular resolution, high dynamic range detector is desirable for exoplanet discovery. There are two major techniques to fulfill the requirements for exoplanet discovery, coronagraph, and nulling interferometry. For the coronagraph approach, scientists design a telescopic attachment to block out the direct light from a host star so that the faint exoplanet signal can be observable. However, the emission and scattered light from the warm circumstellar dust, an analog to the interplanetary dust found in our solar system, will be a major source of noise for coronagraph [90–92]. Also, the coronagraph design depends on the exoplanet dimension [93], which makes it impossible to detect all kinds of exoplanet with a universal coronagraph design. Unlike the approach using coronagraph, nulling interferometry is working differently. Fig. 7-1 shows the schematic diagram of the nulling interferometer. Light from the star and the exoplanet travels to the earth and is

collected by two separate telescopes. The telescopes are separated by a baseline  $d$ . Since the star and exoplanet are at least hundreds of light years away from earth, the

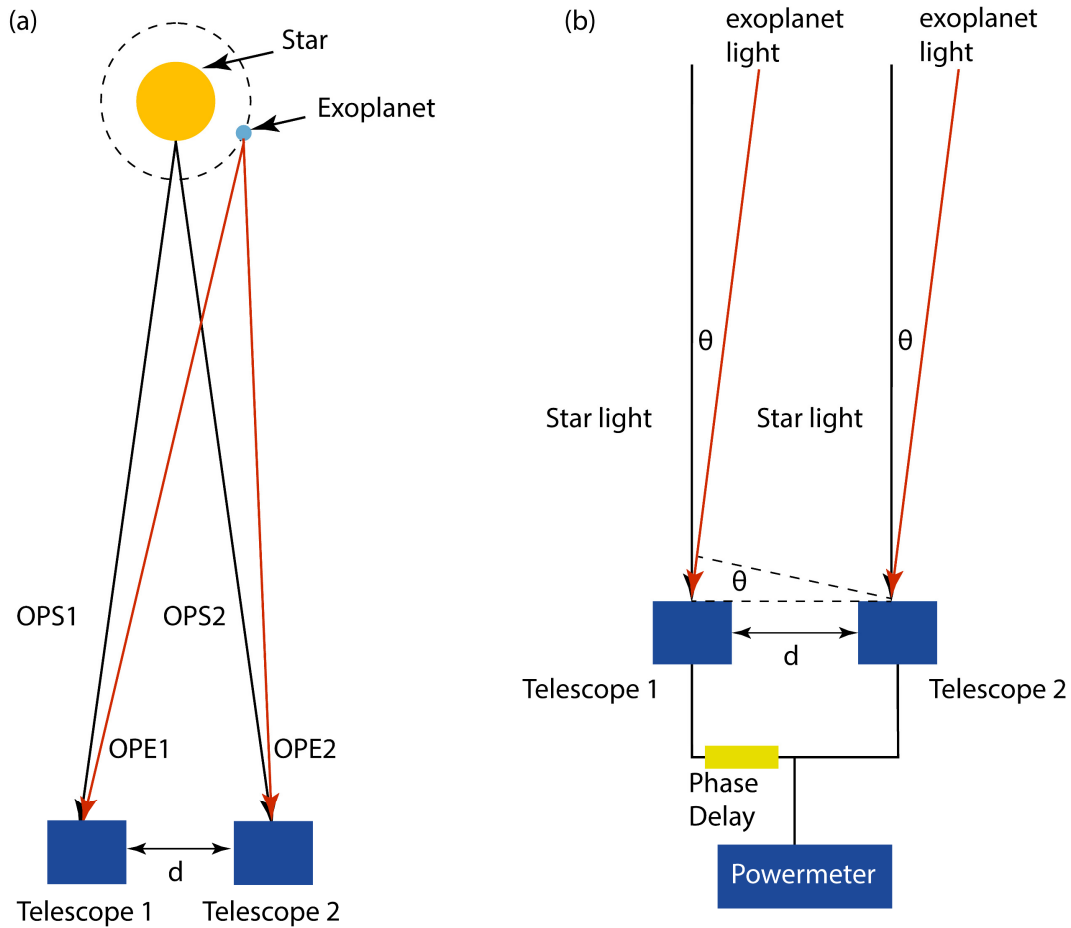


Figure 7-1(a) Schematic layout of the nulling interferometer. the optical path from the star (OPS) and the optical path from the exoplanet (OPE) is shown. (b) Schematic of the working principle of the nulling interferometer.

chance that two incoherent light beams can be simultaneously received by two telescopes are negligible. Thus, the light received by the telescopes are considered as

plane wave and coherent. While we can assume that the optical path difference (OPD) from a star to the two telescopes is 0, the OPD from the exoplanet to the two telescopes is not necessarily 0 and is highly dependent on the position of the exoplanet. Since the  $OPD_{\text{star}}$  (OPS) and  $OPD_{\text{exo}}$  (OPE) are different and the light is coherent, by introducing additional phase delay, one can suppress the light from the star while leaving the light from the exoplanet unaffected. Thus, the contrast between a star and an exoplanet is improved and direct exoplanet detection is possible. It is worth noting that, unlike coronagraph, whose design is dependent on the exoplanet size, the design of a nulling interferometer can be a universal design. The nulling depth, namely the suppression ratio of the star light, is only dependent on the phase control precision. The star light can be fully suppressed when the phase difference between the two optical paths from the star to the two telescopes is exactly  $(2n + 1)\pi$ . Moreover, the nulling interferometer can provide superior angular resolution. As shown in Fig. 7-1 (b), suppose that the tiny angular shift between the exoplanet and the star is  $\theta$ , and assume that the OPS is 0, the OPE will be  $d\sin\theta \approx d\theta$ . Thus, the phase difference  $\varphi_{\text{exo}}$  would be  $\varphi_{\text{exo}} = k \times OPD = \frac{2\pi}{\lambda} d\theta$ . By assuming OPS = 0, The maximum angular resolution can be achieved when OPE =  $\lambda/2$ , which means that  $\varphi_{\text{exo}} = \pi$ . Hence, the angular resolution of nulling interferometer can be given by:

$$\theta = \frac{\lambda\pi}{2\pi d} = \frac{\lambda}{2d} \quad (7 - 1)$$

which is independent from any star and exoplanet property. Typically, the angular resolution can be as high as a few milli-arcseconds, which is favorable for exoplanet detection.

## **7.2 Recent Advances and Challenges in Nulling interferometer**

In 1978, Bracewell first proposed that a spinning infrared nulling interferometer would be a way to detect an exoplanet [94]. While some scientists have demonstrated application of a the nulling interferometer using free space optics [95], the vast majority of research interests have been geared toward using integrated optics based nulling interferometers. Comparing with free space optics, an integrated photonics platform shows great advantage in terms of system stability and compactness. While the wavelength of the light emitted from an exoplanet can vary from the visible to the mid infrared, the astronomical H-band (1.5-1.8  $\mu\text{m}$ ), L-band (3-4  $\mu\text{m}$ ) and N-band (7.5-14  $\mu\text{m}$ ) are particularly favorable for exoplanet research since it represents different stage of exoplanet formation. Although the N-band can be an important window for mature exoplanet detection, the poor performance of optical detectors in the N-band limits the exoplanet detection. While there is extraordinary contrast in the L-band, achieving good integrated optics performance in mid infrared remains challenging because the major integrated photonics material systems, including silicon on insulator (SOI),  $\text{Si}_3\text{N}_4/\text{SiO}_2$ , and silica on silicon, are not transparent in the mid infrared and new platforms such as lithium niobate and chalcogenide glass are still under development. Thus, the H-band nulling interferometer is still the most mature platform to date. In 1999, Berger et.al. demonstrated a 2-channels nulling interferometer based on silica-

on-silicon Y-branch beam combiner [96]. As shown in Fig. 7-2(a), the light from two telescopes is coupled onto the chip through fiber-chip butt coupling and are split by the first two Y-junction, then the two coherent lights interfere at the reverse Y-junction and the star light get suppressed. Based on the Y-branch beam combiner scheme, researchers further demonstrated multi-baseline integrated optics beam combiner on silica-on-silicon and the integrated nulling interferometer has already been installed in the European Southern Observatory as a very large telescope interferometer (VLTI) [97,98]. Although the VLTI has achieved great success in H-band, researchers are developing next-generation mid-infrared nulling interferometer. Chalcogenide glass-based nulling interferometer has thus been developed recently. Unlike conventional CMOS compatible materials, fabrication on chalcogenide glass mainly rely on direct laser inscription, giving researchers the capability of making full 3D photonic structure. However, the index contrast of laser inscribed waveguide is small compared with regular SOI or silicon nitride waveguide and thus limits the compactness of the chalcogenide glass photonic chip, whose footprint is typically several  $\text{cm}^2$ . Recently, a Y-branch splitter and directional coupler-based nulling interferometer components in chalcogenide glass has been demonstrated and researchers are working to integrate these components [99]. Besides, Goldsmith *et.al.* also proposed a multimode interferometer (MMI) based nulling interferometer as shown in Fig. 7-2 (b) [100]. Their simulation results show that the 2-channel nulling interferometer can reach as high as 60 dB extinction ratio within a 30 nm wavelength range in the astronomical L-band. Since the traditional Y-branch splitter or directional

coupler-based nulling interferometer can only achieve around 95% contrast, the proposed MMI-based nulling interferometer outperforms the traditional nulling interferometer and is a perfect candidate for next-generation integrated nulling interferometers.

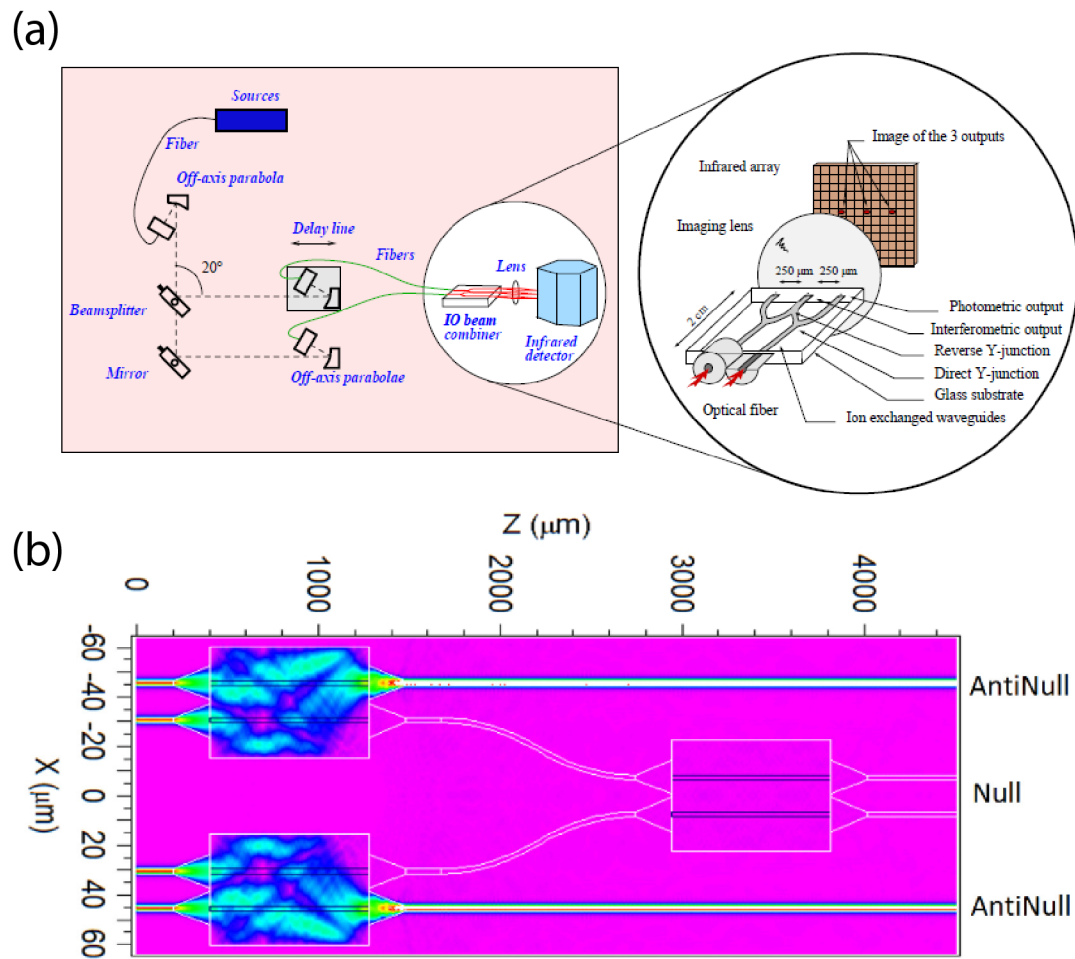


Figure 7-2 (a) Schematic of Y-branch nulling interferometer [96]. (b) Schematic of the MMI-based nulling interferometer [100].

As a summary, researchers have demonstrated Y-branch based integrated nulling interferometer in the astronomical H-band and are now working on nulling

interferometer in the astronomical L-band. However, the extinction ratio of the Y-branch splitter or directional coupler-based nulling interferometer is still unsatisfactory, which limits the exoplanets discovery process. Thus, a compact, high contrast integrated nulling interferometer remains challenging, and further research is required to address the issue.

In this chapter, we investigate a low loss, high contrast integrated Mach Zehnder Interferometer (MZI) based on two cascaded MMI on a  $\text{Si}_3\text{N}_4$ -on- $\text{SiO}_2$  chip, from simulation to experiment. We demonstrate a MMI-MZI with the largest extinction ratio of 58 dB on 300 nm  $\text{Si}_3\text{N}_4$ , and a thermally tunable MMI-MZI with the largest extinction ratio of 50 dB, with the tuning power of about 400 mW. We further analyze the factors that limit us from achieving a higher extinction ratio and proposed an integrated TM filter to solve this problem. With the demonstrated high extinction ratio MMI-MZI, it can be easily used as a nulling interferometer and facilitate future exoplanet discovery.

### **7.3 MMI-MZI Design**

There are several considerations in designing the high extinction ratio MMI-MZI for astrophotonics application before we start the simulation. While simultaneously achieving broadband and high extinction ratio MMI-MZI is highly desirable for astrophotonics application, it is impossible due to the nature of MMI. As we discussed in Chapter 4, the bandwidth of the cascaded MMIs device purely depends on the bandwidth of a single MMI. The bandwidth of a MMI is related to the MMI's dimension:

$$\frac{\delta\lambda_0}{\lambda_0} \approx \frac{\delta L}{L} = \frac{2\delta W_e}{W_e} \quad (7 - 2)$$

Where the  $\lambda_0$  is the central wavelength of the MMI bandwidth,  $L$  is the length of the MMI, and  $W_e$  is the effective width of the MMI, which can be written as [38]

$$W_e = W + \left(\frac{\lambda_0}{\pi}\right) (n_r^2 - n_c^2)^{-\frac{1}{2}} \quad (7 - 3)$$

Obviously, from Equation 7-2 and 7-3, the bandwidth decreases with the increase of the dimension of the MMI. However, MMI works based on the “self-imaging” principle. The more modes the MMI supports, the better the imaging quality will be. For the MMI-MZI, a MMI supporting more modes indicates a wider MMI, and better imaging quality indicates a higher extinction ratio. Thus, there is a fundamental tradeoff between larger bandwidth and a higher extinction ratio. Fig. 7-3 (a-b) shows the simulation results of the MZI-MMI. While the MZI with 10  $\mu m$  width, which supports 8 guided TE mode, has a 3-dB bandwidth larger than 200 nm, the largest extinction ratio is only ~40 dB. Instead, the MZI with 15  $\mu m$  width, which supports 10 guided TE modes, has an extinction ratio better than 60 dB with a reduced 3-dB bandwidth of around 80 nm. In our case, a high extinction ratio is more critical for the exoplanet discovery. Hence, we are putting our effort into improving the extinction ratio in this work.

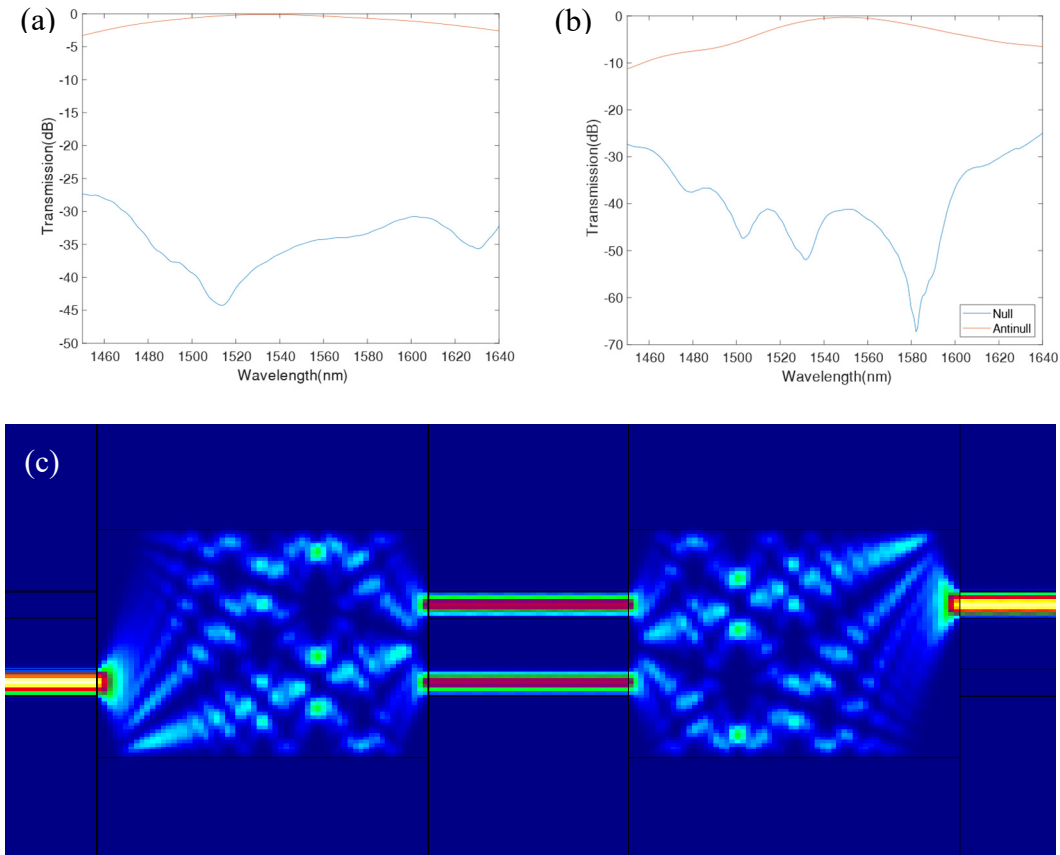


Figure 7-3 Simulation Results. (a) Simulation results of the MZI with 15  $\mu m$  MMI transmission at the null port and anti-null port. (b) Simulation results of the MZI with 10  $\mu m$  MMI transmission at the null port and anti-null port. (c) Simulated mode profile of the MMI-MZI.

In this work, we design the dimension of the MMI to be  $15 \times 166.23 \mu m^2$ . The port width is designed to be  $1.8 \mu m$  with a separation of  $5.1 \mu m$  between two ports of the MMI. Such design enables the paired interference mode, as we described in Chapter 4 [38,101], and the MMI dimension is reduced by three-fold. The FIMMPROP simulated transmission at two output ports and mode profile are shown in Fig 7-3 (b-c).

## 7.4 Experimental Results

Before we can investigate the high extinction ratio MMI-MZI performance, the TM noise on the chip should be minimized first. The TM noise is an important factor that prevent us from getting high extinction ratio MMI-MZI. Since the MMI is optimized for TE polarization, when a TM polarized light goes into the MMI-MZI, a small portion of the TM light will still go to the null port, which will limit the overall extinction ratio. As shown in Fig. 7-4 (a-c), with a TM input, the light does not perfectly converge in the output port, and the simulated extinction ratio will decrease from 70 dB to around 40 dB. Unlike the TM noise we discussed in Chapter 4, the TM noise must be removed in a broadband for the MMI-MZI, i.e., more than 200 nm. Thus, the Bragg grating based TM filter we demonstrated in Chapter 4 no longer works. Here, we utilize the different bending loss for TE mode and TM mode to remove the TM noise. As shown in Fig. 7-4 (d), as the bending radius decreases, the bending loss increases significantly for both the TE mode and TM mode. However, with a bending radius of  $50\ \mu\text{m}$ , while the bending loss for TM mode is 2.4 dB/180° bend, the bending loss for TE mode is still negligible. With the bending loss difference between TE and TM modes, we can implement on-chip broadband TM filtering. We test the  $50\ \mu\text{m}$  bends TM filter with a simple Bragg grating. As shown in Fig. 7-4 (e), without the broadband TM filter based on bending waveguide, the TM noise floor is at around -20 dB, just as what we have seen in Chapter 4. When adding the TM filter to the Bragg grating, the TM noise is suppressed by more than 25 dB with 720° or longer  $50\ \mu\text{m}$  radius bends. It is also worth noting that the overall insertion loss of the TE mode

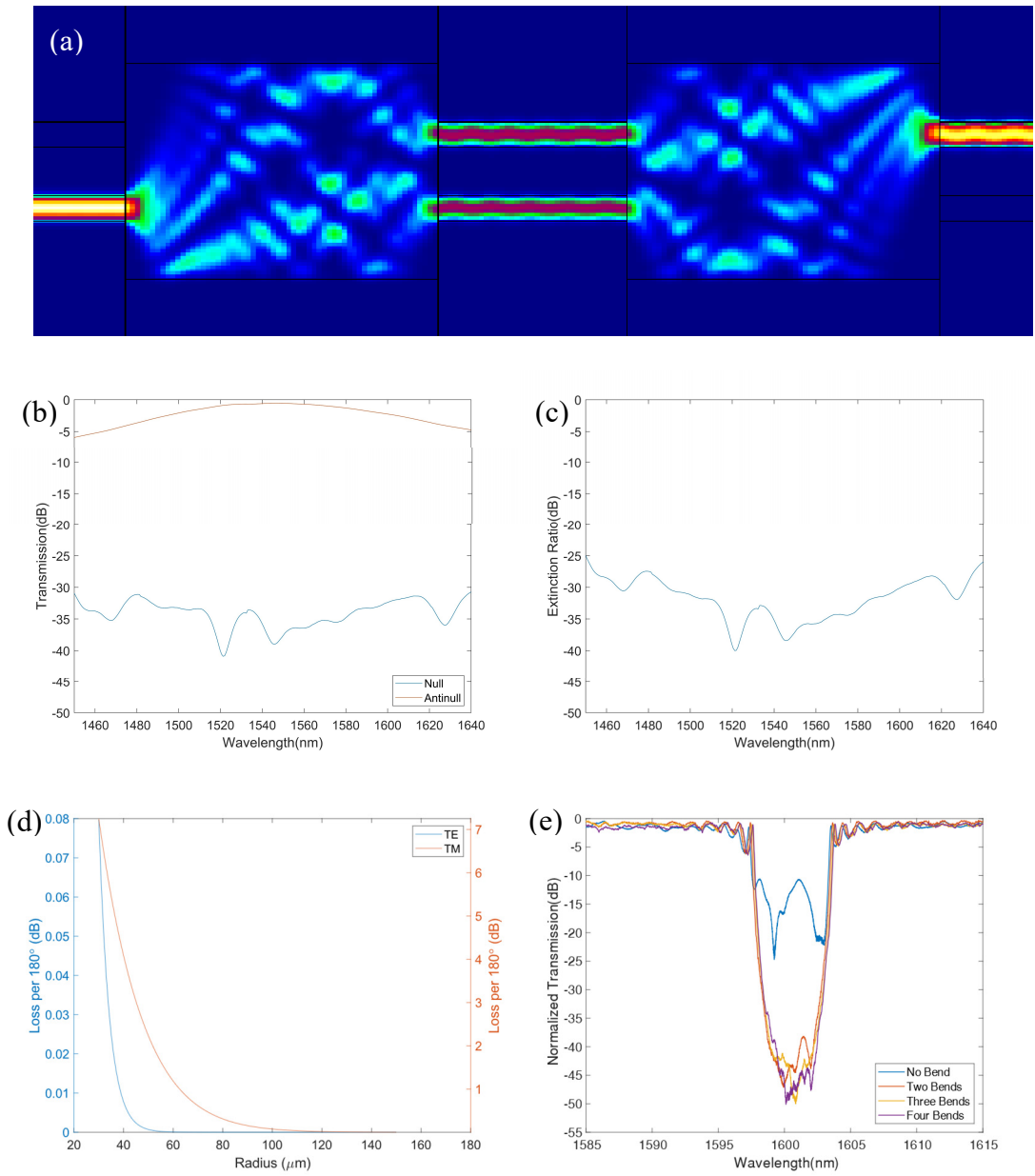


Figure 7-4 (a) Simulated mode profile of the  $15 \mu\text{m}$  MMI-MZI with a TM input. (b) Simulated transmission results of the  $15 \mu\text{m}$  MMI-MZI with a TM input. (c) Simulated extinction ratio of the MZI with  $15 \mu\text{m}$  MMI with a TM input (d)TM transmission on the MMI needs to be simulated. (e)Experimental results of the bend waveguide TM filter.

remains the same, which experimentally shows that the TE mode bending loss is still negligible in  $50 \mu\text{m}$  radius bends. The stronger than simulated TM suppression is attributed to the fact that the bending loss simulation does not take the mode mismatch loss between straight waveguide mode and bend mode into consideration. Thus, the experimental TM suppression can be higher than the simulated results. In the following high extinction ratio MZI experiment, a TM filter with  $720^\circ$   $50 \mu\text{m}$  radius is always included in all MZI designs.

We first test the MMI-MZI without thermal control. The device is fabricated with the standard ZEP-520A fabrication process as described in Chapter 2. Fig. 7-5 shows the SEM images of the fabricated devices. Here, the two MMIs are connected by a  $100 \mu\text{m}$  waveguide. As shown in Fig. 7-5 (b), the device's dimension agrees reasonably well with the design.

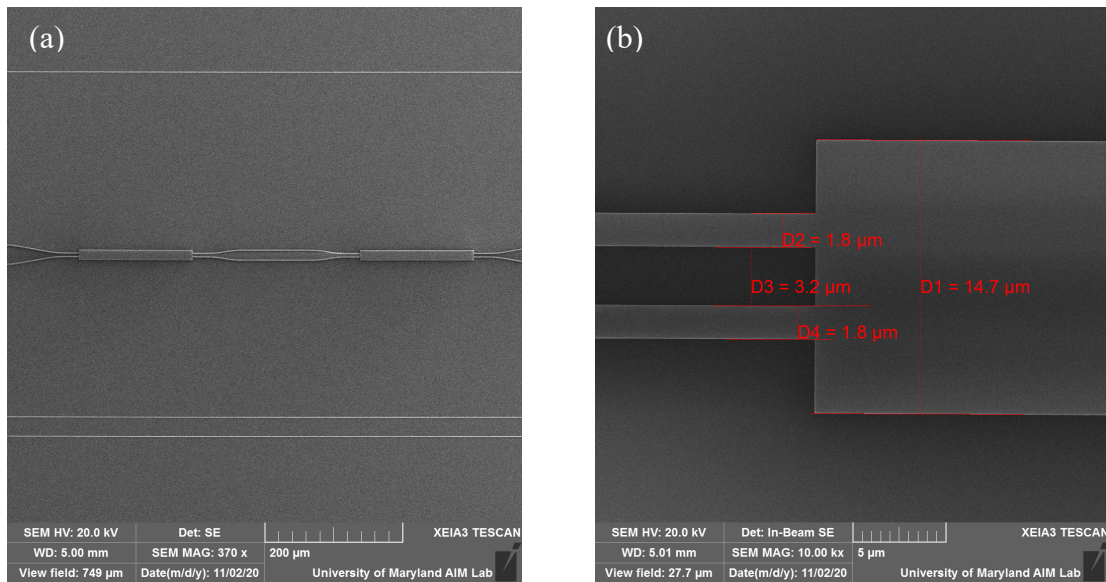


Figure 7-5 SEM images of the fabricated devices. (a)Overall device (b)Zoomed in image of the MMI.

The measurement results are shown in Fig. 7-6. Experimentally, with a TE polarized input, the maximum anti-null transmission is measured at around 1540 nm with an insertion loss of  $\sim 1$  dB. The measured 3-dB bandwidth is 94.3 nm. The highest extinction ratio extracted from the transmission is approximately 58 dB, as shown in Fig 7-6 (b). The device performance agrees well with the simulation results.

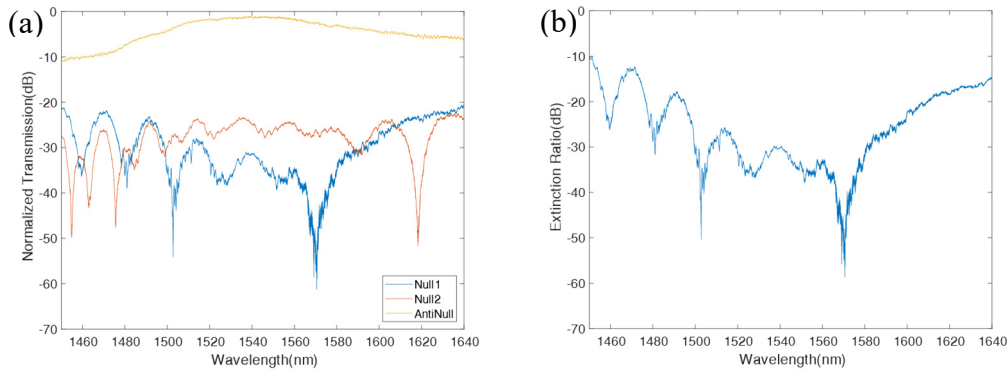


Figure 7-6 Experimental results of the MMI-MZI. (a) Transmission of the null port and anti-null port, normalized to the transmission of a straight waveguide. (b) Extinction ratio extracted from the transmission.

Next, we investigate the MMI-MZI with thermal control. Experimentally, to realize the thermal control, we deposit a total of 130 nm nichrome microheater on top of the PECVD SiO<sub>2</sub> cladding. The microheater is patterned with an Elionix overlay feature. As shown in Fig. 7-7, we successfully get a double alignment precision better than  $1 \mu\text{m}$ , critical for efficient thermal phase control. Since we need  $\pi$  phase shift capability for the MZI but the thermo-optic coefficient of both Si<sub>3</sub>N<sub>4</sub> and SiO<sub>2</sub> are small ( $2.4 \times 10^{-5}/\text{K}$  and  $0.96 \times 10^{-5}/\text{K}$ , respectively) [102], the two MMIs are separated by 500

$\mu\text{m}$ , and the heater are designed to be  $500 \times 10 \mu\text{m}^2$  to allow larger thermal tuning capability.

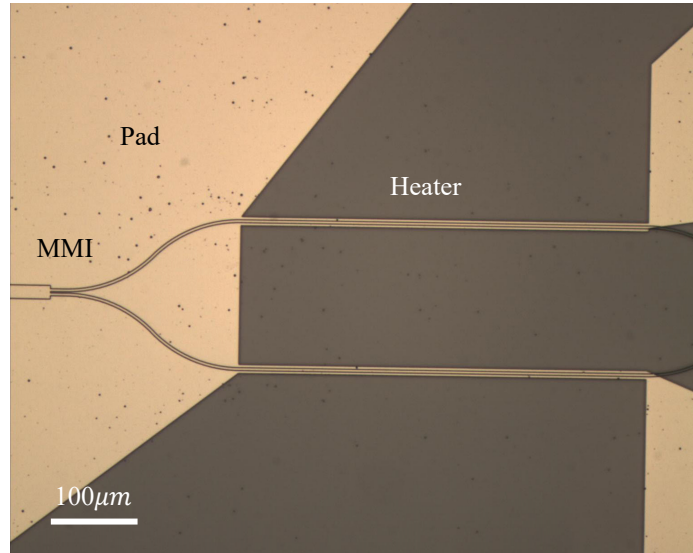


Figure 7-7 Microscope image of the microheater.

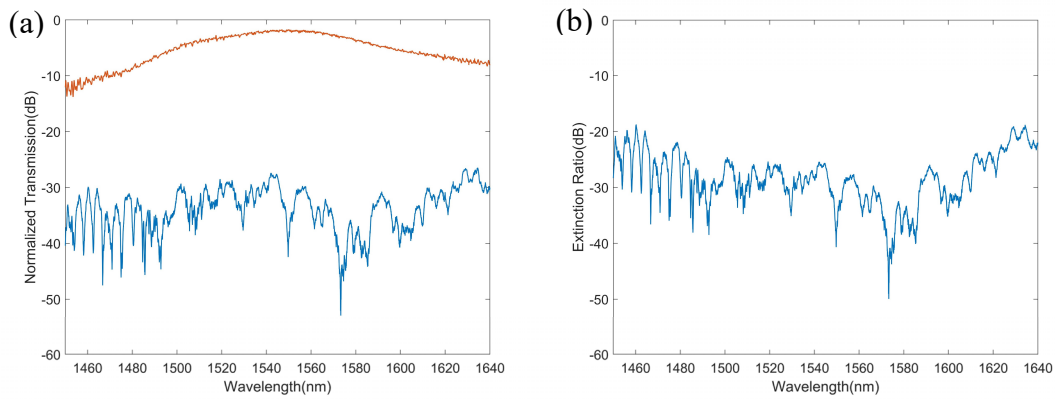


Figure 7-8 Experimental results of the thermally controlled MZI-MMI. (a) Transmission of the null port and anti-null port, normalized to the transmission of a straight waveguide. (b) Extinction ratio extracted from the transmission.

The measurement result of the thermally tunable MZI-MMI is shown in Fig 7-8. Here, the insertion loss of the MZI is measured to be 1.70 dB, and the 3-dB bandwidth is 90.1 nm. By applying a tuning power of about 400 mW, the highest extinction ratio is measured to be -50 dB.

## 7.5 Discussion and Conclusion

Overall, the results shown above agree well with the simulation results. Thanks to the on-chip broadband TM filter, we managed to achieve an extinction ratio of 58 dB with the MMI-MZI and an extinction ratio of 50 dB with the thermally tunable MMI-MZI. The MMI-MZI has a reasonably small footprint, and the loss of the MMI-MZI is less than 2 dB, both of which are highly desirable for the astrophotonics applications. Compared to the 70 dB simulated extinction ratio, we still have room to improve. The primary reason for the difference is fabrication imperfection. When the light propagates in the MMI, it can be expanded into the eigenmodes of the MMI. The self-imaging process purely relies on an accurate MMI footprint and port separation. For the MMI-MZI, ideally, the first MMI will equally split the light with a  $\pi/2$  phase difference, and the second MMI will combine the two lights. But this is impossible when fabrication error occurs. Although we have perfect control over the phase difference between two arms through the thermal control, we cannot control the power difference between two arms with the two MMIs schematics. Fig. 7-9 shows the simulated light propagation profile in the second MMI when a 10% power difference between two MZI arms exists. While the light will still mainly converge to the anti-null port, the null port is not perfectly nulled, and the extinction ratio will drop. As

shown in the inset of Fig. 7-9, the extinction ratio at 1550 nm drops from 47.49 dB to 26.12 dB when the power difference increases from 0 to 10%.

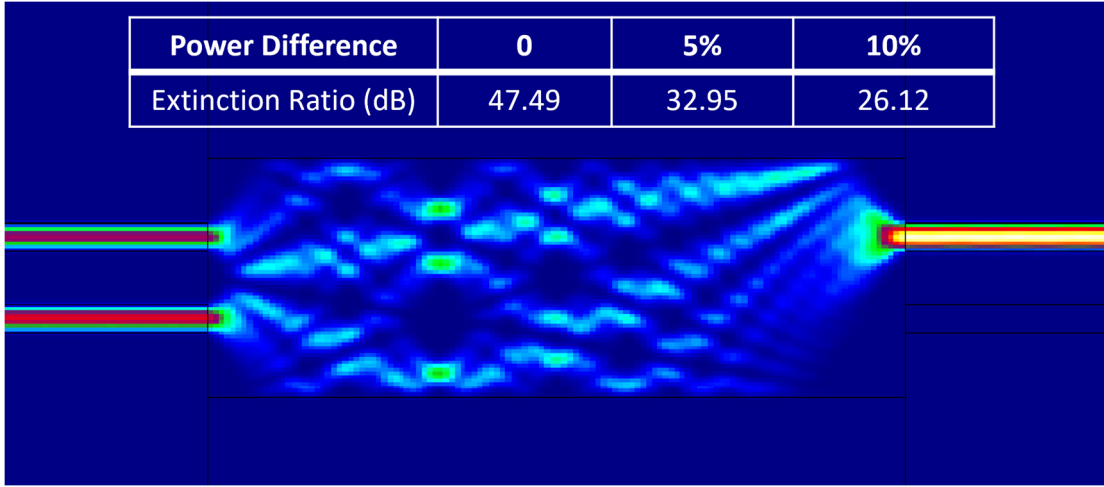


Figure 7-9 Simulation results of a MMI with two inputs. The phase difference and power difference between the two inputs light is  $\pi/2$  and 0.1, respectively. The inset table shows the simulated extinction ratio with different power difference.

Researchers have proposed cascaded MZI schematics to solve this problem [103,104]. As shown in Fig. 7-10, in the cascaded MZI schematics, the first MZI is used to fine-tune the power imbalance so that there is no power difference at the two outputs of the first MZI. Then, with phase control on the second MZI, a  $\pi/2$  phase difference can also be achieved. Thus, both power difference and phase difference conditions are satisfied, and the MZI will work perfectly.

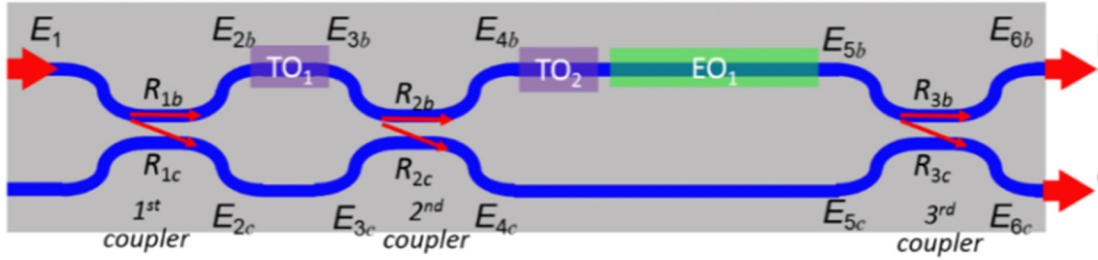


Figure 7-10 Schematics of cascaded MZI. [103]

With all the progress demonstrated in this chapter, the MMI-MZI will be a perfect candidate for implementing a nulling interferometer. As discussed in Section 7.3, by increasing the width of the MMI, the extinction ratio can be further improved. We envision that such a high extinction ratio, low loss MMI-MZI can facilitate future direct exoplanet discovery.

## Chapter 8 : Conclusions and Perspectives

In this dissertation, we have discussed different fabrication techniques for implementing a range of photonics devices. In particular, we have investigated multiple integrated photonics devices, including echelle grating, add-drop filter, Fabry-Pérot Bragg gratings, ring resonators, and MMI-MZI device, and their applications in astrophotonics and quantum information. Since every photon counts for astrophotonics and quantum information, low loss is an essential requirement for the integrated photonics devices. Thus, we have used  $\text{Si}_3\text{N}_4$ , a well-known low-loss photonics material, for all the integrated photonics devices. We have successfully demonstrated a low-loss performance on all the implemented devices.

The echelle grating discussed in Chapter 3 is essential for on-chip spectrometry. Compared to AWG, echelle grating features a smaller footprint. Different from the previous work on echelle grating, we propose to use silver, instead of distributed Bragg reflector, as the reflector to maximize the bandwidth and minimize the on-chip loss of the echelle grating. After addressing the stitching error problem originating from the EBL process, we have demonstrated a 5-channel  $\text{Si}_3\text{N}_4/\text{SiO}_2$  echelle grating with 1.39 dB on-chip insertion loss, 4.929 nm channel spacing, a 1300 spectral resolution, a 1.2dB channel non-uniformity and better than -30 dB crosstalk. The combined performance is better than any reported echelle grating. It is envisaged that the echelle grating can have a great potential for astrophotonics application.

The add-drop filter discussed in Chapter 4 is realized based on two  $2\times 2$  MMIs and two Bragg gratings. Specifically, the CWBG-MMI add-drop filter features the

capability of implementing add-drop operation on an arbitrary amount of channel with arbitrary spacing, thanks to the LP/LA algorithm that designs the CWBG. We have demonstrated a CWBG-MMI add-drop filter with five arbitrarily spaced channels with on-chip loss of  $< 1$  dB, a rejection ratio of  $> 40$  dB, and a 3-dB line width of 1.2 nm, and a spectral precision of better than  $\pm 0.2$  nm. To our knowledge, this is the first CWBG-MMI multi-channel add-drop filter ever made. The LP/LA algorithm gives further flexibility to design filter with more notches and narrower linewidth.

We have also demonstrated an on-chip FWM signal with a FPBG cavity going from theory, to grating optimization and to an experimental demonstration near 1590 nm in Chapter 5. A -37.44 dB FWM conversion efficiency is observed with a 5.3 dBm on chip pump power. A ten-fold loss reduction using tapered grating has been demonstrated, making the high efficiency FWM process possible. Furthermore, dispersion compensation is realized with the help of the Bragg grating dispersion and thermal phase control.

We then demonstrated multiple loss reduction techniques and characterized the waveguide loss using ring resonators in Chapter 6. With a thicker  $\text{Si}_3\text{N}_4$  and waveguide supporting multiple guided modes, the waveguide loss has been further reduced from 0.33 dB/cm to 0.18 dB/cm. With these progresses, the on-chip FPBG-FWM efficiency can be higher, and the SFWM will be possible in the future. We have also explored a new material platform, AlN-on-sapphire, due to its strong second-order nonlinearity and ultrabroad transparent window. We have demonstrated a loss of the AlN waveguide

of 1.95 dB/cm. All the innovations pave the way for future quantum information applications.

Lastly, The MMI-MZI discussed in Chapter 7 can be used for the exoplanet discovery by nulling the light from the star while leaving the light from the exoplanet unchanged. For the exoplanet discovery purpose, high extinction ratio of the MMI-MZI is critical. We have demonstrated an MMI-MZI with an extinction ratio of 58 dB by introducing a bending-waveguide-based broadband TM filter. We have also shown the thermal tuning capability for the MMI-MZI, and an extinction ratio of 50 dB is realized. The MMI-MZI has a reasonably small footprint and the loss of the MMI-MZI is less than 2 dB.

There are multiple directions for future works. For the add-drop filter, recently our group have demonstrated a spiral CWBG which has 55 notches and smaller overall footprint [105]. We envision that the spiral CWBG can be integrated into the CWBG-MMI add-drop filter, so that an add-drop filter with more notches and smaller footprint can be realized in the future, which may be critical for the astrophotonics applications. To further reduce the loss, multiple more advanced fabrication techniques, such as CMP, thermal annealing, can be used. Optimizing the waveguide geometry can also help reduce the loss and improving the FWM efficiency. For the MMI-MZI, we expect that the extinction ratio can be improved by using a wider MMI and a cascaded MMI scheme to balance the power difference due to fabrication errors. Lastly, with further reduction of the loss of AlN waveguides, new applications in astrophotonics and quantum information will emerge. Replacing the PVDNC grown AlN sample by MBE-

grown single crystal AlN sample will lead to much lower losses. Since it has been shown on SOI platform that a waveguide with thick film but shallow etches can make the mode less confined and experience less sidewall scattering losses [106], a thicker AlN film with shallow etches is also a promising approach to low loss waveguides.

## Appendix A: Detailed Fabrication Recipes

### Ebeam Lithography

#### ZEP-520A:

- 1) Spin coat ZEP-520A on sample with 4500 rpm for 1 min (resist thickness is around 300 nm)
- 2) Prebake with hotplate at 180 °C for 5 min
- 3) Spin coat aquaSAVE (conductive polymer to prevent charging effect in EBL) with 4500 rpm for 30 seconds.
- 4) Expose in 100kV EBL system with 300  $\mu\text{C}/\text{cm}^2$  dose.
- 5) Develop with DI water for 30 seconds, ZED-N50 developer for 1 min, and IPA for 30 seconds.
- 6) Ultrasonic lift-off for at least 1 min with remover PG

#### maN-2405:

- 1) Spin coat ma-N 2405 with 3000 rpm for 30 seconds.
- 2) Pre-bake with hotplate at 100 °C for 1 min.
- 3) Spin coat aquaSAVE with 3000 rpm for 30 seconds.
- 4) Expose in 100kV EBL system with 400  $\mu\text{C}/\text{cm}^2$  dose.
- 5) Develop with water for 30 seconds, ma-D 525 developer for 45 seconds, and DI water for 30 seconds.
- 6) Oxygen plasma cleaning (parameter: 30W RF power, 150W ICP power, 40 sccm O<sub>2</sub>) for 1 min after dry etch.

## ICP-RIE Etch

ICP-RIE Fluorine Etcher for Si<sub>3</sub>N<sub>4</sub> Etch:

ICP Power 500W

RF power 25W

Pressure 15 mTorr

CHF<sub>3</sub>/O<sub>2</sub> = 100/10 sccm

The measured etch speed from this recipe is about 100nm/min, with a vertical etch sidewall. The selectivity ratio between metal mask and Si<sub>3</sub>N<sub>4</sub> is larger than 20:1 and the selectivity ratio between negative-tone resist to Si<sub>3</sub>N<sub>4</sub> is about 1:1.

ICP-RIE Chlorine Etcher for AlN Etch:

ICP Power: 500W

DC Bias: 220V

Pressure: 5 mTorr

Gas: Cl<sub>2</sub>/BCl<sub>3</sub>/Ar = 40/5/8 sccm

This recipe's measured AlN etch rate is about 175nm/min, with directionality of 70°-80°. The selectivity ratio between AlN and SiO<sub>2</sub> is about 3:1.

## PECVD

Gas: SiH<sub>4</sub>/N<sub>2</sub>/N<sub>2</sub>O = 8.5/161.5/710 sccm

Pressure: 1000 mTorr

RF Power: 20W

The measured deposition rate is around 71nm/min.

## Bibliography

1. X. Ji, F. A. S. Barbosa, S. P. Roberts, A. Dutt, J. Cardenas, Y. Okawachi, A. Bryant, A. L. Gaeta, and M. Lipson, "Ultra-low-loss on-chip resonators with sub-milliwatt parametric oscillation threshold," *Optica* **4**, 619-624 (2017).
2. M. H. P. Pfeiffer, A. Kordts, V. Brasch, M. Zervas, M. Geiselmann, J. D. Jost, and T. J. Kippenberg, "Photonic Damascene process for integrated high-Q microresonator based nonlinear photonics," *Optica* **3**, 20-25 (2016).
3. X. Zhang, K. S. Chen, R. Ghodssi, A. A. Ayón, and S. M. Spearing, "Residual stress and fracture in thick tetraethylorthosilicate (TEOS) and silane-based PECVD oxide films," *Sensors Actuators, A Phys.* **91**, 373–380 (2001).
4. Y. Hu, "Ultra-low-loss silicon nitride waveguide gratings and their applications in astrophotonics," Doctoral dissertation, University of Maryland, College Park, 2020
5. S. K. Ray, C. K. Maiti, S. K. Lahirib, and N. B. Chakrabartib, "TEOS-Based PECVD of Silicon Dioxide for VLSI Applications" *Adv. Mater. Optic. Electron.* **6**, 73-82 (1996).
6. S. Pathak, P. Dumon, D. Van Thourhout, and W. Bogaerts, "Comparison of AWGs and Echelle Gratings for Wavelength Division Multiplexing on Silicon-on-Insulator," *IEEE Photonics J.* **6**, 1-9 (2014).
7. X. Pommarede, K. Hassan, P. Billondeau, V. Hugues, P. Grosse, B. Charbonnier, and G. H. Duan, "16×100 GHz Echelle Grating-Based Wavelength Multiplexer on Silicon-on-Insulator Platform," *IEEE Photonics*

- Technol. Lett. **29**, 493–495 (2017).
8. C. Sciancalepore, R. J. Lycett, J. A. Dallery, S. Pauliac, K. Hassan, J. Harduin, H. Duprez, U. Weidenmueller, D. F. G. Gallagher, S. Menezo, and B. Ben Bakir, "Low-crosstalk fabrication-insensitive echelle grating demultiplexers on silicon-on-insulator," *IEEE Photonics Technol. Lett.* **27**, 494–497 (2015).
  9. M. Muneeb, X. Chen, P. Verheyen, G. Lepage, S. Pathak, E. Ryckeboer, A. Malik, B. Kuyken, M. Nedeljkovic, J. Van Campenhout, G. Z. Mashanovich, and G. Roelkens, "Demonstration of Silicon-on-insulator mid-infrared spectrometers operating at 38 $\mu$ m," *Opt. Express* **21**, 11659-11669 (2013).
  10. W. Bogaerts, S. K. Selvaraja, P. Dumon, J. Brouckaert, K. De Vos, D. Van Thourhout, and R. Baets, "Silicon-on-insulator spectral filters fabricated with CMOS technology," *IEEE J. Sel. Top. Quantum Electron.* **16**, 33–44 (2010).
  11. D. Feng, W. Qian, H. Liang, C. C. Kung, J. Fong, B. J. Luff, and M. Asghari, "Fabrication insensitive echelle grating in silicon-on-insulator platform," *IEEE Photonics Technol. Lett.* **23**, 284–286 (2011).
  12. X. Ma, M. Li, and J. J. He, "CMOS-compatible integrated spectrometer based on echelle diffraction grating and MSM photodetector array," *IEEE Photonics J.* **5**, (2013).
  13. S. Janz, A. Balakrishnan, S. Charbonneau, P. Cheben, M. Cloutier, A. Del age, K. Dossou, L. Erickson, M. Gao, P. A. Krug, B. Lamontagne, M. Packirisamy, M. Pearson, and D. X. Xu, "Planar Waveguide Echelle Gratings in Silica-On-Silicon" *IEEE Photonics Technol. Lett.* **16**, 503–505 (2004).

14. E. Ryckeboer, X. Nie, A. Z. Subramanian, D. Martens, P. Bienstman, S. Clemmen, S. Severi, R. Jansen, G. Roelkens, and R. Baets, "CMOS-compatible silicon nitride spectrometers for lab-on-a-chip spectral sensing," *Proc. SPIE* (2016).
15. A. Malik, M. Muneeb, Y. Shimura, J. Van Campenhout, R. Loo, and G. Roelkens, "Germanium-on-silicon planar concave grating wavelength (de)multiplexers in the mid-infrared," *Appl. Phys. Lett.* **103**, 161119 (2013).
16. J. Pello, M. Muneeb, S. Keyvaninia, J. J. G. M. Van Der Tol, G. Roelkens, and M. K. Smit, "Planar concave grating demultiplexers on an inp-membrane-on-silicon photonic platform," *IEEE Photonics Technol. Lett.* **25**, 1969–1972 (2013).
17. N. C. Harris, D. Grassani, A. Simbula, M. Pant, M. Galli, T. Baehr-Jones, M. Hochberg, D. Englund, D. Bajoni, and C. Galland, "Integrated source of spectrally filtered correlated photons for large-scale quantum photonic systems," *Phys. Rev. X* **4**, 041047 (2014).
18. H. U. Yang, J. D'Archangel, M. L. Sundheimer, E. Tucker, G. D. Boreman, and M. B. Raschke, "Optical dielectric function of silver," *Phys. Rev. B* **91**, 235137 (2015).
19. T. Zhu, Y. Hu, P. Gatkine, S. Veilleux, J. Bland-Hawthorn, and M. Dagenais, "Ultrabroadband high coupling efficiency fiber-to-waveguide coupler using Si<sub>3</sub>N<sub>4</sub>/SiO<sub>2</sub> waveguides on silicon," *IEEE Photonics J.* **8**, 1-12 (2016).
20. J. J. He, B. Lamontagne, A. Del age, L. Erickson, M. Davies, and E. S.

- Koteles, "Monolithic integrated wavelength demultiplexer based on a waveguide rowland circle grating in InGaAsP/InP," *J. Light. Technol.* **16**, 631–637 (1998).
21. S. Xie, Y. Meng, J. Bland-Hawthorn, S. Veilleux, and M. Dagenais, "Silicon Nitride/Silicon Dioxide Echelle Grating Spectrometer for Operation Near 1.55  $\mu\text{m}$ ," *IEEE Photonics J.* **10**, 1–7 (2018).
  22. J. Brouckaert, W. Bogaerts, S. Selvaraja, P. Dumon, R. Baets, and D. Van Thourhout, "Planar Concave Grating Demultiplexer With High Reflective Bragg Reflector Facets," *IEEE Photonics Technol. Lett.* **20**, 309–311 (2008).
  23. K. Ma, K. Chen, N. Zhu, L. Liu, and S. He, "High-resolution compact on-chip spectrometer based on an echelle grating with densely packed waveguide array," *IEEE Photonics J.* **11**, 1–7 (2019).
  24. P. Gatkine, S. Veilleux, Y. Hu, J. Bland-Hawthorn, and M. Dagenais, "Arrayed Waveguide Grating Spectrometers for Astronomical Applications: New Results," **25**, 232–238 (2017).
  25. T. Zhu, Y. Hu, P. Gatkine, S. Veilleux, J. Bland-Hawthorn, and M. Dagenais, "Arbitrary on-chip optical filter using complex waveguide Bragg gratings," *Appl. Phys. Lett.* **108**, 101104 (2016).
  26. R. Sumi, R. K. Gupta, N. DasGupta, and B. K. Das, "Ultra-Broadband Add-Drop Filter/Switch Circuit Using Subwavelength Grating Waveguides," *IEEE J. Sel. Top. Quantum Electron.* **25**, 1–11 (2018).
  27. C. Errando-Herranz, F. Niklaus, G. Stemme, and K. B. Gylfason, "Low-power

- microelectromechanically tunable silicon photonic ring resonator add-drop filter," *Opt. Lett.* **40**, 3556-3559 (2015).
28. P. Rabiei, S. Member, W. H. Steier, L. Fellow, C. Zhang, and L. R. Dalton, "Polymer Micro-Ring Filters and Modulators.pdf," **20**, 1968–1975 (2002).
  29. K. Djordjev, S. J. Choi, S. J. Choi, and P. D. Dapkus, "Microdisk tunable resonant filters and switches," *IEEE Photonics Technol. Lett.* **14**, 828–830 (2002).
  30. D. Charron, J. St-Yves, O. Jafari, S. LaRochelle, and W. Shi, "Subwavelength-grating contradirectional couplers for large stopband filters," *Opt. Lett.* **43**, 895 (2018).
  31. C. Couplers, H. Qiu, J. Jiang, P. Yu, D. Mu, J. Yang, X. Jiang, H. Yu, R. Cheng, L. Chrostowski, and S. Member, "Narrow-Band Add-Drop Filter Based on," **36**, 3760–3764 (2018).
  32. S. Paul, T. Saastamoinen, S. Honkanen, M. Roussey, and M. Kuittinen, "Multi-wavelength filtering with a waveguide integrated phase-modulated Bragg grating," *Opt. Lett.* **42**, 4635–4638 (2017).
  33. S. Aastamoinen, J. A. N. I. T. Ervo, S. E. H. Onkanen, and M. Arkku, "Add-drop filter based on TiO<sub>2</sub> coated shifted Bragg grating," *Opt. Express* **24**, 32–39 (2016).
  34. A. D. Simard and S. LaRochelle, "Complex apodized Bragg grating filters without circulators in silicon-on-insulator," *Opt. Express* **23**, 16662-16675 (2015).

35. J. Wang and L. R. Chen, "Low crosstalk Bragg grating/Mach-Zehnder interferometer optical add-drop multiplexer in silicon photonics," *Opt. Express* **23**, 26450-26459 (2015).
36. M. Caverley, X. Wang, K. Murray, N. A. F. Jaeger, and L. Chrostowski, "Silicon-on-Insulator Modulators Using a Quarter-Wave Phase-Shifted Bragg Grating," *IEEE Photonics Technol. Lett.* **27**, 2331–2334 (2015).
37. J. Jiang, H. Qiu, G. Wang, Y. Li, T. Dai, X. Wang, H. Yu, J. Yang, and X. Jiang, "Broadband tunable filter based on the loop of multimode Bragg grating," *Opt. Express* **26**, 559-566 (2018).
38. L. B. Soldano and E. C. M. Pennings, "Optical Multi-Mode Interference Devices Based on Self-Imaging : Principles and Applications" *J. Lightwave Technol.* **13**, 615-627 (1995)
39. J. Skaar, Ligang Wang, and T. Erdogan, "On the synthesis of fiber Bragg gratings by layer peeling," *IEEE J. Quantum Electron.* **37**, 165–173 (2001).
40. J. Bland-Hawthorn, S. C. Ellis, S. G. Leon-Saval, R. Haynes, M. M. Roth, H.-G. Löhmannsröben, a J. Horton, J.-G. Cuby, T. a Birks, J. S. Lawrence, P. Gillingham, S. D. Ryder, and C. Trinh, "A complex multi-notch astronomical filter to suppress the bright infrared sky.," *Nat. Commun.* **2**, 581 (2011).
41. C. Q. Trinh, S. C. Ellis, J. Bland-Hawthorn, J. S. Lawrence, A. J. Horton, S. G. Leon-Saval, K. Shortridge, J. Bryant, S. Case, M. Colless, W. Couch, K. Freeman, H. G. Löhmannsröben, L. Gers, K. Glazebrook, R. Haynes, S. Lee, J. O’Byrne, S. Mizziarski, M. M. Roth, B. Schmidt, C. G. Tinney, and J. Zheng,

- "Gnosis: The first instrument to use fiber bragg gratings for oh suppression,"  
Astron. J. **145**, 51(2013).
42. M. A. Foster, A. C. Turner, J. E. Sharping, B. S. Schmidt, M. Lipson, and A. L. Gaeta, "Broad-band optical parametric gain on a silicon photonic chip,"  
Nature **441**, 960–963 (2006).
43. P. Del’Haye, A. Schliesser, O. Arcizet, T. Wilken, R. Holzwarth, and T. J. Kippenberg, "Optical frequency comb generation from a monolithic microresonator," Nature **450**, 1214–1217 (2007).
44. M. Ferrera, L. Razzari, D. Duchesne, R. Morandotti, Z. Yang, M. Liscidini, J. E. Sipe, S. Chu, B. E. Little, and D. J. Moss, "Low-power continuous-wave nonlinear optics in doped silica glass integrated waveguide structures," Nat. Photonics **12**, 737-740 (2008).
45. J. S. Levy, A. Gondarenko, M. A. Foster, A. C. Turner-Foster, A. L. Gaeta, and M. Lipson, "CMOS-compatible multiple-wavelength oscillator for on-chip optical interconnects," Nat. Photonics **4**, 37–40 (2010).
46. A. C. Turner, M. A. Foster, A. L. Gaeta, and M. Lipson, "Ultra-low power parametric frequency conversion in a silicon microring resonator," Opt. Express **16**, 4881-4887 (2008).
47. S. A. Miller, M. Yu, X. Ji, A. G. Griffith, J. Cardenas, A. L. Gaeta, and M. Lipson, "Low-loss silicon platform for broadband mid-infrared photonics," Optica **4**, 707-712 (2017).
48. M. Pu, L. Ottaviano, E. Semenova, and K. Yvind, "Efficient frequency comb

- generation in AlGaAs-on-insulator," *Optica* **3**, 823-826 (2016).
49. C. Wang, M. Zhang, M. Yu, R. Zhu, H. Hu, and M. Loncar, "Monolithic lithium niobate photonic circuits for Kerr frequency comb generation and modulation," *Nat. Commun.* **10**, 978 (2019).
  50. B. Desiatov, A. Shams-Ansari, M. Zhang, C. Wang, and M. Lončar, "Ultra-low-loss integrated visible photonics using thin-film lithium niobate," *Optica* **6**, 380-384 (2019).
  51. M. Zhang, B. Buscaino, C. Wang, A. Shams-Ansari, C. Reimer, R. Zhu, J. M. Kahn, and M. Lončar, "Broadband electro-optic frequency comb generation in a lithium niobate microring resonator," *Nature* **568**, 373–377 (2019).
  52. A. Fülöp, C. J. Krückel, D. Castelló-Lurbe, E. Silvestre, and V. Torres-Company, "Triply resonant coherent four-wave mixing in silicon nitride microresonators," *Opt. Lett.* **40**, 4006-4009 (2015).
  53. P. P. Absil, J. V. Hryniewicz, B. E. Little, P. S. Cho, R. A. Wilson, L. G. Joneckis, and P.-T. Ho, "Wavelength conversion in GaAs micro-ring resonators," *Opt. Lett.* **25**, 554-556 (2000).
  54. B. Stern, X. Ji, Y. Okawachi, A. L. Gaeta, and M. Lipson, "Battery-operated integrated frequency comb generator," *Nature* **562**, 401–405 (2018).
  55. Q. Li, T. C. Briles, D. A. Westly, T. E. Drake, J. R. Stone, B. R. Ilic, S. A. Diddams, S. B. Papp, and K. Srinivasan, "Stably accessing octave-spanning microresonator frequency combs in the soliton regime," *Optica* **4**, 193-203 (2017).

56. Q. Li, M. Davanço, and K. Srinivasan, "Efficient and low-noise single-photon-level frequency conversion interfaces using silicon nanophotonics," *Nat. Photonics* **10**, 406–414 (2016).
57. S. Kim, K. Han, C. Wang, J. A. Jaramillo-Villegas, X. Xue, C. Bao, Y. Xuan, D. E. Leaird, A. M. Weiner, and M. Qi, "Dispersion engineering and frequency comb generation in thin silicon nitride concentric microresonators," *Nat. Commun.* **8**, 372 (2017).
58. D. Braje, L. Hollberg, and S. Diddams, "Brillouin-Enhanced Hyperparametric Generation of an Optical Frequency Comb in a Monolithic Highly Nonlinear Fiber Cavity Pumped by a cw Laser," *Phys. Rev. Lett.* **102**, 193902 (2009).
59. E. Obrzud, S. Lecomte, and T. Herr, "optical pulses," *Nat. Photonics* **11**, 600–607 (2017).
60. S.-P. Yu, H. Jung, T. C. Briles, K. Srinivasan, and S. B. Papp, "Photonic-Crystal-Reflector Nanoresonators for Kerr-Frequency Combs," *ACS Photonics* **6**, 2083-2089 (2019).
61. A. M. Darwish, E. P. Ippen, H. Q. Le, J. P. Donnelly, and S. H. Groves, "Optimization of four-wave mixing conversion efficiency in the presence of nonlinear loss," *Appl. Phys. Lett.* **69**, 737–739 (1996).
62. Y.-W. Hu, Y. Zhang, P. Gatkine, J. Bland-Hawthorn, S. Veilleux, and M. Dagenais, "Characterization of Low Loss Waveguides Using Bragg Gratings," *IEEE J. Sel. Top. Quantum Electron.* **24**, 1–8 (2018).
63. P. Lalanne and J. P. Hugonin, "Bloch-wave engineering for high-Q, small-V

- microcavities," *IEEE J. Quantum Electron.* **39**, 1430–1438 (2003).
64. P. Lalanne, S. Mias, and J. P. Hugonin, "Two physical mechanisms for boosting the quality factor to cavity volume ratio of photonic crystal microcavities," *Opt. Express* **12**, 458-467 (2004).
65. Q. Quan, P. B. Deotare, and M. Loncar, "Photonic crystal nanobeam cavity strongly coupled to the feeding waveguide," *Appl. Phys. Lett.* **96**, 203102 (2010).
66. A. Gondarenko, J. S. Levy, and M. Lipson, "High confinement micron-scale silicon nitride high Q ring resonator," *Opt. Express* **17**, 11366-11370 (2009).
67. K. Luke, A. Dutt, C. B. Poitras, and M. Lipson, "Overcoming Si<sub>3</sub>N<sub>4</sub> film stress limitations for high quality factor ring resonators," *Opt. Express* **21**, 22829-22833 (2013).
68. M. H. P. Pfeiffer, C. Herkommer, J. Liu, T. Morais, M. Zervas, M. Geiselmann, and T. J. Kippenberg, "Photonic damascene process for low-loss, high-confinement silicon nitride waveguides," *IEEE J. Sel. Top. Quantum Electron.* **24**, 1–11 (2018).
69. S. Xie, Y. Zhang, Y. Hu, S. Veilleux, and M. Dagenais, "On-Chip Fabry-Perot Bragg Grating Cavity Enhanced Four-Wave Mixing," *ACS Photonics* **7**, 1009–1015 (2020).
70. M. Kues, C. Reimer, P. Roztocky, L. R. Cortés, S. Sciara, B. Wetzl, Y. Zhang, A. Cino, S. T. Chu, B. E. Little, D. J. Moss, L. Caspani, J. Azaña, and R. Morandotti, "On-chip generation of high-dimensional entangled quantum

- states and their coherent control," *Nature* **546**, 622–626 (2017).
71. J. A. Jaramillo-Villegas, P. Imany, O. D. Odele, D. E. Leaird, Z.-Y. Ou, M. Qi, and A. M. Weiner, "Persistent energy–time entanglement covering multiple resonances of an on-chip biphoton frequency comb," *Optica* **4**, 655-658 (2017).
  72. X. Ji, F. A. S. Barbosa, S. P. Roberts, A. Dutt, J. Cardenas, Y. Okawachi, A. Bryant, A. L. Gaeta, and M. Lipson, "Ultra-low-loss on-chip resonators with sub-milliwatt parametric oscillation threshold," *Optica* **4**, 619-624 (2017).
  73. Y. Xuan, Y. Liu, L. T. Varghese, A. J. Metcalf, X. Xue, P.-H. Wang, K. Han, J. A. Jaramillo-Villegas, A. Al Noman, C. Wang, S. Kim, M. Teng, Y. J. Lee, B. Niu, L. Fan, J. Wang, D. E. Leaird, A. M. Weiner, and M. Qi, "High-Q silicon nitride microresonators exhibiting low-power frequency comb initiation," *Optica* **3**, 1171-1180 (2016).
  74. H. El Dirani, L. Youssef, C. Petit-Etienne, S. Kerdiles, P. Grosse, C. Monat, E. Pargon, and C. Sciancalepore, "Ultralow-loss tightly confining Si<sub>3</sub>N<sub>4</sub> waveguides and high-Q microresonators," *Opt. Express* **27**, 30726-30740 (2019).
  75. C. Xiong, W. H. P. Pernice, X. Sun, C. Schuck, K. Y. Fong, and H. X. Tang, "Aluminum nitride as a new material for chip-scale optomechanics and nonlinear optics," *New J. Phys.* **14**, 095014 (2012).
  76. X. Liu, C. Sun, B. Xiong, L. Wang, J. Wang, Y. Han, Z. Hao, H. Li, Y. Luo, J. Yan, T. Wei, Y. Zhang, and J. Wang, "Aluminum nitride-on-sapphire platform for integrated high-Q microresonators," *Opt. Express* **25**, 587-594 (2017).

77. Y. Sun, W. Shin, D. A. Laleyan, P. Wang, A. Pandey, X. Liu, Y. Wu, M. Soltani, and Z. Mi, "Ultra-high Q microring resonators using a single-crystal aluminum-nitride-on-sapphire platform," *Opt. Lett.* **44**, 5679-5682 (2019).
78. J. Kischkat, S. Peters, B. Gruska, M. Semtsiv, M. Chashnikova, M. Klinkmüller, O. Fedosenko, S. MacHulik, A. Aleksandrova, G. Monastyrskyi, Y. Flores, and W. T. Masselink, "Mid-infrared optical properties of thin films of aluminum oxide, titanium dioxide, silicon dioxide, aluminum nitride, and silicon nitride," *Appl. Opt.* **51**, 6789–6798 (2012).
79. H. Jung and H. X. Tang, "Aluminum nitride as nonlinear optical material for on-chip frequency comb generation and frequency conversion," *Nanophotonics* **5**, 263–271 (2016).
80. A. Yariv, "Critical coupling and its control in optical waveguide-ring resonator systems," *IEEE Photonics Technol. Lett.* **14**, 483–485 (2002).
81. A. Yariv and P. Yeh, "Photonics: Optical Electronics in Modern Communications," Oxford University Press (2007).
82. D. T. Spencer, J. F. Bauters, M. J. R. Heck, and J. E. Bowers, "Integrated waveguide coupled Si<sub>3</sub>N<sub>4</sub> resonators in the ultrahigh-Q regime," *Optica* **1**, 153-157 (2014).
83. J. E. Heebner, V. Wong, A. Schweinsberg, R. W. Boyd, and D. J. Jackson, "Optical transmission characteristics of fiber ring resonators," *IEEE J. Quantum Electron.* **40**, 726–730 (2004).
84. P. E. Barclay, K. Srinivasan, and O. Painter, "Nonlinear response of silicon

- photonic crystal micresonators excited via an integrated waveguide and fiber taper," *Opt. Express* **13**, 801-820 (2005).
85. B. Stern, X. Ji, A. Dutt, and M. Lipson, "Compact narrow-linewidth integrated laser based on low-loss silicon nitride ring resonator," *Opt. Lett.* **42**, 4541-4544 (2017)
  86. M. W. Puckett, K. Liu, N. Chauhan, Q. Zhao, N. Jin, H. Cheng, J. Wu, R. O. Behunin, P. T. Rakich, K. D. Nelson, and D. J. Blumenthal, "422 Million intrinsic quality factor planar integrated all-waveguide resonator with sub-MHz linewidth," *Nat. Commun.* **12**, 1–8 (2021).
  87. J. Liu, G. Huang, R. N. Wang, J. He, A. S. Raja, T. Liu, N. J. Engelsen, and T. J. Kippenberg, "High-yield, wafer-scale fabrication of ultralow-loss, dispersion-engineered silicon nitride photonic circuits," *Nat. Commun.* **12**, 934 (2021).
  88. J. F. Bauters, M. J. R. Heck, D. D. John, J. S. Barton, C. M. Bruinink, A. Leinse, R. G. Heideman, D. J. Blumenthal, and J. E. Bowers, "Planar waveguides with less than 01 dB/m propagation loss fabricated with wafer bonding," *Opt. Express* **19**, 24090-24101 (2011).
  89. A. Wolszczan and D. A. Frail, "A planetary system around the millisecond pulsar PSR1257 + 12," *Nature* **355**, 145–147 (1992).
  90. D. Defrère, P. M. Hinz, B. Mennesson, W. F. Hoffmann, R. Millan-Gabet, A. J. Skemer, V. Bailey, W. C. Danchi, E. C. Downey, O. Durney, P. Grenz, J. M. Hill, T. J. McMahon, M. Montoya, E. Spalding, A. Vaz, O. Absil, P. Arbo, H.

- Bailey, G. Brusa, G. Bryden, S. Esposito, A. Gaspar, C. A. Haniff, G. M. Kennedy, J. M. Leisenring, L. Marion, M. Nowak, E. Pinna, K. Powell, A. Puglisi, G. Rieke, A. Roberge, E. Serabyn, R. Sosa, K. Stapelfeldt, K. Su, A. J. Weinberger, and M. C. Wyatt, "Nulling Data Reduction and on-Sky Performance of the Large Binocular Telescope Interferometer," *Astrophys. J.* **824**, 66 (2016).
91. A. Roberge, C. H. Chen, R. Millan-Gabet, A. J. Weinberger, P. M. Hinz, K. R. Stapelfeldt, O. Absil, M. J. Kuchner, and G. Bryden, "The Exozodiacal Dust Problem for Direct Observations of Exo-Earths," *Publ. Astron. Soc. Pacific* **124**, 799–808 (2012).
92. D. Defrère, O. Absil, R. Den Hartog, C. Hanot, and C. Stark, "Nulling interferometry: Impact of exozodiacal clouds on the performance of future life-finding space missions," *Astron. Astrophys.* **509**, 1–17 (2010).
93. C. C. Stark, A. Roberge, A. Mandell, M. Clampin, S. D. Domagal-Goldman, M. W. McElwain, and K. R. Stapelfeldt, "LOWER LIMITS on APERTURE SIZE for AN EXOEARTH DETECTING CORONAGRAPHIC MISSION," *Astrophys. J.* **808**, 149 (2015).
94. R. N. BRACEWELL, "Detecting nonsolar planets by spinning infrared interferometer," *Nature* **274**, 780–781 (1978).
95. P. M. Hinz, J. R. P. Angel, W. F. Hoffmann, D. W. McCarthy, P. C. McGuire, M. Cheselka, J. L. Hora, and N. J. Woolf, "Imaging circumstellar environments with a nulling interferometer," *Nature* **395**, 251–253 (1998).

96. J. P. Berger, K. Rousselet-Perraut, P. Kern, F. Malbet, I. Schanen-Duport, F. Reynaud, P. Haguenuer, and P. Benech, "Integrated optics for astronomical interferometry," *Astron. Astrophys. Suppl. Ser.* **139**, 173–177 (1999).
97. M. Benisty, J. P. Berger, L. Jocou, P. Labeye, F. Malbet, K. Perraut, and P. Kern, "An integrated optics beam combiner for the second generation VLTI instruments," *Astron. Astrophys.* **498**, 601–613 (2009).
98. R. Abuter, M. Accardo, A. Amorim, N. Anugu, G. Ávila, N. Azouaoui, M. Benisty, J. P. Berger, N. Blind, H. Bonnet, P. Bourget, W. Brandner, R. Brast, A. Buron, L. Burtscher, F. Cassaing, F. Chapron, E. Choquet, Y. Clénet, C. Collin, V. Coudé Du Foresto, W. De Wit, P. T. De Zeeuw, C. Deen, F. Delplancke-Ströbele, R. Dembet, F. Derie, J. Dexter, G. Duvert, M. Ebert, A. Eckart, F. Eisenhauer, M. Esselborn, P. Fédou, G. Finger, P. Garcia, C. E. Garcia Dabo, R. Garcia Lopez, E. Gendron, R. Genzel, S. Gillessen, F. Gonte, P. Gordo, M. Grould, U. Grözinger, S. Guieu, P. Haguenuer, O. Hans, X. Haubois, M. Haug, F. Haussmann, T. Henning, S. Hippler, M. Horrobin, A. Huber, Z. Hubert, N. Hubin, C. A. Hummel, G. Jakob, A. Janssen, L. Jochum, L. Jocou, A. Kaufer, S. Kellner, S. Kendrew, L. Kern, P. Kervella, M. Kiekebusch, R. Klein, Y. Kok, J. Kolb, M. Kulas, S. Lacour, V. Lapeyrère, B. Lazareff, J. B. Le Bouquin, P. Lèna, R. Lenzen, S. Lévêque, M. Lippa, Y. Magnard, L. Mehrgan, M. Mellein, A. Mérand, J. Moreno-Ventas, T. Moulin, E. Müller, F. Müller, U. Neumann, S. Oberti, T. Ott, L. Pallanca, J. Panduro, L. Pasquini, T. Paumard, I. Percheron, K. Perraut, G. Perrin, A. Pflüger, O. Pfuhl,

- T. Phan Duc, P. M. Plewa, D. Popovic, S. Rabien, A. Ramírez, J. Ramos, C. Rau, M. Riquelme, R. R. Rohloff, G. Rousset, J. Sanchez-Bermudez, S. Scheithauer, M. Schöller, N. Schuhler, J. Spyromilio, C. Straubmeier, E. Sturm, M. Suarez, K. R. W. Tristram, N. Ventura, F. Vincent, I. Waisberg, I. Wank, J. Weber, E. Wieprecht, M. Wiest, E. Wiezorrek, M. Wittkowski, J. Woillez, B. Wolff, S. Yazici, D. Ziegler, and G. Zins, "First light for GRAVITY: Phase referencing optical interferometry for the Very Large Telescope Interferometer," *Astron. Astrophys.* **602**, 1–23 (2017).
99. T. Gretzinger, S. Gross, A. Arriola, and M. J. Withford, "Towards a photonic mid-infrared nulling interferometer in chalcogenide glass," *Opt. Express* **27**, 8626-8636 (2019).
100. H.-D. K. Goldsmith, N. Cvetojevic, M. Ireland, and S. Madden, "Fabrication tolerant chalcogenide mid-infrared multimode interference coupler design with applications for Bracewell nulling interferometry," *Opt. Express* **25**, 3038-3051 (2017).
101. S. Xie, J. Zhan, Y. Hu, Y. Zhang, S. Veilleux, J. Bland-Hawthorn, and M. Dagenais, "Add-drop filter with complex waveguide Bragg grating and multimode interferometer operating on arbitrarily spaced channels," *Opt. Lett.* **43**, 6045-6048 (2018).
102. A. W. Elshaari, I. E. Zadeh, K. D. Jöns, and V. Zwiller, "Thermo-Optic Characterization of Silicon Nitride Resonators for Cryogenic Photonic Circuits," *IEEE Photonics J.* **8**, 1-9(2016).

103. S. Liu, H. Cai, C. T. DeRose, P. Davids, A. Pomerene, A. L. Starbuck, D. C. Trotter, R. Camacho, J. Urayama, and A. Lentine, "High speed ultra-broadband amplitude modulators with ultrahigh extinction >65 dB," *Opt. Express* **25**, 11254-11264 (2017).
104. M. Jin, J.-Y. Chen, Y. M. Sua, and Y.-P. Huang, "High-extinction electro-optic modulation on lithium niobate thin film," *Opt. Lett.* **44**, 1265-1268 (2019).
105. Y.-W. Hu, S. Xie, J. Zhan, Y. Zhang, S. Veilleux, and M. Dagenais, "Integrated Arbitrary Filter With Spiral Gratings: Design and Characterization," *J. Light. Technol.* Vol. 38, Issue 16, pp. 4454-4461 **38**, 4454–4461 (2020).
106. A. Biberman, M. J. Shaw, E. Timurdogan, J. B. Wright, and M. R. Watts, "Ultralow-loss silicon ring resonators," *Opt. Lett.* **37**, 4236-4238 (2012).